

12

AD-A259 464

2



NUMERICAL SOLUTION OF THREE-DIMENSIONAL
UNSTEADY VISCOUS FLOWS

DTIC
ELECTE
DEC 23 1992
S C D

Final Report for the period
Dec. 1, 1988 to Nov. 30, 1992

DISTRIBUTION STATEMENT A
Approved for public release
Distribution Unlimited

Prepared by

Lakshmi N. Sankar (Professor)

Wan-Gyu Park (Graduate Student)

School of Aerospace Engineering

Georgia Institute of Technology

Atlanta, GA 30332

December 1992

92-32617

92 12 182

Table of Contents

Accession For	
NTIS GRA&I	<input checked="" type="checkbox"/>
DTIC TAB	<input type="checkbox"/>
Unannounced	<input type="checkbox"/>
Justification	
By <i>Per AD-A253202</i>	
Distribution/	
Availability Codes	
Dist	Avail and/or Special
<i>A-1</i>	

1. Introduction

Appendix :

DTIC QUALITY INSPECTED 3

- (a) Tang, W., Sankar, L. N., and Strahle, W. C., "Numerical Simulation of Vorticity-Acoustic Interaction within Dump Combustors," AIAA Paper 88-0597, 1988.
- (b) Tang, W., Sankar, L. N., and Komerath, N., "Mixing Enhancement in Supersonic Free Shear Layers," AIAA Paper 89-0981, 1989.
- (c) Tang, W., Komerath, N., and Sankar, L. N., "Numerical Simulation of the Growth of Instabilities in Supersonic Free Layers," Journal of Propulsion and Power, Vol. 6, No. 4, pp. 455-460, 1990.
- (d) Tuncer, I. H. and Sankar, L. N., "Numerical Simulation of Three-Dimensional Supersonic Free Shear Layers," AIAA Journal, Vol. 30, No. 4, pp. 871-872, 1992.
- (e) Sankar, L. N. and Park, W. G., "An Iterative Time Marching Procedure for Computation of Unsteady Viscous Flows," ASME-BED, Vol. 20, pp. 281-284, 1991.
- (f) Park, W. G., "A Three-Dimensional Multigrid Technique for Unsteady Incompressible Viscous Flows," Ph.D. Thesis, Georgia Institute of Technology, Atlanta, Georgia, 1993.

INTRODUCTION

During the past four years, under the support of Office of Naval Research, a research effort has been underway on the following two topics :

- (a) Numerical simulation of supersonic shear layer mixing phenomena.
- (b) Development of efficient methods for 3-D unsteady incompressible viscous flow simulations.

Substantial progress was made in the above areas, and the computer codes developed as part of these efforts were transferred for further use to Virginia Polytechnic Institute (Dr. Saad Ragab) and to David Taylor Research and Development Center (Dr. Wei Tang).

The progress made has been documented in a number of conference proceedings, two journal articles and a Ph. D. dissertation (in progress). The Appendix contains all the published work done to date.

This research led to a number of significant new findings. Some of the major accomplishments are as follows :

- (a) A highly accurate method for simulating compressible mixing layers was developed. This method is suitable for direct numerical simulation (DNS) and large eddy simulation (LES) of compressible turbulence, and is used in this context by other researchers.
- (b) An iterative time marching method for 3-D incompressible flows was developed. This method is robust, and can handle internal and external flows. It employs a multigrid iterative strategy for satisfying the discretized form of the governing equations of 3-D viscous flows to great accuracy.

It is hoped that these efforts will serve as useful stepping stones for future research in these areas.

APPENDIX

AIAA'88

AIAA-88-0597

**Numerical Simulation of Vorticity-
Acoustics Interactions within Dump
Combustors**

**W. Tang, L. N. Sankar, and W. C.
Strahle, Georgia Institute of
Technology, Atlanta, GA**

AIAA 26th Aerospace Sciences Meeting

January 11-14, 1988/Reno, Nevada

NUMERICAL SIMULATION OF VORTICITY-ACOUSTICS INTERACTIONS WITHIN DUMP COMBUSTORS

W. Tang^{*}, L. N. Sankar^{**}, and W. C. Strahle^{***}

School of Aerospace Engineering
Georgia Institute of Technology
Atlanta, Georgia 30332

ABSTRACT

The behavior of free shear layers within ramjet dump combustors is studied through the numerical solution of unsteady compressible Navier-Stokes equations. Three configurations are considered: a) a short combustor with an open downstream boundary, b) a long combustor with an open downstream boundary, and c) a short combustor with a partially blocked downstream boundary. Vorticity contours of the computed flow fields in all the three cases reveal oscillations of the shear layer, roll up and shedding of organized vortices. A Fourier analysis of the computed flow fields indicates that the natural acoustic frequency of the system, and the natural shear layer instability frequency are the two dominant frequencies of the flow field. It is also observed that the boundary conditions play a crucial role in the behavior of the combustor flow field.

INTRODUCTION

The flow field within ramjet combustors is characterized by a variety of phenomena such as thin boundary layers along the walls of the inlet and combustor, recirculating flow zones, reacting flow and free shear layers. The free shear layer is unstable by nature, and can undergo large spatial and temporal oscillations when subjected to disturbances. In many cases, the shear layer may roll up and form vortices, which are shed at periodic intervals resulting in a highly unsteady, and undesirable flow environment within the combustor. There is a need to understand the response of the shear layer to externally imposed acoustic disturbances, and device passive and active control techniques for controlling the behavior of this flow field. Both theoretical and experimental studies are being carried out to understand the behavior of the free shear layer within dump combustors.¹⁻³ A number of investigators have also studied numerically the flow fields within the dump combustors, using explicit time marching techniques, with and without viscous terms.⁴⁻⁷

The experimental studies reported in Ref. 1 show that the behavior of the free shear layer is sensitive to periodic acoustic disturbances imposed at the downstream boundary. In some cases, it has been shown possible to drastically alter the size of the recirculation zone using disturbances. There is a need to systematically study the

significant role that the external boundary conditions and the related acoustics play on the behavior of the free shear layer. As a first step towards such a study, the flow field within a 2-D dump combustor is studied through the numerical solution of the unsteady, compressible Navier-Stokes equations. The acoustics characteristics of the inlet-combustor system is altered by changing either the length of the combustor, or altering the downstream boundary condition, by partially blocking the downstream boundary. The length of the inlet, and the flow Reynolds number are held fixed in order to avoid significant changes of the thickness of the shear layer, and its natural instability characteristics.

The computed flow fields are analyzed using iso-vorticity plots at selected time levels. The flow properties at selected locations within the shear layer are also analyzed using Fourier transform techniques to identify the dominant frequencies. The shear layer downstream of the step is analyzed using classical, linear instability analyses to identify the natural frequency of the shear layer. It is found that the boundary conditions play a crucial role in the behavior of the unsteady flow within the combustor.

NUMERICAL FORMULATION

In Fig. 1, the three configurations being analyzed are shown. The typical dimensions of the configurations are also indicated, normalized with respect to the step height. The unsteady flow within the combustor is governed by 2-D compressible Navier-Stokes equations, and is likely to be turbulent. Because existing algebraic and two equation models are not suitable for unsteady flows, and because these models can smear out features such as shear layer instability and vortex roll up, in the present work no explicit turbulence model was used. An algebraically generated, stretched Cartesian coordinate system was used. The governing equations, which are parabolic with respect to time, were integrated using an implicit time marching procedure, originally devised by Beam and Warming.⁸ This procedure is second order accurate in space, and may be designed to be either first or second order accurate with respect to time. In the present work, the first order time accuracy option was used. This procedure has been previously applied to unsteady external flow problems with good success.⁹ In the Appendix, the mathematical formulation is briefly described.

Since numerical solutions are sensitive to grid spacing, a variety of grid sizes were experimented with, ranging from a coarse 61 x 41 grid

* Research Engineer, Member, AIAA.

** Associate Professor, Member, AIAA.

*** Regents Professor, Fellow, AIAA.

system, to a fine 151 x 121 grid system. As expected, increased grid refinement leads to improved resolution of features such as the shear layer roll up. The basic characteristics of the flow such as the length of the recirculation zone at a given time, and the thickness of the shear layer are, however, insensitive to grid spacing. Based on these exploratory studies, in the calculations to be reported here it was decided to use the 151 x 121 grid system. Because excessive grid stretching can reduce the formal spatial accuracy of the solution from second order to first order, and lead to a loss of resolution of the flow features, a uniform grid spacing was used in the studies reported here. For the short combustor configuration shown, this is equivalent to grid spacings of 0.15 and 0.025 along the x- and z-directions respectively.

Numerical viscosity is introduced into the solution procedure through a set of artificial viscosity terms as explained in the appendix. In order to assess the effects of artificial viscosity on the solution, calculations were performed for values of the artificial viscosity coefficient between 1 and 5. The flow features were insensitive to this coefficient, within this range. Subsequently, a value of unity was used for the artificial viscosity coefficient, in the calculations to be reported.

BOUNDARY CONDITIONS

Because the governing equations are parabolic with respect to time, the proper boundary condition for this problem is the specification of velocity, and temperature at all time levels at all the boundaries. Unfortunately, such a complete specification of the boundary conditions is seldom feasible, and rarely available from experiments. Therefore, the following set of approximate boundary conditions have been used.

At all the solid walls, the no slip boundary condition was imposed. Furthermore, the normal derivative of pressure was set to zero. The temperature at the solid walls was evaluated using adiabatic assumptions. The density at the wall was subsequently extracted from the equation of state.

At the inlet, the flow was assumed to be parallel to the x- axis, and the velocity profile was assumed to be a "plug" profile (uniform everywhere except at the walls). The Mach number at the inlet was chosen to be 0.2, and the inflow density was assumed to be unity. Furthermore, the derivative of pressure along the x- axis was assumed to be zero at the inlet.

At the outflow boundary, two different treatments are needed depending on whether the downstream boundary is partially blocked, or is completely open. Configurations 1 and 2 shown in Fig. 1 have open downstream boundaries. On the open boundary the pressure was prescribed, while the other three flow variables (density, u and v components of velocity) were extrapolated from the interior. The portion of the downstream boundary that is blocked was treated like any other solid wall.

The above boundary conditions are considered "reflecting" boundary conditions. That is, they allow part of the signals attempting to leave the

computational domain to be reflected back at the inlet and the outflow boundary. In a real world situation, say in a wind tunnel, no such reflections occur although there may be other sources of disturbances such as background noise. In other cases, say within a ramjet combustor, the inlet and exit may be choked. Thus the above boundary conditions are a poor substitute for what takes place near the boundaries of a wind tunnel or a ramjet combustor. As mentioned earlier, removal of false reflections from the boundaries would require prescription of velocity and temperature at all boundaries at all time levels.

The reflecting boundary conditions described above serve one very useful purpose, however. They provide a continuous, small supply of acoustic energy at a frequency which is characteristic of the dimensions of the configuration. These waves can interact with the shear layer, and lead to amplification of shear layer instability, shear layer roll up and other interesting phenomena. For the situation where the pressure is fixed at the downstream boundary, and has zero gradient at the upstream boundary, the acoustic mode imposed by the reflecting boundaries corresponds to the quarter wave acoustic mode. Since the frequency of this mode may be changed by changing the length of the configuration, it is possible to study the response of the shear layer to a particular frequency, simply by choosing a suitable length of the configuration. For the short combustor configuration shown in Fig. 1, the quarter wave frequency happens to be 160 Hertz.

RESULTS AND DISCUSSION

Calculations have been carried out for the three configurations shown in Fig. 1. In all the cases, the flow was started impulsively, assuming the air to be stationary within the configuration at time $t = 0$, except at the inflow boundary. At subsequent time levels, the flow velocity within the combustor steadily increases as the stationary mass of air is replaced by the high speed airstream. At later time levels, a periodic pattern is established, in which the shear layer oscillates in resonance with a frequency that is characteristic of the combustor length for configurations 1 and 2, and the cavity length for configuration 3. During a given cycle a part of the shear layer rolls up into a vortex, and is shed. Depending on the case studied, this vortex may merge with previously shed vortices downstream at a subsequent time.

To verify the observation that the present boundary conditions lead to the presence of quarter wave acoustic modes for configurations 1 and 2, a large number of calculations were done on a somewhat coarser grid, for a number of configurations. The length of the combustor was parametrically changed. In Fig. 2, the frequency of flapping of the shear layer is plotted as a function of the length of the configuration. The quarter wave acoustic frequency associated with the configuration, given by $4a/L$ where a is the speed of sound, is also plotted. It is seen that these two quantities match well for the entire range of combustor lengths. Similar studies have been done with configuration 3, which indicate that the shear layer oscillates at the natural frequency of the cavity.

Configuration 1: For a detailed discussion of the shear layer dynamics, we concentrate on configuration 1. In Fig. 3, the vorticity contours within the dump combustor after a large period of time are shown, at regular time levels. It is seen that the vorticity contours at time $t = 210$ (normalized with respect to step height and inlet speed of sound) are identical to those at $t = 300$. The other time levels ($t = 220$, $t = 310$), ($t = 230$, $t = 320$) etc. also match. That is, the shear layer pattern repeats itself once every 90 non-dimensional units of time. This exactly equals the quarter wave acoustic frequency of configuration 1, which has a length equal to 22.5.

In Fig. 3, it is seen that the shear layer undergoes considerable lateral oscillations called flapping. It is also seen that the shear layer periodically rolls up and sheds a vortex, for example between time levels 220 and 290. During the time interval $250 < t < 290$, this vortex pairs into two smaller vortices which are convected out of the flow domain.

In Fig. 4, the pressure variation at a point one step height downstream, and in the middle of the shear layer is plotted as a function of time. It is seen that the pressure values oscillate at a distinct frequency, but the amplitude varies from cycle to cycle. The calculations were carried out for approximately 12 cycles of oscillation (approximately 1200 units of time, 24000 time steps) to ensure that the phenomena being discussed repeat themselves.

In order to understand why the amplitude of pressure oscillations vary from cycle to cycle, the pressure distribution shown within 4 was analyzed using Fast Fourier transform techniques. In Fig. 5, the Fourier transform of the pressure signals at six different locations is plotted. Note that the distances indicated are measured from the corner of the step. It is seen that the Fourier transform shows pressure peaks at four distinct frequencies, equal to 160, 304, 416 and 592 Hz. The fourth frequency appears to be combinations of the first and third frequency ($160 + 416 = 592$). The 160 Hz peak occurs as a result of the quarter wave acoustic mode.

To assess the reason for the existence of the 304 Hz peak, the shear layer velocity distribution just downstream of the boundary was analyzed using classical inviscid shear layer stability analysis. The amplitude of the streamwise growth of disturbances within the shear layer was studied as a function of user input sinusoidal temporal variation. In Fig. 6, the real part of the growth rate is plotted as a function of the input frequency, for a velocity profile 1.5 steps downstream of the step. It is seen that at a frequency of 300, the most rapid spatial growth of the linear instability waves occur. We have repeated these stability calculations at a number of stations in the immediate vicinity of the step, using velocity profiles selected at random time levels. In all cases, the analysis indicated that at 300 Hz the shear layer is most prone to instabilities.

From the above discussions one may conclude that the shear layer within the configuration 1 locks onto the quarter wave acoustic frequency of the shear layer, and oscillates. Shear layer roll up and shedding of vortices also occur at the

quarter wave acoustic frequency. Secondary oscillations also occur within the shear layer at frequency close to the natural frequency of roll up of the shear layer. Some of the higher frequencies observed may be seen to be combinations of the above two fundamental frequencies of the flow.

Configuration 2: This configuration differs from configuration 1 only in the length of the combustor. The increased length of the combustor leads to a somewhat lower quarter wave acoustic frequency, equal to 48 Hz. In Fig. 7, the vorticity contours are plotted at selected time intervals for the period $200 < t < 300$. The natural frequency of roll up of the shear layer, computed using velocity profiles just downstream of the step was found to be 270 Hz. In this case the shear layer still locks onto the quarter wave acoustic frequency of the system and tends to oscillate very slowly.

In Fig. 8, the Fourier transform of the pressure at two locations within the shear layer is shown. It is seen that two distinct peaks, one at the system acoustic frequency of 90 Hz, and the other near the shear layer roll up frequency of 270 Hz. Because the time step was chosen to be large to reduce the computer time requirements, higher harmonics or combinations of these frequencies could not be resolved by the calculations.

Configuration 3: This configuration differs from the previous two in that a cavity forms between the step and the partially blocked downstream boundary. The cavity has a distinct acoustic frequency of its own, which differs from the quarter wave acoustic frequency of the system based on the length of the configuration.

Calculations for this configuration were done, and results analyzed using techniques identical to those employed for configurations 1 and 2. In Fig. 9, the u -component of velocity and pressure at selected locations within the shear layer is plotted as a function of time. A visual examination of this near sinusoidal variation indicates that it occurs at a frequency equal to the natural acoustic frequency of the cavity. In this case, the velocity profile downstream of the step tended to vary rapidly from one time level to the other, so that a single shear layer roll up frequency could not be found. A Fourier analysis of the velocity and pressure variations showed only one significant peak, corresponding to the natural acoustic frequency of the cavity.

CONCLUSIONS

The behavior of free shear layers within 2-D dump combustors has been analyzed using numerical solution of time-dependent Navier-Stokes equations. The computed flow fields have been analyzed using vorticity contour plots, Fast Fourier transform of the pressure fluctuations, and linear, inviscid stability analysis of the shear layer. The following conclusions may be drawn, based on the present study.

1) Boundary conditions play a crucial role in the behavior of the flow within the combustor. For example, when the downstream boundary is blocked the shear layer tends to oscillate at the cavity frequency, rather than the system frequency.

Changing the length of the configuration leads to large variations in the system response, when monitored as a function of time.

2) The shear layer tends to lock onto the natural acoustic frequency of the system (or of the cavity). The flapping motion of the shear layer was accompanied by vortex shedding, and pairing in the cases studied.

3) Fourier spectra of the pressure fluctuations within the system show a second, somewhat weaker peak, at the shear layer instability frequency. Some of the higher frequencies found in the Fourier spectra appear to be combinations or multiples of these two basic frequencies.

ACKNOWLEDGEMENTS

This work was supported by the Office of Naval Research under Contract No. N0014-84-K-0293. Computer time for the calculations was provided by the University of Pittsburgh Supercomputer Center.

REFERENCES

1. Strahle, W. C., Davis, J. A. and Sankar, L. N., "Acoustic Response of Turbulent Reacting Recirculating Flows," Proceedings of the 23rd JANNAF Combustion Meeting, October 1986.
2. Strahle, W. C. and Davis, J. A., "Acoustic-vortical Interaction in a Complex Turbulent Flow," AIAA Paper 88-0595.
3. Davis, J. A., Komerath, N. M., Walterick, R. E., Strahle, W. C. and Lekoudis, S. G., "Acoustic Behavior of an SFRJ Simulator," AIAA Paper 86-0003.
4. Visbal, M. and Hankey, W., "Numerical Simulation of a Non-Reacting Unsteady Flow in a Dump Combustor Configuration," AIAA Paper 86-1118.
5. Jou, W. and Menon, S., "Numerical Simulation of the Vortex-Acoustic Wave Interaction in a Dump Combustor," AIAA Paper 86-0002.
6. Menon, S. and Jou, S., "Simulations of Ramjet Combustor Flow Fields, Part I- Numerical Model, Large Scale and Mean Motions," AIAA Paper 87-1421.
7. Kailasanath, J., Gardner, J., Boris, J. and Oran, E., "Numerical Solution of the Flow Field in a Central Dump Ramjet Combustor," NP: Memorandum Report 5832, July 1986.
8. Beam, R. and Warming, R., "An Implicit Factored Scheme for the Compressible Navier-Stokes Equations," AIAA Journal, Vol. 16, No. 4, 1978.
9. Sankar, L.N. and Tang, W., "Numerical Solution of Unsteady Viscous Flow past Rotor Sections," AIAA paper 85-0129.

APPENDIX

All the calculations were performed in a stretched Cartesian coordinate system (ξ, η, τ) which is linked to the physical coordinate system

according to the following one-to-one relationship:

$$\xi = \xi(x) ; \eta = \eta(y) ; \tau = t \quad (1)$$

The Jacobian of transformation J is given by

$$J = \xi_x \eta_y \quad (2)$$

and the metrics of transformation are given by

$$\xi_x = J \eta_{,\eta} ; \eta_y = J \xi_{,\xi} \quad (3)$$

Standard central differences were used to compute quantities such as $x_{,\xi}$, $x_{,\eta}$ etc. which in return were used to compute quantities such as $\xi_{,x}$, $\xi_{,y}$ etc. At the solid surface and the inflow/outflow boundaries, three-point one-sided differences were used to compute the metrics.

In the (ξ, η, τ) coordinate system, the two-dimensional, unsteady Navier-Stokes equations may be written as

$$q_{,\tau} + F_{,\xi} + G_{,\eta} = R_{,\xi} + S_{,\eta} \quad (4)$$

where

$$q = J^{-1} \{ \rho, \rho u, \rho v, e \} \quad (5)$$

The quantities F, G, R and S are given by

$$F = (\xi_x F) / J$$

$$G = (\eta_y G) / J$$

$$R = (\xi_x R) / J$$

$$S = (\eta_y S) / J \quad (6)$$

and

$$F = \begin{bmatrix} \rho u \\ \rho u^2 + p \\ \rho uv \\ u(e+p) \end{bmatrix} \quad G = \begin{bmatrix} \rho v \\ \rho vx \\ \rho v^2 + p \\ v(e+p) \end{bmatrix}$$

$$R = \begin{bmatrix} 0 \\ \tau_{xx} \\ \tau_{xy} \\ R_4^{xy} \end{bmatrix} \quad S = \begin{bmatrix} 0 \\ \tau_{xy} \\ \tau_{yy} \\ S_4^{yy} \end{bmatrix} \quad (7)$$

The quantities R_4 and S_4 represent the dissipation of energy due to work done by the viscous stresses, and heat conduction along the x- and y- directions respectively. The viscous stresses τ_{xx} , τ_{yy} and τ_{xy} were related to the velocity gradients through Stokes' hypothesis. As mentioned earlier the objective of the present work is to determine the onset of laminar shear layer instability, and no explicit turbulence model has been used in the computations to be presented here.

DISCRETIZATION AND APPROXIMATE FACTORIZATION

Since the governing equations are coupled to each other and are highly nonlinear, a stable, efficient solution procedure is required for solving them. In the present work, the Beam-Warming algorithm was used with some modifications. The viscous terms were explicitly evaluated using information available at earlier steps.

Since the mathematical and numerical formulation of the Beam-Warming algorithm are well known, only a brief description of the solution scheme is given here.

The governing equations are written at a computational node (i,j) in the following finite difference form:

$$\delta_\tau q + \delta_\xi F^{n+1} + \delta_\eta G^{n+1} = \delta_\xi R^n + \delta_\eta S^n - \epsilon_\xi D^n \quad (8)$$

where for example, the term $\delta_\xi F^{n+1}$ is the standard two point central difference formula given by $(F_{i+1/2}^{n+1} - F_{i-1/2}^{n+1}) / \Delta x$. The quantity D is the artificial dissipation term discussed in the next section.

The highly nonlinear terms F and G at the time level (n+1) were expanded by a Taylor series about a previous time level n as shown below:

$$\begin{aligned} F^{n+1} &= F^n + [DF/Dq]^n (q^{n+1} - q^n) \\ G^{n+1} &= G^n + [DG/Dq]^n (q^{n+1} - q^n) \end{aligned} \quad (9)$$

Here the quantities DF/Dq and DG/Dq are 4x4 matrices which are the Jacobians of the flux vectors F and G with respect to q.

In order to allow large values of the explicit dissipation coefficient ϵ_ξ to be used without instability, and to allow the viscous terms to be treated explicitly, the following implicit dissipation terms were added to the left side of the difference equation (8):

$$-\epsilon_1 J^{-1} (\delta_{\xi\xi} + \delta_{\eta\eta}) J (q^{n+1} - q^n) \quad (10)$$

The coefficient ϵ_1 was taken to be three times the explicit dissipation coefficient ϵ_ξ . A range of ϵ_ξ values between 3 and 5 were used in the calculations reported here.

Equation (8) may be written after the addition of the artificial implicit dissipation terms given by Equation (10), in the following operator form:

$$\begin{aligned} [I + \Delta t \delta_\xi \{DF/Dq\} + \Delta t \delta_\eta \{DG/Dq\} \\ - \epsilon_1 J^{-1} (\delta_{\xi\xi} + \delta_{\eta\eta}) J] (q^{n+1} - q^n) = R^n \end{aligned} \quad (11)$$

where,

$$\begin{aligned} R^n &= -\Delta t (\delta_\xi F + \delta_\eta G)^n + \Delta t (\delta_\xi R \\ &+ \delta_\eta S)^n - \Delta t \epsilon_\xi D^n \end{aligned} \quad (12)$$

The left-hand side operator of Equation (11) was approximately factored into two smaller operators, leading to the following final form:

$$\begin{aligned} [I + \Delta t \delta_\xi \{DF/Dq\} - \epsilon_1 \Delta t J^{-1} \delta_{\xi\xi} J] \\ [I + \Delta t \delta_\eta \{DG/Dq\} \\ - \epsilon_1 \Delta t J^{-1} \delta_{\eta\eta} J] (q^{n+1} - q^n) = R^n \end{aligned} \quad (13)$$

Equation (13) may be solved through the inversion of two block tridiagonal matrix equations, one corresponding to the ξ -direction and the other corresponding to the η -direction. In

order to keep the flow solver simple, the boundary conditions on all the boundaries were explicitly updated after the interior points had been updated using Equation (13).

TREATMENT OF THE EXPLICIT DISSIPATION TERMS

In the earlier Euler and Navier-Stokes equations, researchers used the following form of the artificial dissipation term:

$$D^n = \Delta t J^{-1} [\delta_{\xi\xi\xi\xi} + \delta_{\eta\eta\eta\eta}] (Jq)^n \quad (14)$$

This term is formally of the order of the fourth power of the grid spacing in the physical plane, and is not expected to reduce the overall accuracy of the solution technique. This form was found to give nonphysical overshoots in the vicinity of rapid flow gradients such as shocks. It was found that second order artificial dissipation terms did not exhibit a similar overshoot, but led to highly inaccurate solutions.

A solution to the problem of overshoots was proposed by Jameson. In his approach, the dissipation term was written as a combination of second and fourth order dissipation terms. A sensor, based on the second derivative of pressure turned on the second order dissipation in the vicinity of shocks, and suppressed the fourth order dissipation term. Away from the rapid gradients, the fourth order dissipation form was used. Jameson's approach was implemented in the following study as follows.

The term D was written as

$$\begin{aligned} D = \Delta t J^{-1} [\delta_\eta \{A(1-C_1)\delta_{\eta\eta\eta\eta} - AC_1\delta_\eta\} \\ + \delta_\xi \{B(1-C_2)\delta_{\xi\xi\xi\xi} - BC_2\delta_\xi\}] (Jq)^n \end{aligned} \quad (15)$$

The coefficients C_2 and C_1 are proportional to the second derivatives of pressure, and are defined such that it will of significant value (of the order of unity) only near rapid gradients such as shock waves. Elsewhere, these coefficients are of the order zero, and the expression given in equation (15) leads to a fourth order error in the solution. The coefficients A and B are proportional to the wave speed in the x- and y- directions and provide an upwind flavor to the present scheme.

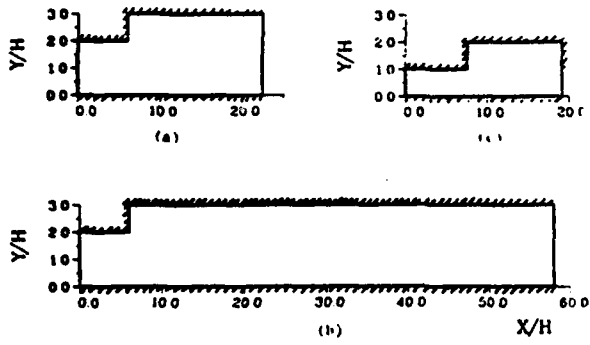


Figure 1. Configurations Studied.

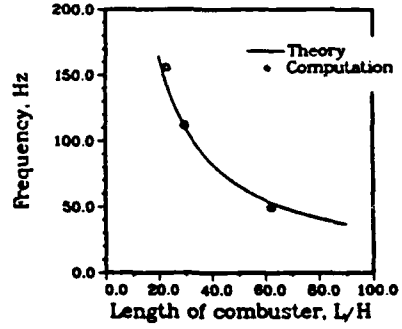


Figure 2. Comparison of Theoretical and Computed Shear Layer Flapping Frequency as a Function of System Length.

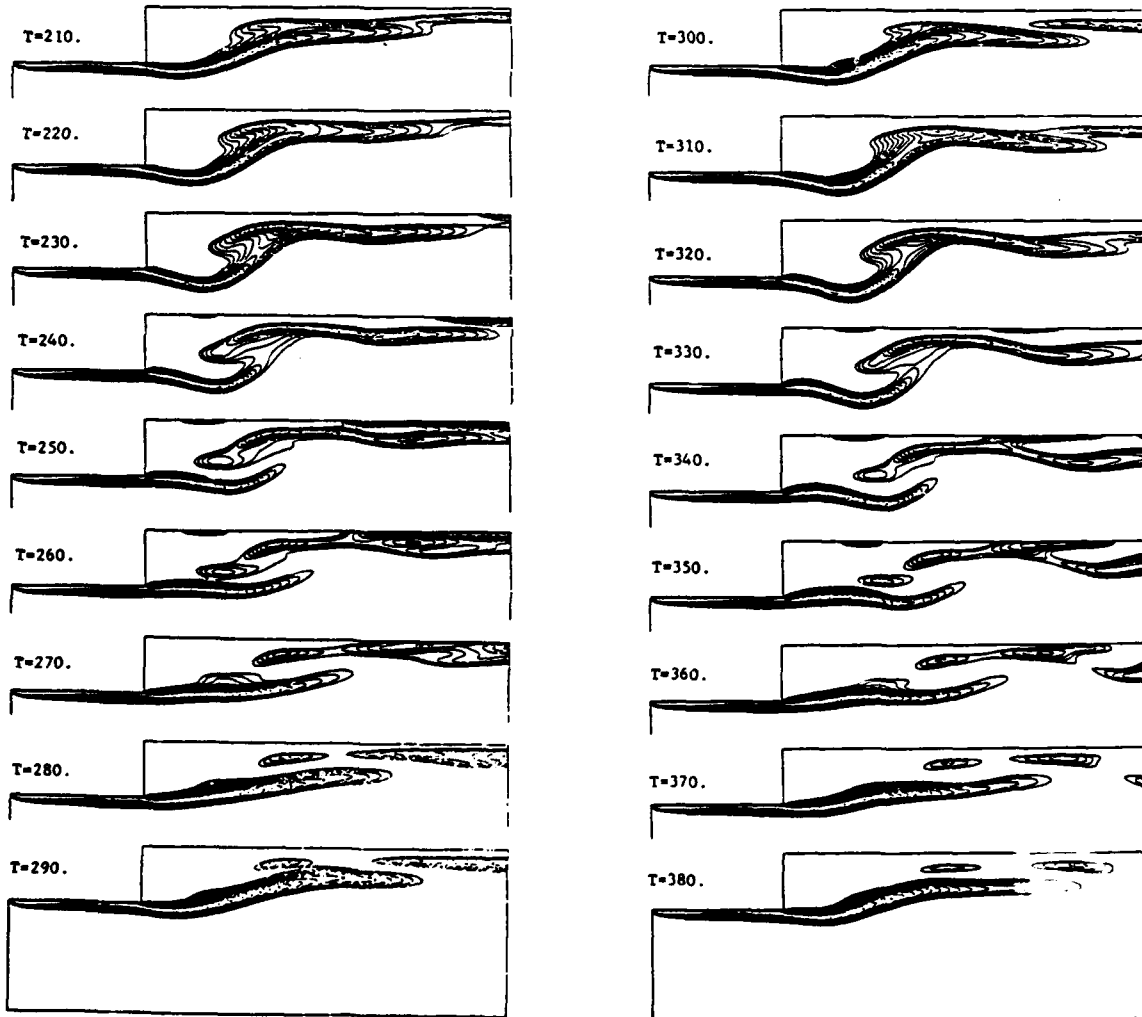


Figure 3. Sample Vorticity Contours at Selected Time Levels for Configuration 1.

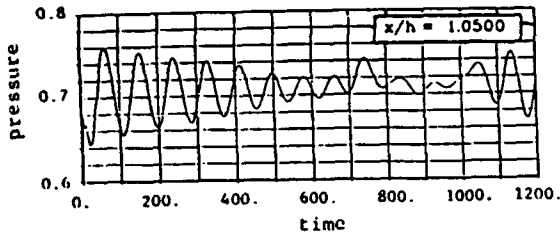


Figure 4. Pressure Time History at a Point Within the Shear Layer ($x/h = 1.05$, $y/h = 0.0$) for Configuration 1.

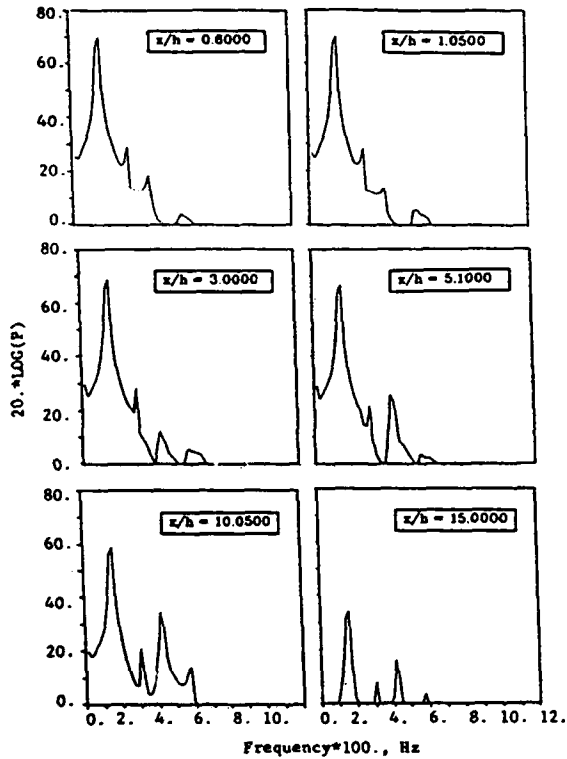


Figure 5. Fourier Spectrum of the Pressure Fluctuations within the Shear Layer for Configuration 1.

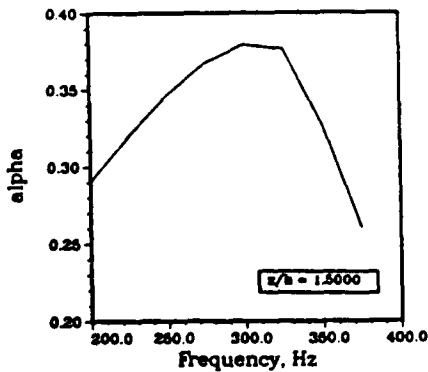


Figure 6. Amplitude of Streamwise Disturbance Growth within the Shear Layer as a Function of Frequency for Configuration 1.

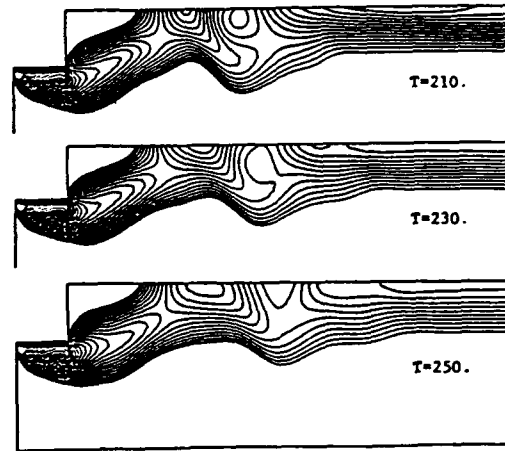


Figure 7. Sample Vorticity Contours at Selected Time Levels for Configuration 2.

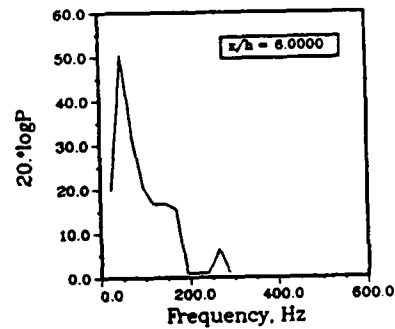


Figure 8. Fourier Transform of Pressure Fluctuations within the Shear Layer for Configuration 2.

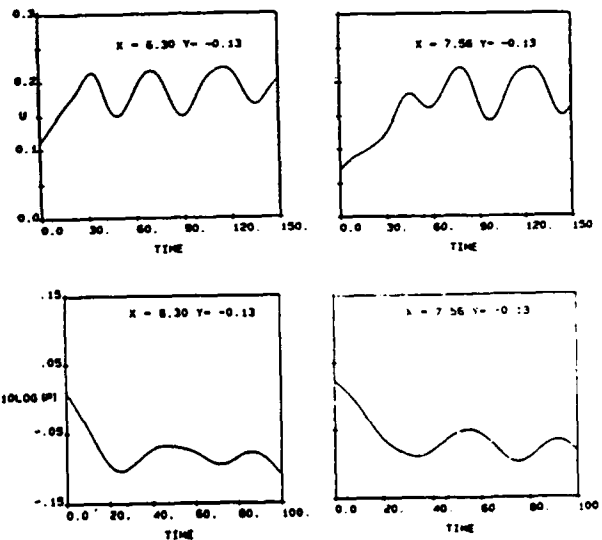


Figure 9. Velocity and Pressure Fluctuations at Selected Points within the Shear Layer for Configuration 3.

AIAA '89

AIAA 89-0981

MIXING ENHANCEMENT IN SUPERSONIC FREE SHEAR LAYERS

W. Tang, L. N. Sankar and N. Komerath
School of Aerospace Engineering
Georgia Institute of Technology, Atlanta, GA 30332

AIAA 2nd Shear Flow Conference

March 13-16, 1989 / Tempe, AZ



For permission to copy or republish, contact the American Institute of Aeronautics and Astronautics
370 L'Enfant Promenade, S.W., Washington, D.C. 20024

MIXING ENHANCEMENT IN SUPERSONIC FREE SHEAR LAYERS

W. Tang¹, L. N. Sankar² and N. Komerath³School of Aerospace Engineering
Georgia Institute of Technology, Atlanta GA 30332

ABSTRACT

The issue of enhancing mixing between parallel, supersonic streams is numerically investigated. An explicit time marching scheme that is second order accurate in time and fourth order accurate in space is used to study this problem. Small amplitude velocity disturbances at selected frequencies are imposed over an otherwise steady flow at the juncture of the two streams to promote mixing. It is found that disturbances are selectively amplified at certain frequencies, while disturbances at other frequencies are rapidly damped out. In studies where the relative Mach number of the disturbances relative to one of the streams is high, shocklets were found to form on one or both sides of the shear layers. In such a situation, the relative Mach numbers of the eddies were different in coordinate systems attached to the upper and the lower streams.

INTRODUCTION

Aircraft engine and missile manufacturers are presently interested in a class of propulsion systems called SCRAMJET engines. In these systems the supersonic airstream captured at the inlet is slowed down to modest supersonic speeds through a series of shock waves prior to entering the combustion chamber. Here the airstream is allowed to mix and react with a parallel stream of fuel or partially burnt fuel/air mixture. For efficient performance of these systems, it is necessary that the fuel and air streams mix with each other as rapidly as possible, over a fairly short distance.

Unfortunately, supersonic free shear layers which form at the juncture of the air and fuel streams tends to grow very slowly [Ref. 1-3] compared to their subsonic counterparts. Alternate mechanisms such as normal injection of fuel into the airstream will likely increase mixing, but at the expense of significant total pressure losses.

Therefore, there is some interest in the use of active and passive control techniques which will promote mixing.

PREVIOUS WORK

A comprehensive discussion of recent experimental, numerical and analytical studies on the behavior of subsonic and supersonic shear layers has been done by Dimotakis [Ref. 4]. Here, only a small subset of existing work, closely related to the present numerical studies, is reviewed.

Experimental Studies: Chinzei et al. [Ref.1] have experimentally studied the growth rate of planar shear layers, using Schlieren techniques, and total pressure probes. They found organized vortical structures to exist in such flows, in a manner similar to subsonic shear layers. Perhaps the best known experimental work on supersonic planar shear layers is that done by Papamoschou and Roshko [ref. 2,3], for a variety of gases and flow conditions on either side of the shear layer. They showed that the convective Mach number of the eddies is a significant parameter governing the growth rate of supersonic shear layers. Papamoschou also performed stability analyses of infinitely thin shear layers (vortex sheets) to link the growth rate of the shear layer (compared to that of an incompressible shear layer) to the convective Mach number, and derived closed form expressions for the convective Mach number as a function of flow conditions on either side. The idea of convective Mach number itself is, of course, not new, and has been previously derived by Bogdanoff [Ref. 5]. In a later study [Ref. 6], Papamoschou found that the measured convective Mach number of the eddies matches the analytical predictions only when the convective Mach number is low and subsonic. He attributed this discrepancy to the fact that the traditional derivations for the convective Mach number assume the total pressure on either side of the shear layer to be equal. In cases where the convective Mach number is high, shocklets can form and lead to different amounts of total pressure losses on either side of the shear layer. Papamoschou also studied modifications to the trailing edge of the splitter plate which initially

1. Research Engineer, Member AIAA.

2. Associate Professor, Member AIAA.

3. Assistant Professor, Member AIAA.

Copyright © 1989 by L. N. Sankar. Published by the American Institute of Aeronautics and Astronautics, Inc. with Permission.

**THIS
PAGE
IS
MISSING
IN
ORIGINAL
DOCUMENT**

page 2

In order to understand the behavior of supersonic free shear layers at low convective Mach numbers, we investigate its response to arbitrary, user-specified acoustic disturbances over a broad range of frequencies. Sinusoidally varying velocity disturbances at a number of frequencies are introduced at the initial, laminar mixing region of the shear layer. These disturbances grow with time as they are convected downstream and eventually lead to well organized vortical structures. The objective of this work is then to study how the disturbances over the entire spectrum of frequencies behave as they are convected downstream, and to speculate on mechanisms by which energy is transferred from high frequencies to low frequencies and vice versa.

To study behavior of the shear layer at very high convective Mach numbers, we use vorticity and pressure contour plots at a number of time levels to track the velocity of the dominant eddies and compute the relative Mach number of these eddies in a coordinate system attached to either the faster stream or the slower stream. If supercritical Mach numbers arise relative to either stream, then the resultant pressure field is examined for the occurrence of shock waves, expansion waves and their effects on the shear layer growth.

The 2-D compressible Navier-Stokes equations in a strong conservation form are numerically solved, using a modified MacCormack scheme that is second order accurate in time, and fourth order accurate in space. This scheme is suitable for studying phenomena such as propagation of acoustic waves, boundary layer instability, and shear layer instability and has been previously used by several authors [Ref. 22-24]. The flow field is assumed to be laminar.

NUMERICAL FORMULATION

The 2-D, laminar, unsteady, compressible flow is governed by the Navier-Stokes equations which may be formally written as:

$$q_t + F_x + G_y = R_x + S_y$$

where F and G are inviscid flux terms, while R and S are the viscous stress terms.

In this work the above equation was solved using a splitting approach. That is, the solution was advanced from one time level 'n' to the next (n+2) through the following sequence of operations:

$$q^{n+2} = L_x L_y L_{xv} L_{yv} L_{xv} L_y L_x q^n$$

where, for example, the L_x operator involves solution of the following 1-D equation:

$$q_t + F_x = 0$$

This 1-D equation was solved through the following predictor-corrector sequence, recommended by Bayliss et al [Ref.22]:

Predictor Step:

$$q_i^* = q_i^n - \Delta t / (6\Delta x) [7F_i - 8F_{i-1} + F_{i-2}]^n$$

Corrector Step:

$$q_i^{n+1} = (q_i^* + q_i^n) / 2 + \Delta t / (12\Delta x) [7F_i - 8F_{i+1} + F_{i+2}]^*$$

In the above equations, the j - index has been suppressed for clarity.

When the above equation is applied at nodes close to the left and right side boundary, a fourth order accurate extrapolation procedure was used to extrapolate the flux vectors F and F^* needed at nodes outside the computational domain.

The L_y operator requires solution of the equation

$$q_t + G_y = 0$$

using a similar approach.

The operators L_{xv} and L_{yv} correspond to numerical solution of 1-D equations such as

$$q_t - R_x = 0$$

**THIS
PAGE
IS
MISSING
IN
ORIGINAL
DOCUMENT**

4

equivalent to applying a slip boundary condition at these walls. In the case of free, unconfined shear layers, non-reflective boundary conditions are needed at these lateral boundaries. In the present work, setting the derivative of the normal component of velocity to zero, rather than the velocity itself to zero was found to minimize reflections.

The flow properties at the inflow were specified everywhere in the flow field as the initial conditions for the problem. The Navier-Stokes solver was then advanced for several non-dimensional units of time, until a fully developed shear layer with a modest streamwise growth was established.

Once a steady state shear flow was achieved, forced excitation of the shear layer began. This was achieved by prescribing the normal (v -) component of velocity over the entire inflow boundary to behave as follows:

$$v(y,x=0,t) = \sum A_n f(y) \sin(\omega_n t + \theta_n)$$

Here the summation shown is over all the excitation frequencies; A_n is the amplitude of disturbance, ω_n is the frequency of disturbance and θ_n is the associated phase angle. The function $f(y)$ determines the variation of the perturbation velocity across the shear layer. Both a Gaussian distribution and a constant magnitude distribution were attempted. The results to be presented here correspond to $f(y)$ equal to unity.

In the present work 6 frequencies were used, with zero phase difference between the individual components. The quantity A_n was 2% of the reference velocity U_1 . The non-dimensional frequencies ω_n were 10, 20, 30, 40, 50 and 60 respectively. Obviously, a linear stability analysis could have been used to pick the frequencies that are related to the most unstable frequency. But the intent here was to impose excitation at several frequencies on the shear layer, at the inflow boundary and determine which frequencies are selectively amplified, and to determine what happens to the energy content at the higher frequencies at subsequent time levels.

Figure 2 shows the vorticity contours at a randomly selected time level. It is seen that the

vorticity field at the immediate downstream boundary is rich in structure showing large gradients in the streamwise as well as normal directions. At large distances downstream, however, only a single row of eddies at well defined distances are seen.

Because the formation and motion of vortices (or eddies) give rise to a rapidly varying pressure field which moves with the eddies some useful information about the energy content at the shear layer distributed over the various frequencies may be obtained by computing the Fourier transform of the pressure field at a number of points within the shear layer. In figure 3, the Fourier spectrum of the pressure field is plotted at 6 x-locations within the computational field, at $y/\delta = 0$. The following trend is seen. Near the inflow boundary, the Fourier spectrum shows a near uniform distribution over the entire frequency range. At downstream locations, the higher frequency content begins to gradually decrease. The low frequency components at non-dimensional frequencies 10 and 20 show a rapid increase initially, but reaches asymptotically constant values. Figure 4 contains the same information as figure 3, except it shows the changes in energy content as a function of downstream distance. It is seen that Fourier coefficient associated with non-dimensional frequency 60 reduces to 30% of initial value 100 δ downstream, whereas the low frequency component triples in magnitude and reaches its limit value 125 units downstream. An examination of the vorticity contour plot (figure 2) shows a number of small eddies at the inflow boundary, which rapidly merge into a single, large vortex. This merging appears to be the mechanism responsible for the decrease in the energy content at high frequencies, and the corresponding increase at the lower frequencies. It is interesting to note that the two lowest frequency components (corresponding to non-dimensional frequencies 10 and 20) maintain their energy levels once they reach their limit values, with no further transfer of energy from the $\omega_n = 20$ waves to the $\omega_n = 10$ waves. This may be due to the fact that the phase difference in the forcing function corresponding to these two waves was zero.

**THIS
PAGE
IS
MISSING
IN
ORIGINAL
DOCUMENT**

6

In figures 7 and 8, the pressure and velocity contours are plotted at a randomly chosen time level. In this case, from an inspection of the vorticity profiles at adjacent time levels, the eddies appear to travel at substantially lower speed than the upper stream. During the early stages of eddy formation and motion, shocklets occur both on the upper and lower sides of the shear layer. As the eddies accelerate and reach low subsonic Mach numbers relative to the upper stream, the shocklets on the upper side of the shear layer disappear. The shocklets on the lower side continue to travel with the eddies, with no reduction in their strength.

Case 3: Case 1 was repeated, by artificially reducing the shear layer vorticity thickness by a factor of 15, keeping all other dimensions such as the grid size, domain length and width constant. In figures 9 and 10, the pressure and vorticity contours are plotted. Again, in figure 10, the solid and dotted contours correspond to low and high pressure levels respectively. Shocklets are evident on either side of the shear layer, although they are weak because the reduced shear layer thickness leads to small and thin eddies, compared to case 1.

Case 4: As a final exercise, Case 1 was repeated, with forced excitation of the normal velocity at the inflow boundary over multiple frequencies, ranging from 10 to 60. The amplitude of the individual components was 0.02 times the upperstream velocity. In figure 11 the Fourier spectrum of the pressure field at several x- locations are plotted. A gradual migration of energy levels from the higher frequency to the lower frequencies is evident, as in the case of the subsonic convective Mach number case. Figure 12 shows how the two high frequency components decay following a brief initial growth as eddies are convected downstream. The low frequency components at frequencies 10, 20 and 30 initially grow rapidly, but reach asymptotic values.

The response of the shear layer to multiple frequencies is strikingly similar to that in the earlier study for subsonic convective Mach numbers, shown in figures 3 and 4.

CONCLUDING REMARKS

The stability and growth characteristics of supersonic free shear layers were studied by

exciting the shear layer at the upstream boundary with small amplitude normal velocity disturbances. The following observations were made:

a) In the case of shear layers at subsonic and supersonic convective Mach numbers, the imposition of acoustic disturbances over a large range of frequencies lead to the transfer of this energy from the high frequencies to the low frequencies, as the flow progressed from the upstream boundary to the downstream boundary. The energy content at the lowermost frequencies rapidly reached asymptotic values following which eddies in the shear layer were convected downstream with no further alteration in their structure.

b) In the case of shear layers at a supersonic convective Mach number, situations were found where the convective Mach number relative to the faster stream is low. This leads to a situation where shocklets arose only on the lower side of the shear layer. Conditions were also found where the convective Mach number relative to both the streams is high, leading to shocklets on either side. These calculations demonstrate the same features experimentally observed by Papamoschou [Ref. 3] and discussed based on total pressure arguments by Dimotakis [Ref 4].

ACKNOWLEDGEMENTS

This work was supported by the Office of Naval Research under Grant No. N00014-89-J-1319. Computer time for the numerical simulations was provided by the Pittsburgh Supercomputing Center. The authors are thankful to Prof. S. A. Ragab of Virginia Polytechnic Institute & State University for several valuable discussions.

REFERENCES

1. Chinzei, N., Masuya, G., Komuro, T., Murakami, A. and Kudou, K., "Spreading of Two-Dimensional Supersonic Mixing Layers," *Physics of Fluids*, Vol. 29, pp1345-1347.
2. Papamoschou, D., "Experimental Investigation of Heterogeneous Compressible Shear Layers," Ph. D. Dissertation, Cal Tech, 1986.

**THIS
PAGE
IS
MISSING
IN
ORIGINAL
DOCUMENT**

8

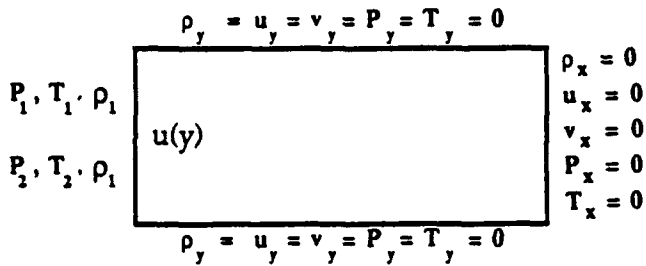


Figure 1. Computational domain

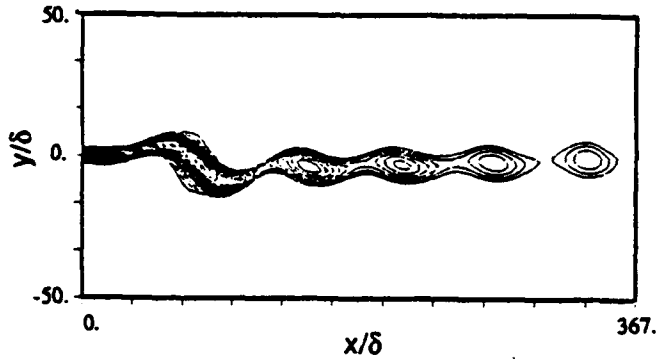


Figure 2. Vorticity Contours for a shear layer excited at multiple frequencies; $Mc=0.2$, $M_1=4.0$, $M_2=2.3$, $a_1/a_2=2.3$, $\delta=1/15$.

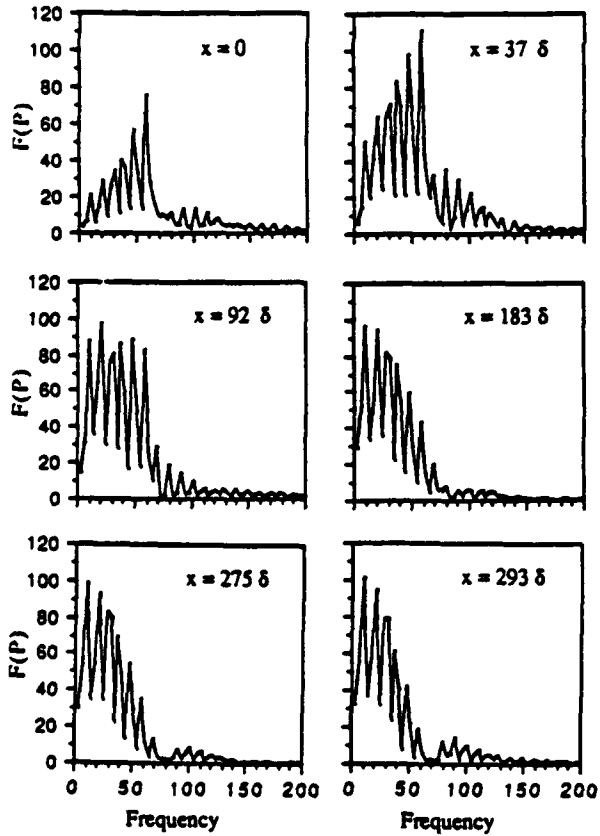


Figure 3. Fourier spectrum of pressure field at selected x-locations within the shear layer; $Mc=0.2$, $M_1=4.0$, $M_2=2.3$, $a_1/a_2=2.3$, $\delta=1/15$.

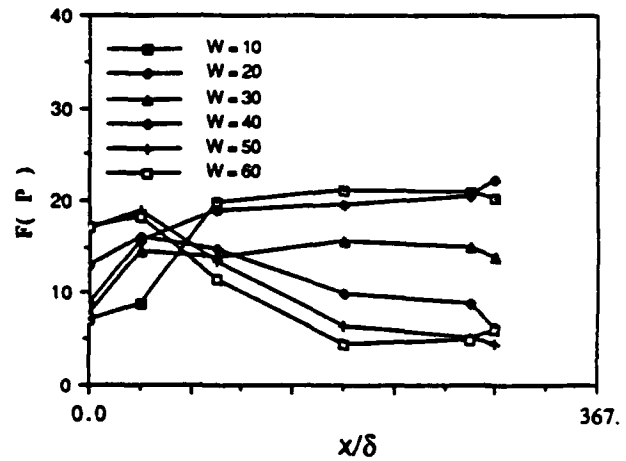
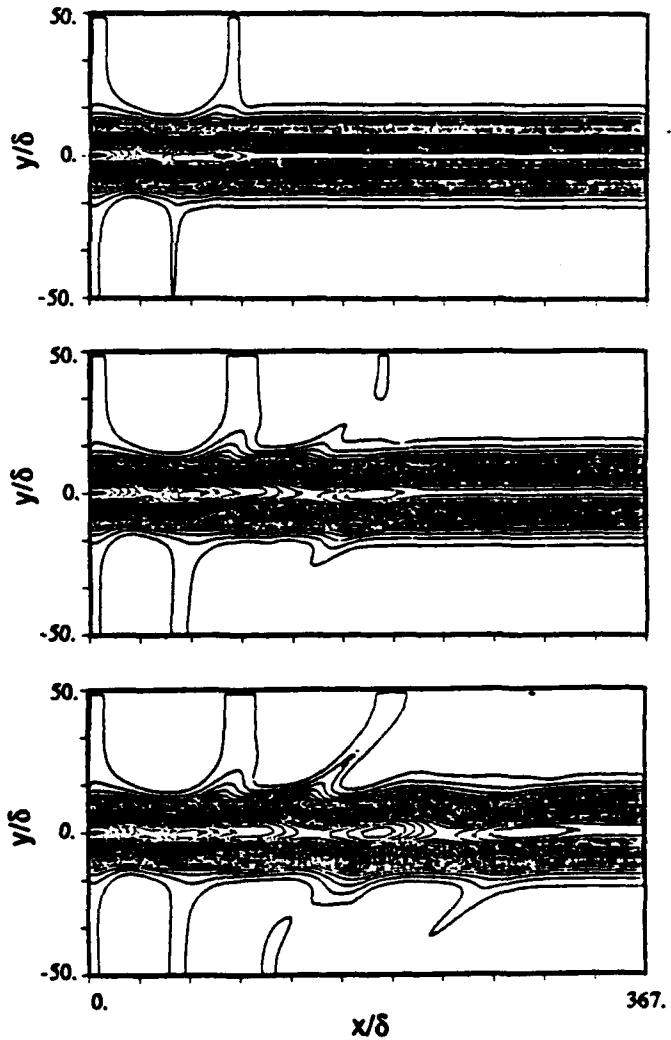


Figure 4. Variation of Fourier spectrum as a function of streamwise location; $Mc=0.2$, $M_1=4.0$, $M_2=2.3$, $a_1/a_2=2.3$, $\delta=1/15$.



**THIS
PAGE
IS
MISSING
IN
ORIGINAL
DOCUMENT**

10

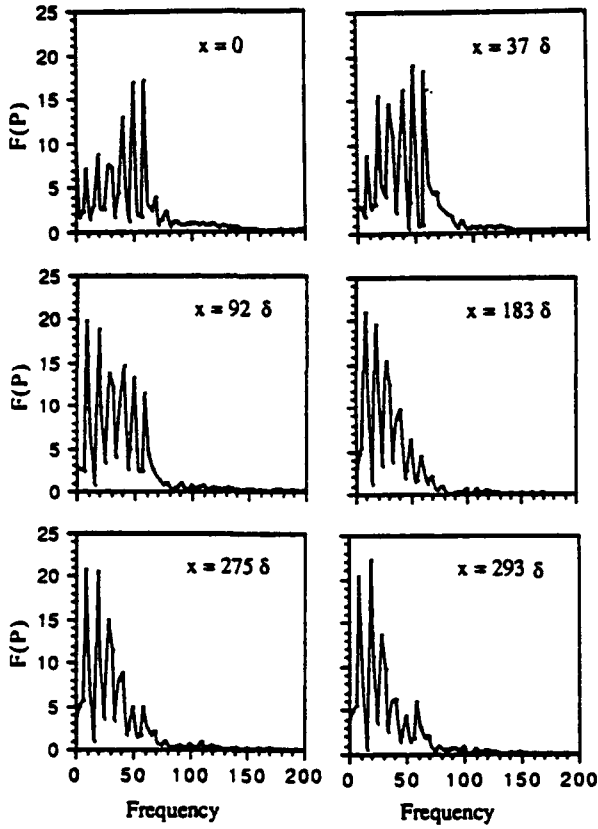


Figure 11. Fourier spectrum of pressure field at selected x -locations within the shear layer; $Mc=1.2$, $M_1=6.0$, $M_2=3.6$, $a_1/a_2=1.0$, $\delta=1/15$.

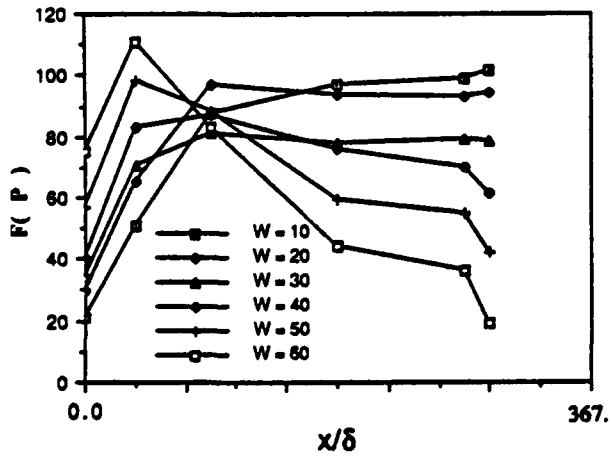


Figure 12. Variation of Fourier spectrum as a function of streamwise location; $Mc=1.2$, $M_1=6.0$, $M_2=3.6$, $a_1/a_2=1.0$, $\delta=1/15$.

Numerical Simulation of the Growth of Instabilities in Supersonic Free Shear Layers

W. Tang,* N. M. Komerath,† and L. N. Sankar‡
Georgia Institute of Technology, Atlanta, Georgia

The behavior of the initial region of a supersonic plane shear layer is analyzed through numerical solution of the two-dimensional Navier-Stokes equations, as well as the three-dimensional equations under the finite-span assumption. A modified MacCormack scheme that is fourth-order accurate in space and second-order in time is employed. Small amplitude oscillations in the normal velocity are found to grow as they convect downstream, and eventually lead to organized vortical structures. Normal velocity disturbances are found to be more efficient than streamwise or spanwise disturbances. The growth rate of these disturbances, as well as the intensity of velocity fluctuations, are found to decrease as the convective Mach number of the shear layer increases. The Mach number of the vortical structures with respect to the faster stream is found to be considerably less than the theoretical value of the convective Mach number.

Nomenclature

a_1	= upper stream speed of sound
a_2	= lower stream speed of sound
F, G	= flux vectors
M_{vortex}	= convective Mach number of present result
M_c	= convective Mach number
q	= vector of conserved variables
R, S	= diffusion vectors
U_c	= convection speed of vortices
U_1	= upper stream inflow velocity
U_2	= lower stream inflow velocity
x	= coordinate in streamwise direction
y	= coordinate in normal direction

Introduction

AIR-BREATHING engines designed for high-flight Mach numbers require supersonic combustion for efficient operation. The shock losses associated with deceleration to low Mach numbers require that the mixing of fuel and air, and the heat release, must occur in supersonic flows. For the same reason, it is desirable to mix the fuel and air using coflowing streams. In such configurations, the mixing must occur across the shear layer formed between the streams. The length and weight of the engine, and the efficiency of heat release, depend on the rapidity of this mixing process. Most current concepts for supersonic-combustion ramjets thus employ mixing-limited heat release. The mixing across a shear layer between two streams depends on the rate of mass and momentum transfer across the layer, and, hence, can be described using the "growth" or "spreading" rate of the shear layer. Unfortunately, shear layers separating supersonic streams are known

to grow much more slowly than corresponding subsonic shear layers.

One long-term objective of supersonic shear layer research, therefore, is to devise methods of increasing the mixing between supersonic streams by enhancing the shear layer growth rate. Recent success in greatly modifying subsonic shear layers has resulted in the advancement of a variety of schemes for achieving similar increases in supersonic shear layers. The variety of such possibilities far exceeds the resources available for experimental exploration of each. Instead, a better approach appears to be to develop reliable numerical models and solution methods that can then be used to perform the exploration, and to identify promising approaches and the appropriate values of parameters required. This is the motivation behind the research described in this paper.

Previous Work

Chinzei et al.¹ conducted experiments on planar shear layer configurations and studied the growth rate. Papamoschou² conducted similar experiments, using a variety of gases and flow conditions, and showed that the results could be scaled using the convective Mach number of the dominant eddies in the shear layer. These results showed that the growth rate of supersonic shear layers is typically less than one-third the growth rate of incompressible shear layers for convective Mach numbers greater than unity.

Passive and active control techniques have been studied by other researchers. These techniques are generally based on the principle that if vorticity is introduced into the shear layer, it will increase the level of fluctuation and, therefore, promote mixing and growth. Guirguis³ and Drummond and Mukunda⁴ studied the effect of a bluff body placed in the middle of the shear layer. Kumar et al.⁵ considered the effects of vorticity produced by a pulsating shock wave on the growth characteristics of the shear layer. Ragab and Wu⁶ have developed calculations based on stability theory to predict the response of supersonic shear layers. Recently,⁷ they have also developed computations of the response of planar wakes and shear layers similar to those in experimental splitter plate configurations.

Scope of Present Paper

In the work presented here, the behavior of a planar free shear layer is studied, using two numerical techniques for solution of the Navier-Stokes equations. The effects of active

Received Dec. 2, 1988; presented as Paper 89-0376 at the 27th Aerospace Sciences Meeting, Reno, NV, Jan. 9-12, 1989; revision received June 3, 1989. Copyright © 1989 American Institute of Aeronautics and Astronautics, Inc. All rights reserved.

*Research Engineer II, School of Aerospace Engineering. Member AIAA.

†Assistant Professor, School of Aerospace Engineering. Member AIAA.

‡Associate Professor, School of Aerospace Engineering. Member AIAA.

control strategies are investigated. Sinusoidal variations in the velocity are introduced at the upstream boundary. The subsequent response of the shear layer to these disturbances is studied. Streamwise, normal, and spanwise disturbances are considered as suitable candidates for promoting mixing.

At present, the problem is assumed to be nominally two-dimensional. Some calculations have been performed with three-dimensional layers under the infinite sweep assumption. It is recognized that the later development of the shear layer may be strongly influenced by three-dimensional effects. However, there is no reason to believe that the initial region should be anything other than two-dimensional. The available experimental flow visualizations, performed with spanwise-integrating techniques such as schlieren and shadowgraphy, clearly show structures that would have been totally smeared out if the flowfields had been significantly three-dimensional.

The present calculations are for laminar shear layers, and no turbulence model is used. Turbulence models inherently bring additional uncertainty into the physical interpretation of the observed behavior of the flowfield, though they are certainly necessary to obtain quantitative accuracy. The lack of such a model restricts the applicability of these results to the initial region of the shear layer.

The initial velocity profile used is a step change in velocity at the slip line between the two streams. Thus, the results obtained will not correspond to experimental results from splitter-plate configurations, since there is no boundary layer and no embedded region of initially subsonic flow.

Within the above limitations, the present work aims to study the behavior of the initial region of a shear layer, and to explore the effects of various forms of excitation.

Problem Statement

The shear layer configuration is shown in Fig. 1. Two uniform, parallel supersonic streams of different Mach numbers are released at the left-hand boundary. All properties are known at this boundary. The upper and lower boundaries of the computational domain are assumed to be hard walls across which no disturbances can escape. There is no boundary layer at these walls, and slip conditions are used. At the downstream boundary, the flow and all disturbances are allowed to escape, and no disturbances are allowed to propagate back.

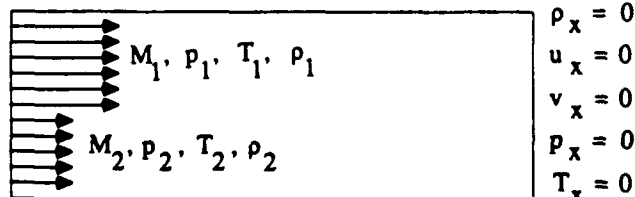
To study shear layer behavior, the static pressures are equalized across the splitter plate, so that there are no strong shocks in the flow. Some waves and their reflections from the wall do occur, but these are quite weak.

The flow is assumed to be nonreacting, and the ratio of specific heats was assumed to be constant for both streams. The species above and below the shear layer were assumed to have the same molecular weight.

Mathematical Formulation: Fourth Order MacCormack Scheme

$$q_t + F_x + G_y = R_x + S_y \quad (1)$$

$$\rho_y = u_y = p_y = T_y = 0, \quad v = 0$$



$$\rho_y = u_y = p_y = T_y = 0, \quad v = 0$$

Fig. 1 Boundary conditions for supersonic free shear layer.

Here, F and G are the inviscid flux terms and account for the transport of mass, moment, and energy and for the influence of pressure. The terms R and S are the viscous stress terms. The above equation is parabolic with respect to time, and may be solved using a variety of stable time marching schemes. For two-dimensional flows, there are four equations. In the case of three-dimensional flows subject to infinite-sweep assumption, there are five equations, the additional equation corresponding to the conservation of spanwise momentum.

In this work, the above equation was solved using a splitting approach; that is, the solution was advanced from one time level ' n ' to the next ' $n+2$ ', through the following sequence of operations:

$$q^{n+2} = (L_x L_y L_{xv} L_{yv} L_{xy} L_{yx} L_x) q^n \quad (2)$$

where, for example, the L_x operator involves solution of the following equation:

$$q_t + F_x = 0 \quad (3)$$

This one-dimensional equation was solved through the following predictor-corrector sequence, recommended by Bayliss et al.⁸:

Predictor Step:

$$q_{i,j}^* = q_{i,j}^n - \frac{\Delta t}{6\Delta x} \left[7F_{i,j} - 8F_{i-1,j} + F_{i-2,j} \right] \quad (4)$$

Corrector Step:

$$q_{i,j}^{n+1} = \frac{1}{2} \left(q_{i,j}^n + q_{i,j}^* \right) + \frac{\Delta t}{12\Delta x} \left[7F_{i,j} - 8F_{i-1,j} + F_{i-2,j} \right] \quad (5)$$

When the above equations are applied at nodes close to the left- and right-side boundary, a fourth-order accurate extrapolation procedure was used to extrapolate the flux vectors F and F^* needed at nodes outside the computational domain.

The L_y operator requires solution of the equation

$$q_t + G_y = 0 \quad (6)$$

using a similar approach.

The operators L_{xv} and L_{yv} correspond to numerical solution of one-dimensional equations such as

$$q_t - R_x = 0 \quad (7)$$

The above equation was solved through the following two-step sequence:

$$q_{i,j}^* = q_{i,j}^n + \frac{\Delta t}{\Delta x} \left[R_i + \frac{1}{2} j - R_i - \frac{1}{2} j \right]^n \quad (8)$$

$$q_{i,j}^{n+1} = \frac{1}{2} \left(q_{i,j}^n + q_{i,j}^* \right) + \frac{\Delta t}{2\Delta x} \left[R_i + \frac{1}{2} j - R_i - \frac{1}{2} j \right]^* \quad (9)$$

The viscous terms are thus updated only to second-order accuracy in space. It may be shown that the above scheme has very little artificial dissipation inherent in it, and is fourth-order accurate in space, as far as the inviscid part is concerned.

Boundary Conditions

As stated above, all flow properties are prescribed at the upstream boundary for both streams, including any imposed perturbations. At the downstream boundary, the flow is assumed to remain fully supersonic for the small-amplitude perturbations encountered in this work, so that the properties may be extrapolated from the interior. Alternatively, the governing equations themselves may be applied if the streamwise diffusion terms R_x are suppressed at the downstream nodes.

At the lateral boundaries, the flow is assumed to be confined by smooth, parallel walls. Slip boundary conditions were used to avoid the compression effects that would be caused by boundary layers. The walls were considered adiabatic, and the normal derivatives of density and pressure were set to zero.

Results and Discussion

Normalization

Velocities were normalized using the speed of sound in the upper stream, which thus became unity. The Reynolds number based on the speed of sound was chosen to be 1000. A 221×61 uniform grid was used, with spacing of 0.01 in each direction. Thus, the length of the domain L was 2.2. The time step was taken as 0.001 (0.0005 for each half-step). The calculations were started with step velocity profiles at the upstream boundary, and allowed to proceed until a steady state was reached asymptotically. This usually took 600 time steps. The results at this stage were stored, and the code was restarted with an imposed sinusoidal velocity disturbance of amplitude 2% of the velocity of the upper stream. The calculations were then run until several cycles of the disturbance had been completed, and the initial effects had been convected away through the downstream boundary.

Convective Mach Number

The cases run have been summarized in Table 1. Because the supersonic shear flow problem involves several parameters (at least five on either side of the shear layer), nondimensional groupings are sought to express observed effects. Following the practice of Papamoschou,² the convective Mach number was used here. For the problem studied here, the convective Mach number reduces to

$$M_c = (U_1 - U_c) / a_1$$

where

$$U_c = (a_1 U_2 + a_2 U_1) / (a_1 + a_2)$$

The values of M_c calculated by this formula are tabulated. A physical interpretation of the convective Mach number is that it is the Mach number of the dominant large-scale vortical structures with respect to either stream. According to the formula given above, this Mach number is the same with respect to either of the streams. An attempt was made, as discussed later, to determine the convection speed of the vortical structures seen in the computational flowfield, and to determine relative Mach numbers from them. The Mach numbers so determined, with respect to the upper, high-speed stream, are also tabulated. It is seen that there is a considerable discrepancy. This is not surprising, and, in fact, even in subsequent experiments by Papamoschou,⁹ similar effects appear to have been observed.

Table 1 Cases presented

Case	M_1	M_2	U_1	U_2	M_c	M_{vortex}
1	4.0	2.3	4.00	3.51	0.20	0.2
2	4.0	2.0	4.00	3.05	0.38	0.2
3	4.0	1.3	4.00	1.98	0.80	0.2
4	5.0	1.3	5.00	1.98	1.20	0.6

Formation of Vortical Structures

Figure 2a shows the contours of vorticity in the shear layer, calculated for case 1, with no disturbance superposed. It is seen that the shear layer grows quickly at the very beginning, and then takes on a smooth profile which grows very little thereafter. It should be remembered that in this calculation there is no imposed turbulence model. Figure 2b shows the effect of imposing a sinusoidal 2% normal velocity disturbance at the inflow boundary. Distinct centers of vorticity are seen to develop and be convected downstream. The shear layer edge now penetrates considerably further into both streams. Careful examination of the contours shows considerable asymmetry and distortion as the structures proceed downstream. The computational domain in this calculation does not extend far enough for these disturbances to grow into the nonlinear regime, and hence no "roll-up" can be expected here. The effects of six cycles of the imposed disturbance can be seen, with the sixth just leaving the computational domain.

Figures 3a and 3b show the corresponding vorticity contours for case 2, where the theoretical value of convective Mach number is nearly twice that of case 1. The growth rate

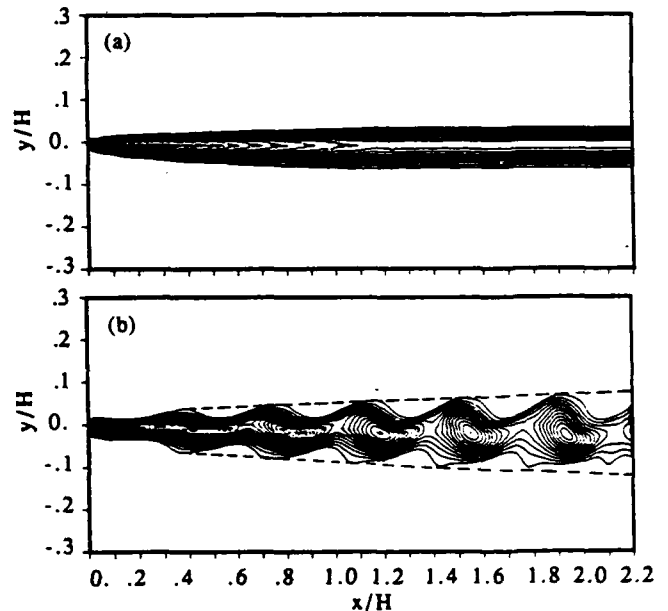


Fig. 2 Vorticity contours for case 1, $M_1 = 4.0$, $M_2 = 2.3$, $M_c = 0.2$; a) without disturbance, b) with disturbance in the normal direction.

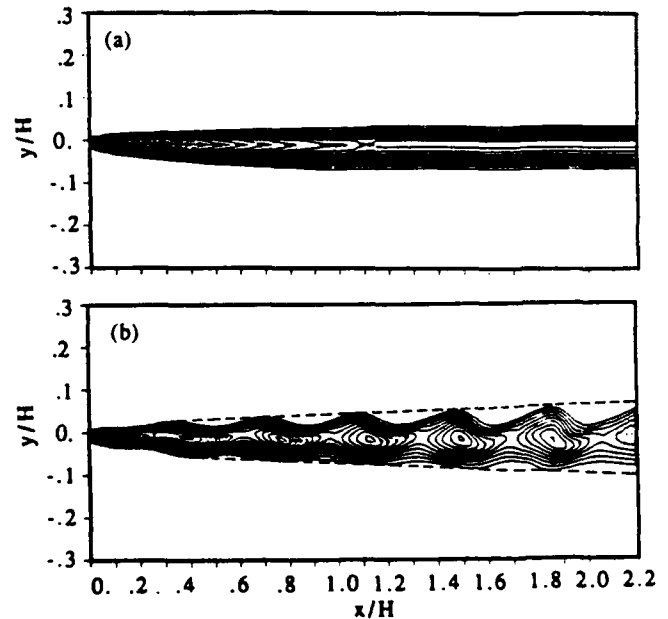


Fig. 3 Vorticity contours for case 2, $M_1 = 4.0$, $M_2 = 2.0$, $M_c = 0.38$; a) without disturbance, b) with disturbance in the normal direction.

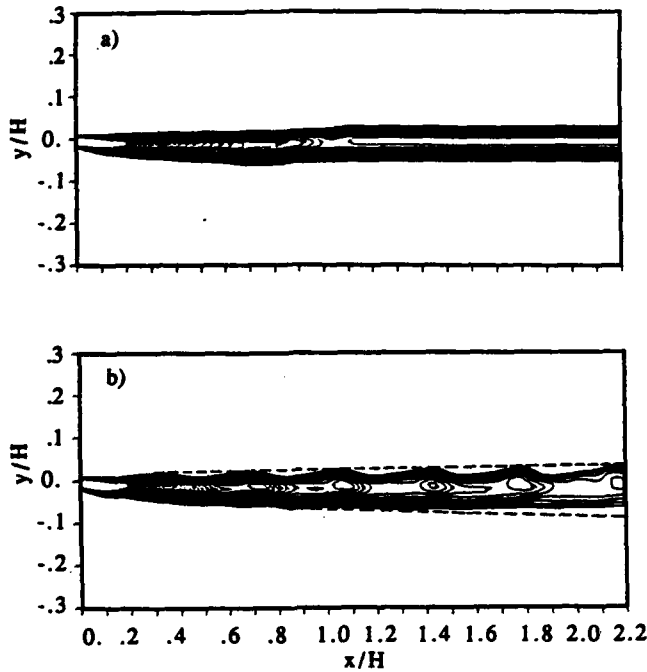


Fig. 4 Vorticity contours for case 3, $M_1 = 4.0$, $M_2 = 1.3$, $M_c = 0.8$; a) without disturbance, b) with disturbance in the normal direction.

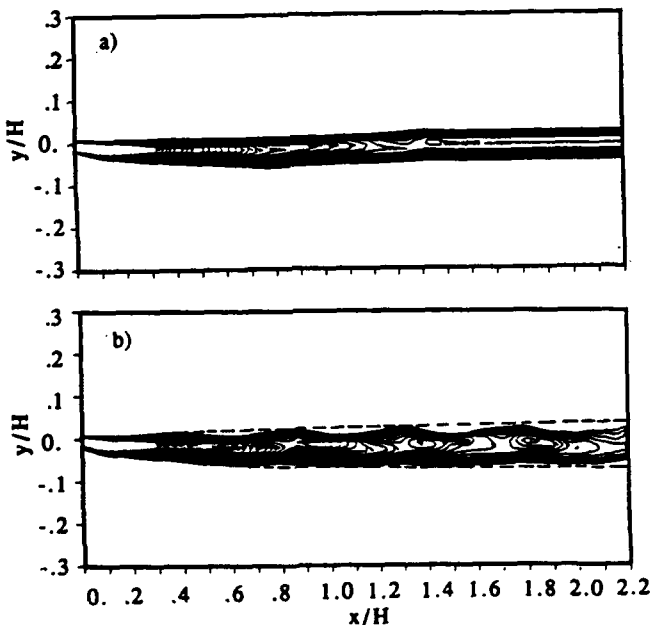


Fig. 5 Vorticity contours for case 4, $M_1 = 5.0$, $M_2 = 1.3$, $M_c = 1.2$; a) without disturbance, b) with disturbance in the normal direction.

appears to be less, as expected from the experimental observations of the effect of M_c . This effect is seen further in Figs. 4 and 5, where the convective Mach number, according to the formula, is 0.8 and 1.2, respectively.

Disturbance Type

Other kinds of disturbance were tried; specifically, disturbances in velocity along the streamwise direction for the two-dimensional shear layer and disturbances along the spanwise direction using a three-dimensional model with the infinite sweep assumption. The results are shown in Figs. 6 and 7, respectively, for the case where the convective Mach number is predicted to be 0.2. In each case, the disturbance amplitude is the same. It is seen that these types of disturbances are less efficient than the normal velocity disturbance.

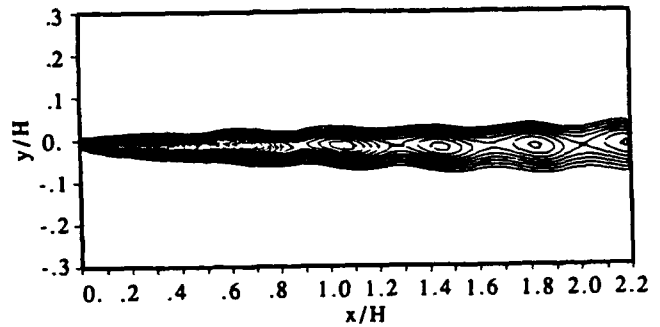


Fig. 6 Effect of streamwise disturbances for case 1.

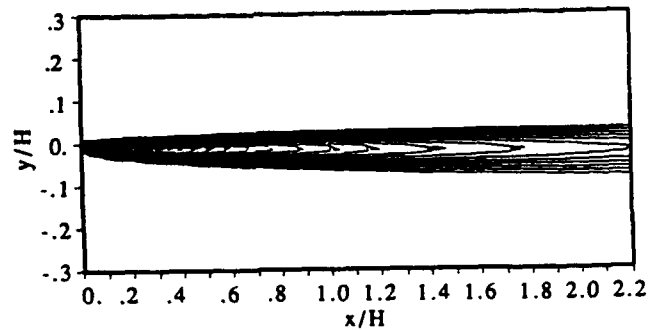


Fig. 7 Effect of spanwise disturbances for case 1.

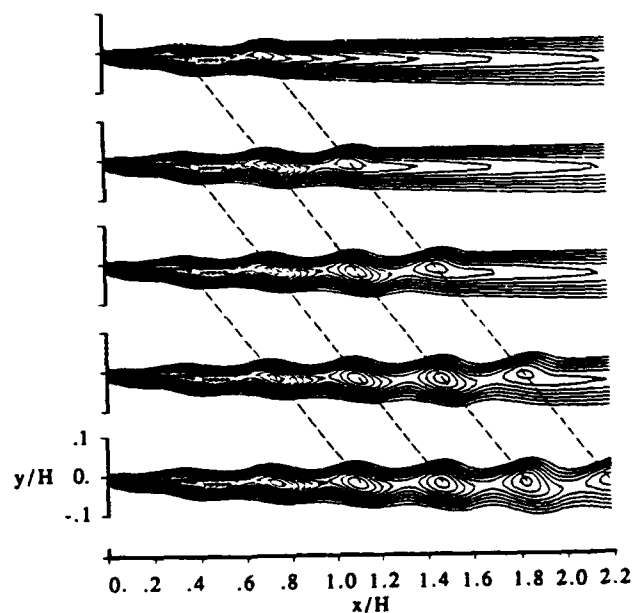


Fig. 8 Computation of convective speed based on the temporal evolution of vorticity contours for case 2.

Convective Speed Based on Evolution of Vorticity Contours

One common way of calculating the convective Mach number is to track the downstream convection of the vorticity contours as a function of time. The results of this effort are shown in Fig. 8 for case 2. Similar computations were performed for all of the cases, and the results are shown in Table 1. It is seen that as the theoretical value of the convective Mach number rises, the measured convective Mach number of the structures with respect to the upper stream vary much less. Of course, this means that the convective Mach number is no longer the same when compared to the two streams. The structures appear to move at a speed that is close to that of the upper, high-speed stream. This is similar to the more recent observations of Papamoschou,⁹ where the structures were found, for many cases, to move at speeds close to that of one or the other stream.

Growth Rate Enhancement

The thickness of the shear layer was computed from the velocity profiles across the shear layer. These profiles are shown later in the paper, where they are used to examine the numerical accuracy of the results. Figure 9 shows the shear layer thickness for unperturbed and perturbed cases for case 1. The disturbed case shows a significantly greater rate of growth, except near the downstream boundary. However, the increase in growth rate is only on the order of 10-15%.

The frequency of the imposed fluctuations was chosen such that about six vortical structures could be seen in the computational domain at one time. Thus, the actual frequency used was higher than the frequency of maximum amplification predicted by linear stability analysis. Use of the preferred frequency would have required a much larger computational domain in the x direction to capture an adequate number of vortices, and would have increased the computational effort required by an order of magnitude.

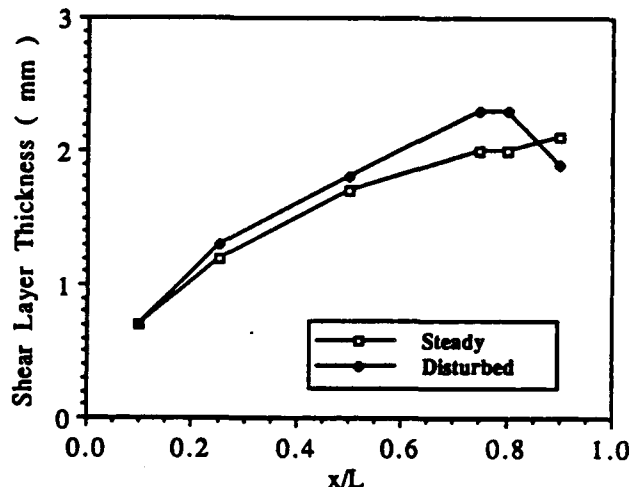


Fig. 9 Shear layer thickness.

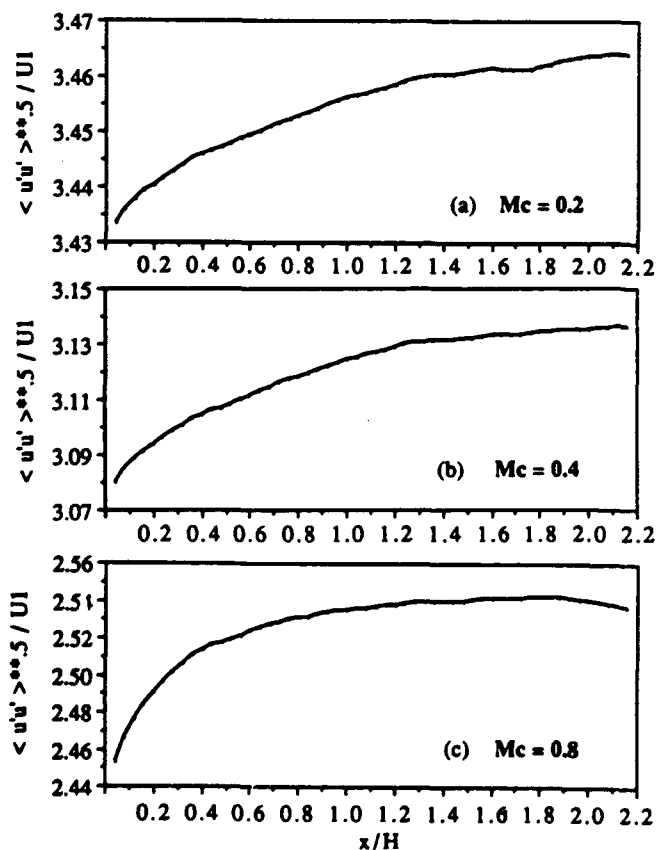


Fig. 10 Effect of convective Mach number on fluctuation in the shear layer; a) $M_c = 0.2$; b) $M_c = 0.38$; and c) $M_c = 0.80$.

The intensity of fluctuation in the shear layer is plotted as a function of downstream distance for three cases with different theoretical convective Mach numbers in Figs. 10a-10c. The quantity measured was the root-mean-squared fluctuation of the U -component of velocity about the mean, normalized by the mean velocity. It is to be noted that this is not the turbulence intensity, since no attempt has been made to model the turbulence. The fluctuations have their origin in the imposed disturbance, though they may have been selectively amplified by energy exchange with the shear layer. It is seen that the intensity of fluctuations decreases rapidly with increasing convective Mach number. It also appears that the intensity quickly reaches an asymptotic value and does not increase further. In fact, for the higher values of convective Mach number, the intensity appears to peak and then decrease gradually thereafter. This decay in the intensity with high values of M_c has been predicted by other researchers using linear stability analysis.

Studies of Discretization Error

All the above results were generated using the fourth-order MacCormack scheme. The influence of the accuracy of the computation scheme was studied by comparing results obtained using a second-order MacCormack scheme to those obtained with the fourth-order scheme. Velocity profiles across the shear layer were used to examine the results. Figure 11 shows the comparison for case 1, however, with a 111×31 grid. The profile was obtained at the station 10% of the domain length downstream of the origin. The results are seen to be quite similar. The agreement is close for profiles at 25 and 50% downstream. However, at $x/L = 0.75$, differences can be clearly seen. The fourth-order scheme is seen to resolve spatial details better, as expected. The difference decreased

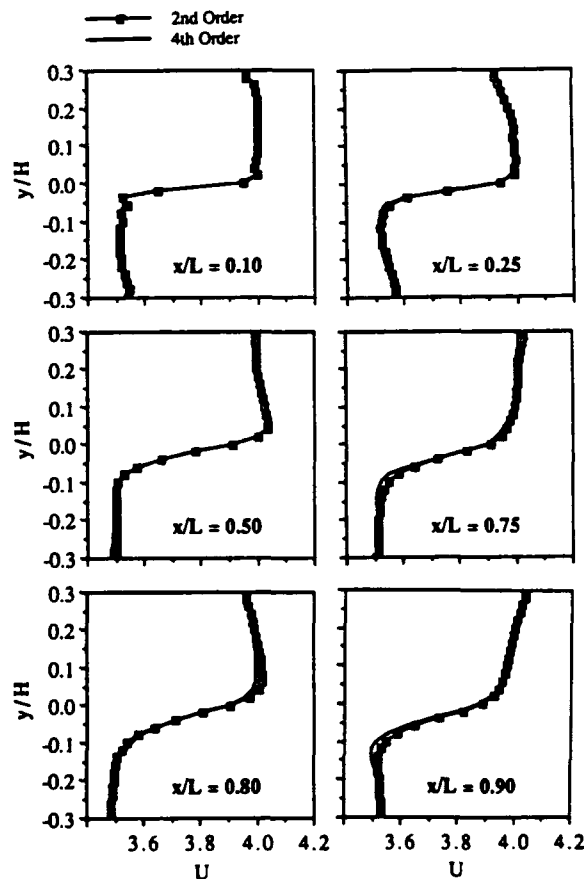


Fig. 11 Velocity profiles across the shear layer: comparison of second- and fourth-order MacCormack schemes for case 1 with 111×31 grid.

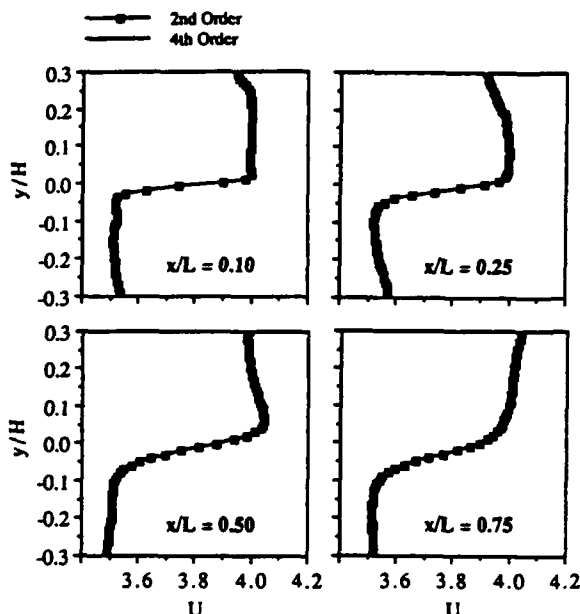


Fig. 12 Velocity profiles across the shear layer: comparison of second- and fourth-order MacCormack schemes for case 1 with 221×61 grid.

further downstream. It is concluded from these that the second-order scheme already shows reasonable accuracy, and that the fourth-order results are quite accurate.

The effect of grid size was checked by comparing the above results with those obtained with the 221×61 grid, as shown in Fig. 12. In this case, the difference between the second- and fourth-order codes is negligible for all stations. Thus, it is concluded that with the 221×61 grid, the results are not sensitive to grid size.

Computational Resources

All calculations reported here were performed on the Cray X-MP at the Pittsburgh Supercomputing Center. The CPU time per time step per grid node was $10 \mu\text{s}$ for the fourth-order MacCormack scheme, using the 221×61 grid.

Conclusions

A numerical study of the behavior of planar supersonic shear layers has been performed. Different numerical schemes have been tested. Techniques for enhancing the growth rate of the shear layer have been investigated. The following are noted from the results:

1) The fourth-order MacCormack scheme accurately simulates the evolution of the imposed disturbances. The results are essentially independent of the spatial order of the scheme, with a 221×61 grid with the grid parameters used.

2) A perturbation of 2% of the mean flow velocity, imposed at the upstream boundary in the normal direction, produces a larger growth of the shear layer than an equal amount of perturbation imposed in the streamwise or spanwise directions.

3) Imposed sinusoidal disturbances in the normal velocity upstream lead to the formation and growth of vortical structures. The shear layer thickness grows rapidly at first and then the growth rate decreases asymptotically.

4) The root-mean-square fluctuation level in the streamwise velocity and the shear layer growth rate decrease with increasing values of the theoretical convective Mach number of the shear layer.

5) The vortical structures are found to move at different Mach numbers relative to the upper and lower stream, and the relative Mach number appears to be smaller relative to the stream with the higher Mach number.

Acknowledgments

This work was supported by the Office of Naval Research under contract N00014-87-K-0132. S. G. Lekoudis was the Technical Monitor. Computer resources were provided by a grant from the Pittsburgh Supercomputing Center.

References

- ¹Chinzei, N., Masuya, G., Komuro, T., Murakami, A., and Kudou, K., "Spreading of Two-Dimensional Supersonic Mixing Layers," *Physics of Fluids*, Vol. 29, No. 5, May 1986 pp. 1345-1347.
- ²Papamoschou, D., "Experimental Investigation of Heterogeneous Compressible Shear Layers," Ph.D. Dissertation, California Institute of Technology, Pasadena, CA, 1986.
- ³Guirguis, R. H., "Mixing Enhancement in Supersonic Shear Layers: III. Effect of Convective Mach Number," AIAA Paper 88-0701, Jan. 1988.
- ⁴Drummond, J. P. and Mukunda, H. S., "A Numerical Study of Mixing Enhancement in Supersonic Reacting Flow Fields," AIAA Paper 88-3260, July 1988.
- ⁵Kumar, A., Bushnell, D. M., and Hussaini, M. Y., "A Mixing Augmentation Technique for Hypervelocity Scramjets," AIAA Paper 87-1882, July 1987.
- ⁶Ragab, S. A. and Wu, J. L., "Instabilities in the Free Shear Layer Formed by Two Supersonic Streams," AIAA Paper 88-0038, Jan. 1988.
- ⁷Ragab, S. A., "Instabilities in the Wake/Mixing Layer Region of a Splitter Plate Separating Two Supersonic Streams," *Proceedings of the 1st National Fluid Dynamic Congress*, Vol. 2, AIAA, Washington, DC, July 1988, pp. 1095-1102.
- ⁸Bayliss, A., Maestrello, L., Parikh, P., and Turkel, E., "Numerical Simulation of Boundary Layer Excitation by Surface Heating and Cooling," *AIAA Journal*, Vol. 24, July 1986, pp. 1095-1101.
- ⁹Papamoschou, D., Presentation at the Workshop on the Fluid Dynamics of Compressible Turbulent Shear Layers, Cincinnati, OH, July 1988.
- ¹⁰Sankar, L. N., Tang, W., and Komerath, N. M., "Numerical Simulation of Supersonic Free Shear Layers," *International Conference on Computational Engineering Science*, Atlanta, GA, April 1988.

Numerical Simulation of Three-Dimensional Supersonic Free Shear Layers

Ismail H. Tuncer* and Lakshmi N. Sankar†
Georgia Institute of Technology, Atlanta, Georgia 30332

Abstract

THE temporal stability and growth characteristics of three-dimensional supersonic shear layers are numerically investigated. An explicit time-marching scheme that is second-order accurate in time and fourth-order accurate in space is used to study this problem. The shear layer is excited by instability waves computed from a linear stability analysis and random initial disturbances. At low convective Mach numbers, organized vortical structures develop both for the random disturbance and the modal disturbance cases. At supersonic convective Mach numbers, vortical structures develop initially but are not sustained in time. Temporal growth of disturbances is found to be a strong function of the convective Mach number.

Contents

An improved understanding of factors that contribute to supersonic shear-layer growth is necessary for design of active and passive control techniques to enhance the mixing of airstreams and fuel streams, and for the design of efficient, compact SCRAMJET engines. It has been observed¹⁻³ that, in supersonic shear layers, organized vortical structures exist in a manner similar to subsonic shear layers. However, as the convective Mach number increases, the streamwise shear-layer growth rate is found to drop to about 30% of that of an incompressible flow.⁴

In the past, Tang et al.⁵ used a fourth-order MacCormack scheme to study temporal and spatial growth of two-dimensional thin shear layers at very early stages of laminar mixing, and studied the effects of convective Mach number as well as streamwise, spanwise, and cross-stream velocity disturbances on the shear layer growth. It was demonstrated that the growth rate of the shear layer decreased with increasing convective Mach number. In this work, three-dimensional, temporarily growing mixing layers have been studied. The study focuses on the effects of instability waves computed using a linear stability analysis and random initial disturbances on a temporarily evolving shear layer.

The three-dimensional, laminar, unsteady, compressible flow is governed by the Navier-Stokes equations, which may be formally written in a strong conservation form

$$q_t + F_x + G_y + H_z = R_x + S_y + T_z \quad (1)$$

where F , G , and H are inviscid flux terms, and R , S , and T are the viscous stress terms. Equation (1) was solved using an operator splitting approach and a MacCormack-type finite difference scheme:

$$q^{n+2} = L_x L_y L_z L_{xv} L_{yv} L_{zv} L_{xy} L_{yx} L_{yz} L_{zy} L_{xz} L_{zx} q^n \quad (2)$$

Presented as Paper 90-3958 at the AIAA 13th Aeroacoustics Conference, Tallahassee, FL, Oct. 22-24, 1990; received Jan. 22, 1991; synoptic received May 16, 1991; accepted for publication July 17, 1991. Full paper available from AIAA Library, 555 West 57th St., New York, NY 10019. Copyright © 1990 by the American Institute of Aeronautics and Astronautics, Inc. All rights reserved.

*Postdoctoral Fellow, School of Aerospace Engineering. Member AIAA.

†Associate Professor, School of Aerospace Engineering. Member AIAA.

The L_x , L_y , and L_z operators involve solutions of the one-dimensional equation such as

$$q_t + F_x = 0 \quad (3)$$

This one-dimensional equation is solved through the following predictor-corrector sequence, recommended by Bayliss and Maestrello.⁶

Predictor step:

$$q_i^n = q_i^{n-1} - \frac{Dt}{6 Dx} [7F_i - 8F_{i-1} + F_{i-2}]^{n-1} \quad (4)$$

Corrector step:

$$q_i^{n+1} = \frac{(q_i^n + q_i^{n-1})}{2} + \frac{Dt}{12 Dx} [7F_i - 8F_{i+1} + F_{i+2}]^n \quad (5)$$

The viscous operators L_{xv} , L_{yv} , and L_{zv} are integrated similarly with the exception that the viscous stress terms are differenced in space with the second-order-accurate central difference scheme. The overall numerical scheme is fourth-order accurate in space and second-order accurate in time as far as the inviscid part is concerned.

Since the temporal development mixing layers are studied, periodic boundary conditions in the streamwise and spanwise directions and slip boundary conditions in the cross-stream direction are applied.

The computational domain is a rectangular channel that extends in stream- and spanwise directions over one wavelength of the longest disturbance wave predicted by linear stability analysis for a given convective Mach number. In the cross-stream direction, it extends from -7.5 to 7.5 times the vorticity thickness. The computational domain is discretized with a $66 \times 34 \times 121$ uniformly spaced grid along the streamwise, spanwise, and cross-stream directions, respectively. The Reynolds number is based on the vorticity thickness and

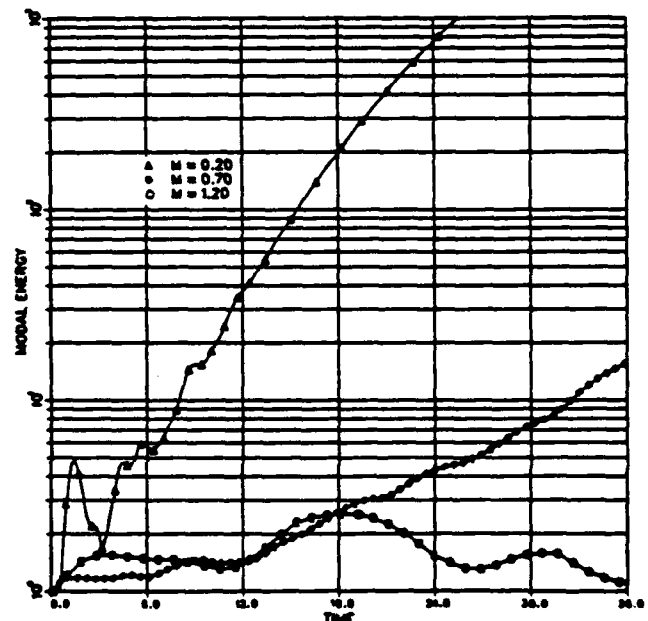


Fig. 1 Modal energy growth of the most unstable modes in shear layers disturbed by instability waves.

ranges between 3×10^2 and 6×10^2 . The mean velocity across the cross-stream direction is given by a hyperbolic tangent profile. The convective Mach number is defined as $M_c = (U_1 - U_2)/(c_1 + c_2)$, where U is the magnitude of the mean velocity, c is the speed of sound, and subscripts 1 and 2 refer to the upper and lower streams, respectively.

The modal kinetic energy content of the flowfield is defined as

$$E_{mn}(t) = \int [uu^* + vv^* + ww^*] dz \quad (6)$$

where u , v , and w are the two-dimensional Fourier transforms of the velocity field on the plane that spans in the streamwise and spanwise directions. The integration is in the cross-stream direction. The superscript * denotes the complex conjugate.

Instability Waves Superposed on Mean Flow

We have first superposed three-dimensional waves onto the mean flow and monitored temporal evolution of the flowfield and the modal energy growth. These disturbance waves are the most unstable waves predicted by the linear stability analysis³ at a given convective Mach number and are given for the

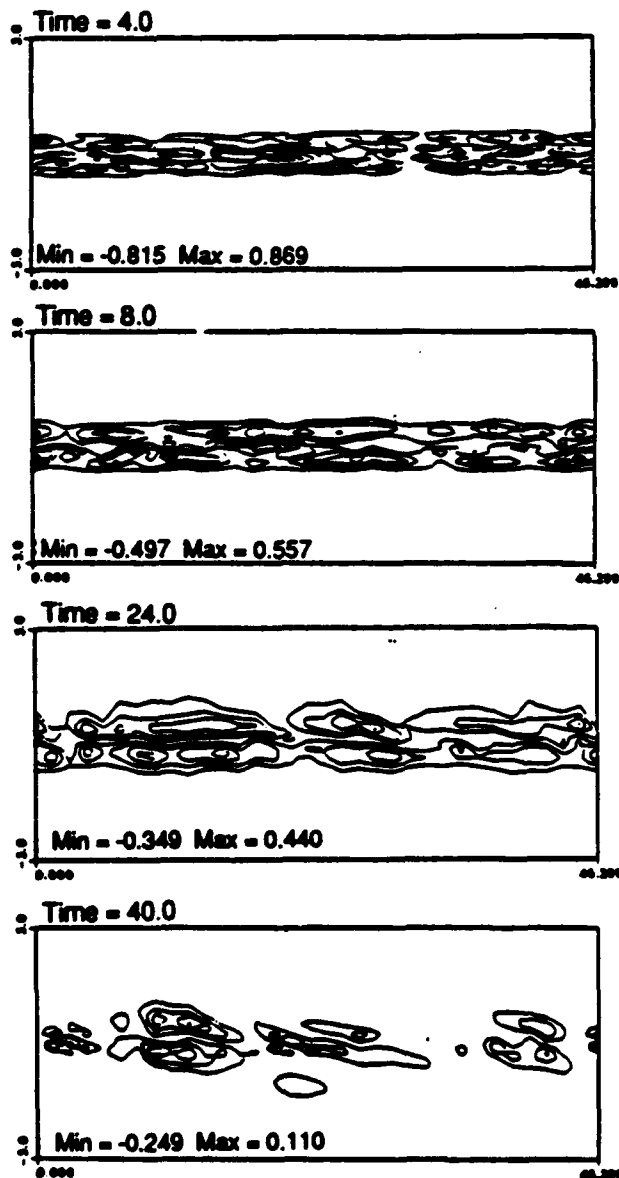


Fig. 2 Spanwise vorticity contours at midspan in a randomly disturbed shear layer, $M_c = 1.2$.

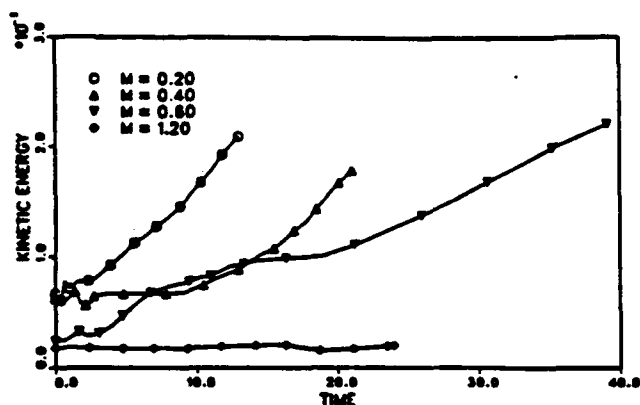


Fig. 3 Average perturbation kinetic energy growth in randomly disturbed shear layers.

velocity components, density, and temperature in the following form:

$$d(x, y, z) = AD(z) \exp i(\alpha x + \beta y) \quad (7)$$

where $D(z)$ is the eigenfunction, α and β are the wave numbers, and A is the magnitude, which is set to $0.015M_c$.

We have studied the flowfields for convective Mach numbers of 0.2, 0.7, and 1.2. The corresponding wavelengths of the most unstable waves, which are predicted by the linear stability analysis code, are $\alpha = 0.41$ and $\beta = 0$ for $M_c = 0.2$, $\alpha = 0.3$ and $\beta = 0.3$ for $M_c = 0.7$, and $\alpha = 0.14$ and $\beta = 0.07$ for $M_c = 1.2$. The temporal growth of modal kinetic energy associated with the most unstable modes is shown in Fig. 1.

Random Disturbances Superposed on Mean Flow

Next, we superposed a random initial disturbance field onto the mean flowfield. The random disturbance field was generated using a random number generator, and its magnitude at any point in the flowfield was restricted to be less than $0.03M_c$. These disturbances were confined to regions of significant vorticity in the shear layer, where $|u(y)| \leq 0.25M_c$. Computations were performed for convective Mach numbers of 0.2, 0.4, 0.6, and 1.2.

In all flow cases, random organized vortical structures were observed in the perturbation velocity field. However, at a higher convective Mach number of 1.2, organized structures tended to die out in time (Fig. 2). The temporal growth of average perturbation kinetic energy for the cases studied is given in Fig. 3.

The following is concluded:

- 1) The temporal growth rate in perturbation kinetic energy decreases with increasing convective Mach numbers for both modal and random disturbances.
- 2) At supersonic convective Mach numbers ($M_c = 1.2$), the growth of three-dimensional structures were also found to be unsustainable in both the random and modal disturbance cases.

References

- ¹Tam, C. K. W., and Hu, F. Q., "The Instability and Acoustic Wave Modes of Supersonic Mixing Layers Inside a Rectangular Channel," *Journal of Fluid Mechanics*, Vol. 203, 1989, pp. 51-76.
- ²Papamoschou, D., "Experimental Investigation of Heterogeneous Compressible Shear Layers," Ph.D. Dissertation, California Inst. of Technology, Pasadena, CA, Dec. 1986.
- ³Ragab, S., "Linear Instability Waves in Supersonic Turbulent Mixing Layers," AIAA Paper 87-1418, June 1987.
- ⁴Papamoschou, D., and Roshko, A., "Observations of Supersonic Free Shear Layers," AIAA Paper 86-0162, Jan. 1986.
- ⁵Tang, W., Komerath, N., and Sankar, L. N., "Numerical Simulations of the Growth of Instabilities in Supersonic Free Shear Layers," AIAA Paper 89-0376, 1989; also, *Journal of Propulsion and Power*, Vol. 6, No. 4, 1990, pp. 455-460.
- ⁶Bayliss, A., and Maestrello, L., "Simulation of Instabilities and Sound Radiation in a Jet," *AIAA Journal*, Vol. 9, No. 7, 1981, pp. 835-841.

AN ITERATIVE TIME MARCHING PROCEDURE FOR COMPUTATION OF
UNSTEADY VISCOUS FLOWS

L. N. Sankar, Professor

and

W. G. Park, Graduate Student

School of Aerospace Engineering
Georgia Institute of Technology, Atlanta, GA 30332

ABSTRACT

A technique for computing 2-D and 3-D unsteady, incompressible viscous flows is described. This procedure allows fourth or sixth order accuracy in space, and second order accuracy in time, and is general enough to be used to study external and internal flow problems. Algorithmic details of the procedure are described. A sample application of this algorithm to 3-D steady viscous flow over a body of revolution is given. The final paper will give additional numerical results for external flow past a body of revolution at an angle of attack, and flow over 2-D airfoil geometries.

INTRODUCTION

The problem of accurately computing unsteady three dimensional incompressible flows is one of great interest to researchers working in the fields of bioengineering and aerospace industry. The flow within bifurcated channels, flow in blood vessels with compliant walls, flow over complex submarine shapes, flow past underwater propellers, and flows within turbomachinery, ducts and pumps are all inherently three-dimensional, and unsteady. These configurations can not be properly analyzed unless a computational capability that complements experimental methods exists to analyze such flows.

Techniques for efficient and accurate prediction of 3-D, incompressible, unsteady flows are also necessary for the first principle based prediction of incompressible turbulent flows through direct numerical simulations or large eddy simulations. The lack of such tools is one of the principal reasons that first principle based prediction of turbulent flows past and through complex configurations have not been extensively attempted to date.

Finally, there has been a significant interest within the research community during the past several years in the use of active and passive control techniques to improve flow quality and reduce undesirable phenomena. There is considerable interest in the use of control devices to promote mixing in air/fuel streams, or hot/cold streams, to ensure uniform inflow at the compressor face, and to prevent flow separation within diffusers, and highly curved ducts. There is also interest in the use of control devices to reduce noise, vibration, and flutter. These control devices and

control laws can not be perfected until a capability for accurate and efficient prediction of unsteady incompressible flows is available.

A SURVEY OF EXISTING SOLUTION PROCEDURES

Interest in the development of numerical solution procedures for the prediction of two- and three-dimensional unsteady Navier-Stokes equations arose in the mid sixties and early seventies with the availability of high speed digital computers of the IBM 370 and the CDC 6600 class. During the past two decades, evolution of these techniques has been fueled by the availability of faster and cheaper scalar/vector computer architectures, the availability of efficient solution algorithms, and the development of automated grid generation techniques capable of dividing complex flow regions into smoothly varying cells. At the present time, this field of computational fluid dynamics is a well developed science, documented in text books [Ref. 1-3], conference proceedings and journals.

Although solution techniques for both compressible and incompressible flows have evolved, techniques for analyzing these two class of flows are necessarily different. Compressible viscous flows are governed by a set of parabolic partial differential equations. As first pointed out by Crocco [Ref. 4] marching in time from an arbitrary set of initial conditions is indeed the most efficient way of solving unsteady compressible viscous flows. Incompressible viscous flows on the other hand are governed by a mixed set of elliptic and parabolic differential equations, making noniterative time marching approaches difficult, except in special cases.

Despite the different mathematical characteristics of compressible and incompressible flows, enough commonalities exist between these two class of flows to encourage adaptation of algorithms developed for incompressible flows to compressible flows and vice versa. For example, the parabolic part of the incompressible flow equations (e.g. the vorticity transport equation) may be integrated using schemes such as the McCormack scheme, or implicit approximate factorization schemes which are the traditional tools used in compressible flow solvers. Grid generation schemes, and graphics pre- and post-processing tools are all quite similar, whether one solves the compressible flow equations or the incompressible flow

equations. Nonetheless, compressible flow solvers have evolved to a point where they may be routinely used to study a variety of problems ranging from 1-D subsonic flow to 3-D unsteady, hypersonic flow. Incompressible flow solvers, on the other hand, have shown only a limited level of success in predicting 3-D unsteady viscous flows. All evidence to date points the elliptic portion of the incompressible flow equations to be one of the difficulties. The traditional, iterative solution of the elliptic portion of the governing equations (where the unknown may be pressure, or the scalar components of a vector stream function) converges very slowly, and the convergence rate usually deteriorates at high Reynolds numbers.

One of the commonly used approaches for solving 2-D incompressible flows is the vorticity-velocity or the vorticity-stream function formulation. Mehta [Ref. 5], Wu [Ref. 6], Thames [Ref. 7] and others have used this approach. In Mehta's work, unsteady viscous flow past stationary and oscillating airfoils were studied. He used an approximate factorization scheme to integrate the parabolic portion of the governing equations, and a direct fast Poisson solver to invert the elliptic equation for the stream function. He experienced difficulties in obtaining accurate solutions at Reynolds numbers as low as 5,000. Some researchers (e.g. Wu) have circumvented the need to iteratively solve the Poisson equation for velocity or stream function, by recasting the differential equation as an integral relation. The operations count for this approach dramatically increases with Reynolds number. This approach requires costly, numerical evaluation of volume integrals in three-dimensions. Thompson [Ref. 8] studied the 3-D jet-in-cross wind problem. As in the previous cases, the analyses were restricted to relatively low Reynolds numbers.

A different approach for solving the incompressible Navier-Stokes equations is to solve them in the primitive variables form (pressure-velocity). Again, a variety of approaches for solving these equations are possible. In some studies [e.g. Goda, Ref. 9], the u-, v- and w- momentum equations are integrated in time using an implicit or an explicit time marching scheme. The pressure field which appears in these equations is evaluated at each time step by solving a Poisson's equation for pressure, usually using an iterative scheme. By using a staggered storage scheme where the pressure field is stored at cell centers, while the velocity fields are stored at face centers, it is possible to avoid use of nonphysical, extraneous boundary conditions for pressure at the solid surface. Brandt [Ref. 10], Ta'asan [Ref. 11] have shown that it is possible to accelerate the iterative solution of the pressure field using classical multigrid techniques.

An alternative to solving a Poisson equation for pressure is the Marker and Cell (MAC) algorithm developed at Los Alamos by Welch et. al. [Ref. 12]. At each time step, the velocity field is first updated using an explicit time marching scheme, using the pressure field from the previous time step. Next, the correction to the pressure at the center of each cell is evaluated by summing up the mass flux through the six faces of the cell. If a cell is accumulating mass, then the pressure value is increased to repel fluid away from the cell. If a cell is losing mass, then the pressure value is lowered. Any change in the pressure field produces a corresponding change in the velocity field, which may be computed simply by evaluating the changes in the pressure gradient. Thus the velocity field is iteratively updated along with the pressure field at each time step. Hirt and Cook [Ref. 13] have extended the MAC method to 3-D flows, and to curvilinear coordinates.

Building upon the earlier works by Chorin [Ref. 14] and Steger and Kutler [Ref. 15], Kwak et. al. [Ref. 16] have developed an implicit time marching scheme for solving incompressible flows. In their scheme, known as the method of pseudo-compressibility, an artificial pressure derivative with respect to time is appended to the continuity equation. The entire system of equations is solved by a time marching scheme, as in a compressible flow. If only a steady state is of interest, then the added

pressure derivative drops out in the steady state, and physically correct solutions are achieved. If the aim is to achieve time-accurate calculations, either the artificial pressure derivative should be kept very small (which makes the equations extremely stiff, and forces very small time steps) or an inner iterative loop within each time step should be used.

A number of other approaches for solving incompressible viscous flows exist, and have been demonstrated to work well for a limited number of test cases. A direct inversion of the Poisson equation for pressure at each time step was employed by Osswald and Ghia [Ref. 17]. This requires large amounts memory, because the sparse coefficient matrix, that arises when the Elliptic equation for pressure is discretized, gives rise to a full matrix when inverted. Thus, even a very sparse grid containing 1,000 nodes will require one million words of storage to store the inverted matrix. Furthermore, a direct solution to the elliptic equation alone does not necessarily guarantee stable, accurate solutions of the entire equation set. Hafez et al. [Ref. 18] have looked at the decomposition of the velocity field into a rotational part and an irrotational part. This approach shares many of the drawbacks of the traditional velocity-vorticity form previously discussed. Higher order projection methods for solving incompressible viscous flows have been documented by Bell et. al. [Ref. 19] and have been applied to low Reynolds number flows ($Re < 5000$).

The methods for solving incompressible viscous flows discussed above have several drawbacks:

- a) Most of them are only second order accurate in space, and first or second order accurate in time. Before these schemes can be applied to phenomena such as direct numerical simulation of turbulence, it will be necessary to raise the spatial and temporal accuracy to fourth or higher order.
- b) The iterative convergence of the elliptic portion of the solvers deteriorates at high Reynolds numbers.
- c) In some instances (e.g. method of pseudo-compressibility) a trade off exists between temporal accuracy and convergence speed.
- d) These methods do not take advantage of the vast progress that has been achieved in the solution of steady viscous flows. For example, with rare exceptions, multigrid acceleration of the Poisson solvers has not been attempted. Acceleration of the iterative solution of the pressure field to convergence using spatially varying time steps and grid sequencing have also not been extensively used. Although these techniques are primarily intended for steady state solutions in compressible flows, there is no reason why these strategies can not be used to solve the elliptic partial differential equation governing the pressure (or a vector stream function).
- e) There has been a growing interest in the use of massively parallel computer architectures such as the Connection Machine to solve unsteady viscous flows. Many of the compressible flow algorithms have already been adapted for use on these machines [Ref. 20-22]. There is a need to develop new procedures and modify existing algorithms for incompressible flows, on parallel machines.

MATHEMATICAL AND NUMERICAL FORMULATION

The objective of the present research is to develop efficient, and accurate solution techniques for the analysis of 3-D, unsteady, incompressible flows. The algorithms to be described meet the following requirements:

- a) The schemes should be fourth or higher order accurate in space, and second or higher order accurate in time.
- b) The solution techniques should be capable of handling

complex internal and external flows. That is, the equations and the solution procedures should be cast in a curvilinear, time-deforming coordinate system.

c) The solution procedures should work for a wide range of Reynolds numbers, with no appreciable loss in solution efficiency.

d) The solution procedures should be tailored for efficient execution on the current generation of vector and massively parallel computer architectures.

With the above goals in mind, a solution procedure for solving 3-D unsteady incompressible flows has been developed. The key features of the present scheme are listed below.

a) The primitive variables (p,u,v,w) are the primary unknowns in the present formulation. Depending on the turbulence models to be used, additional unknowns such as the turbulence kinetic energy k, dissipation rate e, the Reynolds stress components u'v' may need to be evaluated. In three-dimensional flows, it is believed that solving for the primitive variables (p,u,v,w) will be more convenient than use of vorticity-vector stream function.

b) The present scheme is iterative in nature. That is, at each time step, the flow properties are updated in an iterative fashion. Such an iterative procedure is necessary, because one of the unknowns, namely the pressure is governed by an elliptic PDE. In some approaches, such as the pseudo-compressibility approach, a noniterative marching scheme has been used. However, such schemes trade temporal accuracy for the ability to achieve a convergent steady state solution.

c) The parabolic portion of the governing equations employ a high order (second or fourth order in time) implicit time marching scheme. Since there is at least one flow variable (pressure) that must be iteratively solved for, there is no reason not to update the rest of the flow variables (u,v,w) during each pressure iteration. The use of implicit schemes removes the necessity to choose small time steps required by stability considerations.

Present Scheme:

For the sake of convenience, the details of the present scheme are described in a Cartesian coordinate system, and for 2-D flows. Since the governing equations may be cast in a curvilinear, non-orthogonal, time-deforming coordinate system in a form very similar to the Cartesian form, application of the present algorithm on a curvilinear grid is straightforward.

The goal of the present scheme is to advance the flow properties (p,u,v) from a known time step 'n' to the next time step 'n+1'. Let 'k' be an iteration counter. Then a quantity such as $u^{n+1,k}$ denotes the variable u at the time level 'n+1' and iteration level 'k'. A good starting guess for the flow variables at time level 'n+1' at the start of the iteration process is these variables at the previous time level. That is,

$$\begin{aligned} u^{n+1,0} &= u^n \\ v^{n+1,0} &= v^n \\ p^{n+1,0} &= p^n \end{aligned}$$

We also define 'delta quantities' Δu , Δv and Δp such that

$$\Delta u = u^{n+1,k} - u^{n+1,k-1}$$

$$\Delta v = v^{n+1,k} - v^{n+1,k-1}$$

$$\Delta p = p^{n+1,k} - p^{n+1,k-1}$$

Thus, the goal of the iterative process at each time step is to drive these delta quantities Δu , Δv and Δp to zero.

An coupled system of equations for these delta variables may now be written. For example, consider the u-momentum equation (with density assumed to be unity):

$$u_t + (u^2)_x + (uv)_y + \partial p / \partial x = \nu (u_{xx} + u_{yy})$$

For the sake of illustration, let us assume that a second order accuracy in time is acceptable. Then, the time derivative $\partial u / \partial t$ will be approximated as

$$\partial u / \partial t = (u^{n+1,k} - u^n) / \Delta t$$

The other terms in the above equation will be evaluated at the 'n+1/2' time level:

$$u^{n+1/2,k} = (u^{n+1,k} + u^n) / 2$$

$$u^{n+1/2,k-1} = (u^{n+1,k-1} + u^n) / 2$$

The spatial discretizations may be carried out using either a second order accurate central/upwind difference form or a higher order form. The higher order spatial accuracy may be achieved on uniform grids using Pade' approximations to the derivatives; on highly stretched grids, higher order accuracy may be achieved using a Lagrangean fit to the variables u^2 , uv , p etc. In high Reynolds number flows, the Lagrangean fit need not be equally weighted about the node, but may be biased in the direction of the flow. For example, when the flow is from left to right, if the Lagrangean interpolation of u^2 is done using nodes only to the left of, and including, the current node then an upwind formulation results. The details of how the spatial discretization is done do not change the iterative solution process being described.

If the quantities such as u^2 , uv and p appearing in the above discretization are linearized about known information u^n and $u^{n+1,k-1}$, then a difference equation linking Δu , Δv and Δp results. Such an equation is given for the u-momentum equation below:

$$\Delta u / \Delta t + \{ \delta_x (2u^{n+1/2,k-1} \Delta u) + \delta_y (u^{n+1/2,k-1} \Delta v + v^{n+1/2,k-1} \Delta u) + \delta_x (\Delta p) \} / 2$$

$$= -\nu / 2 (\delta_{xx} + \delta_{yy}) \Delta u = - \{ (u^{n+1,k-1} - u^n) / \Delta t + \{ \delta_x (u^2) + \delta_y (uv) + \delta_{xx} p - \nu (\delta_{xx} u + \delta_{yy} u) \}^{n+1/2,k-1} \}$$

Here δ_x , δ_y , δ_{xx} etc. stand for suitable, high order upwind or central approximations to the spatial derivatives.

Note that the right side of the above equation is simply the Crank-Nicholson approximation to the u-momentum equation. If the right side is driven to zero, then the unsteady u-momentum equation will be fully satisfied at the current time level n+1.

A similar equation may be written for the v-momentum equation, linking the quantities Δu , Δv and Δp . In the case of continuity equation, one can draw upon the Marker and Cell approach, to link the iterative changes in pressure to changes in velocity, and write

$$\beta \Delta p = - (\delta_x u + \delta_y v)^{n+1,k-1}$$

Here β is a free parameter, that may even vary from node to node.

It should be noted that the addition of $\beta \Delta p$ to the left side of the above equation is not equivalent to a pseudo-compressibility approach. As long as Δp is driven to zero, the discretized form of the continuity equation is exactly satisfied at each time step.

Applying the above discretizations in time and space at all

the nodes in the flow field, a system of simultaneous equations results for the quantity Δq equal to $(\Delta u, \Delta v, \Delta p)$. This system may be formally written as:

$$[A] \{\Delta q\} = \{R\}$$

Here, the right hand side is the governing equation, with the temporal and spatial derivative approximated as discussed above. The right side also contains the time derivatives that appear in the governing equation. In traditional iterative schemes such as the pseudocompressibility scheme, the right side contains only the spatial derivatives. Thus, in these schemes, only the steady state solution is guaranteed. In the present approach, the time accurate solution at each time step is guaranteed, if the right side can be driven to zero.

PRELIMINARY RESULTS

The above procedure for solving 2-D and 3-D incompressible viscous flows is being tested on several 2-D problems. A preliminary version of the procedure for computing external flows over three-dimensional geometries also exists. Figure 1 shows the computed surface pressure distribution over a body of revolution tested in Germany, for which experimentally measured data is available. It is clear that the proposed iterative scheme gives numerical results that are in good agreement with experiments.

The full paper will give the following additional results:

- a) Incompressible flow past an airfoil at Reynolds numbers 5000 to 3.5 Million.
- b) Steady 3-D separated flow past an ellipsoid of revolution at an angle of attack.

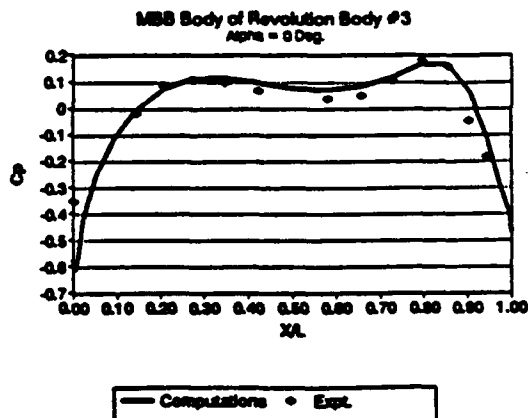
These cases have been chosen because of the availability of good quality experimental data, and the simplicity of the grid generation.

REFERENCES

1. Roache, P. J., *Computational Fluid Dynamics*, Hermosa Publishers, Albuquerque, NM, 1972.
2. Peyret, R. and Taylor, T. D., *Computational Methods for Fluid Flow*, Springer Verlag, 1983.
3. Hirsch, C., *Numerical Computation of Internal and External Flows, Vol. 1*, John Wiley & Sons Ltd., 1988.
4. Crocco, L., "A Suggestion for the Numerical Solution of the Steady Navier-Stokes Equations," *AIAA Journal*, Vol. 3, No. 10, 1965, pp1824-1832.
5. Mehta, U. B., "Dynamic Stall of an Oscillating Airfoil," *AGARD CP-227*, 1977.
6. Wu, J. C., "Numerical Boundary Conditions for Viscous Flow Problems," *AIAA Journal*, Vol. 14, No. 8, August 1976, pp1042-1049.
7. Thames, F. C., "Numerical Solution of Incompressible Navier-Stokes Equations About Arbitrary Two-Dimensional Bodies," Ph. D. Thesis, Mississippi State University, Mississippi, August 1977.
8. Thompson, J., Ph. D. Dissertation, Georgia Institute of Technology, 1972.
9. Goda, K., "A Multistep Implicit Technique with Implicit Difference Schemes for Calculating Two- or Three-Dimensional Cavity Flows," *Journal of Computational Physics*, Vol. 30, 1979.
10. Brandt, A., "Multigrid Techniques: Guide with Applications to Fluid Dynamics, GMD-Study No. 85, GMD-FIT, 1984.
11. Ta'asan, S., "Multigrid Method for a Vortex Breakdown

Simulation," *ICASE Report No. 86-18*, pp264-290, 1986.

12. Welch, J.E., Harlow, F.H., Shanon, J.P. and Daly, B.J., "The MAC Method: A Computing Technique For Solving Transonic Viscous, Incompressible, Transient Fluid-Flow problems Involving Free Surfaces", *Los Alamos Report LA-3425*, November, 1965.
13. Hirt, C.W. and Cook, J.L., "Calculating Three-Dimensional Flows Around Structures and Over Rough Terrain", *J. of Computational Physics*, Vol. 10, 1972, pp. 324-340.
14. Chorin, A.J., "A Numerical Method for Solving Incompressible Viscous Flow Problems", *Journal of Computational Physics*, Vol. 2, 1967, pp. 12-26.
15. Steger, J.L. and Kutler, P., "Implicit Finite-Difference Procedures for the Computation of Vortex Wakes", *AIAA Journal*, Vol. 15, Apr. 1977, pp. 581-590.
16. Kwak, D., Chang, J.L.C., Shanks, S.P. and Chakravarthy, S.R., "A Three-Dimensional Incompressible Navier-Stokes Flow Solver Using Primitive Variables", *AIAA Journal*, Vol. 24, Mar. 1986, pp.390-396.
17. Oswald, G.A., Ghia, K.N. and Ghia, U., "An implicit Time-Marching Method for Studying Unsteady Flow with Massive Separation", *AIAA CP 854*, 1985, pp. 686-696.
18. Hafez, M. and Soliman, M., "A velocity Decomposition Method for Viscous Incompressible Flow Calculations, Part II.", *AIAA 9th Computational Fluid Dynamics Conference*, Buffalo, N.Y. Jun. 1989.
19. Bell, J.B., Solomon, J.M. and Szymczak, W.G., "A Second-Order Projection Method for the Incompressible Navier-Stokes Equations on Quadrilateral Grids", *AIAA 9th Computational Fluid Dynamics Conference*, Buffalo, N.Y. Jun. 1989.
20. Jespersen, D.C. and Levit C., "A Computational Fluid Dynamics Algorithm on a Massively Parallel Computer", *AIAA 9th Computational Fluid Dynamics Conference*, Buffalo, N.Y. Jun. 1989.
21. Wake, B.E. and Egolf, T.A., "Implementation of a Rotary-Wing Three-Dimensional Navier-Stokes Solver on a Massively Parallel Computer", *AIAA 9th Computational Fluid Dynamics Conference*, Buffalo, N.Y. Jun. 1989.
22. Landsberg, A.M. and Murman, E.M., "Implementation of a 2D-Euler Solver Using Id World, a Parallel Programming Environment", *AIAA 9th Computational Fluid Dynamics Conference*, Buffalo, N.Y. Jun. 1989.



**A THREE-DIMENSIONAL MULTIGRID TECHNIQUE
FOR UNSTEADY INCOMPRESSIBLE VISCOUS FLOWS**

A Condensed Version of the Thesis

Presented to

The Faculty of the Division of Graduate Studies

By

Warn-Gyu Park

In Partial Fulfillment

of the Requirements for the Degree

Doctor of Philosophy

in the School of Aerospace Engineering

Georgia Institute of Technology

March 1993

LIST OF CONTENTS

I	INTRODUCTION	1
II	MATHEMATICAL FORMULATION	6
	2.1 Governing Equations in the Physical Domain	6
	2.2 Governing Equations in the Computational Domain	7
III	NUMERICAL FORMULATION	10
	3.1 Grid Generation	10
	3.2 Grid Motion	10
	3.3 Iterative Time Marching Procedure	11
	3.4 Initial and Boundary Conditions	15
	3.5 Acceleration by Multigrid Technique	18
IV	RESULTS AND DISCUSSION	20
	4.1 Dynamic Stall of an Oscillating Airfoil	20
	4.2 3-D Steady Flow over an Ellipsoid of Revolution	21
	4.3 3-D Steady Flow through a 90° Bended Square Duct	22
	4.4 Acceleration of 2-D Flow by Multigrid Technique	23
	4.5 3-D Steady Flow around a marine Propeller	24
V	CONCLUDING REMARKS	26
	FIGURES	
	REFERENCES	

CHAPTER I

INTRODUCTION

The accurate computation of three-dimensional unsteady incompressible flow problem is one of great interest to researchers working in fields of aerodynamics, hydrodynamics and biofluid mechanics. The flow over complex submarine shapes, flow past underwater propeller, flow within turbomachinery, and flow in blood vessels with compliant walls are examples of such flows. Accurate and efficient computation of such flows at high Reynolds numbers is presently not possible due to the mixed (elliptic-parabolic) nature of the governing equations. Indeed, methods for three-dimensional incompressible flows lag behind three-dimensional compressible flows by several years. Until accurate and efficient methods for three-dimensional incompressible, unsteady flows become available, it will not be possible to attempt challenging problems such as the first principles based on direct simulation or large eddy simulation of turbulent flows over complex geometries. The lack of such tools is one of the principal reasons that the first principles based prediction of turbulent flows past and through complex configurations has not been extensively attempted to date.

As Gresho and Sani (ref.1) pointed out, the pressure is a somewhat mysterious quantity in incompressible flows. It is not a thermodynamic variable since there is no 'equation of state' for an incompressible fluid. It is in one sense a mathematical artefact - a Lagrange multiplier that constrains the velocity field to remain divergence-free ; i.e. incompressible - yet its gradient is a relevant physical quantity ; a force per unit volume. It propagates at infinite speed in order to keep the flow always and everywhere incompressible ; i.e. it is always in equilibrium with a time-varying divergence-free velocity field.

One might have the idea that the compressible Navier-Stokes equation solvers can compute incompressible flows using compressible flow methods, and setting the Mach

number to be very low. But this idea becomes impractical at very low Mach numbers because the compressible Navier-Stokes equation solvers have a singular behavior as the Mach number approaches zero. This leads to an ill-conditioned stiff system of equations and consequently very slow convergence, or even divergence of the solution with time. This stiffness can be explained as a time step limitation (ref.2). We note that all explicit methods for solving the compressible Navier-Stokes equations are limited to a time step which is less than that given by the CFL condition. For example, in two-dimensions :

$$\Delta t \leq \frac{1}{(|u|/\Delta x) + (|v|/\Delta y) + a \left[(1/\Delta x)^2 + (1/\Delta y)^2 \right]^{1/2}} \quad (1.1)$$

where a is the speed of sound. From this condition, we observe that Δt approaches zero as the speed of sound approaches infinity. As a result, an "infinite" amount of computer time would be required to compute a truly incompressible flow in this manner. Implicit methods will permit a larger Δt , but the maximum value is normally less than 100 times that given by Eq.(1.1) because of truncation errors, approximate factorization errors, and so on. Thus, even if an implicit scheme is used, it is not practical to compute a truly incompressible Navier-Stokes solution using compressible flow methods.

The significant difficulty in solving incompressible Navier-Stokes equations is that the governing equations are a mixed elliptic-parabolic type of partial differential equations. The continuity equation does not have a time derivative term and is given in the form of a divergence-free constraint. This is another major difference between the incompressible and compressible Navier-Stokes equations. The absence of a time derivative term in the continuity equation prohibits time integration of continuity equation by a time marching scheme. The compressible Navier-Stokes equations, on the other hand, are efficiently integrated by time marching schemes because they are a set of parabolic partial differential equations.

One of the commonly used approaches for solving two-dimensional incompressible flow is the vorticity-velocity or vorticity-stream function formulation (ref. 3,4,5). This is very efficient for two-dimensional problems, but this approach can not be extended straightforwardly to three dimensions. Consequently, the incompressible Navier-Stokes equations for three-dimensional problem are normally solved in their primitive variable form (p,u,v,w). Most methods using primitive variables may be classified into three groups. The first approach is the pressure Poisson method or Marker-and-Cell (MAC)

method which was first introduced by Harlow and Welch (ref.6). In the pressure Poisson method, the velocity field is advanced in time by solving the momentum equations with a stable explicit or implicit time marching scheme. Then the pressure field is evaluated at each time step by solving a Poisson equation for pressure directly (ref.7) or iteratively (ref.8,9,10). The continuity equation is thus satisfied when the pressure field is computed implicitly. This Poisson equation for pressure is obtained by taking the divergence of the unsteady momentum equations. The main idea of the MAC method (ref.11,12), an alternative to solving a pressure Poisson equation, is that the pressure field is updated at each time step by adjusting the pressure by an amount proportional to the negative of the velocity divergence :

$$p_{i,j}^k - p_{i,j}^{k-1} = -\beta (\nabla \cdot \bar{V})^{k-1} \quad (1.2)$$

Here the superscripts 'k' and 'k-1' denote the iteration level, and β is a relaxation factor. Usually, a staggered grid system (ref.6) is used for the MAC method, because such a grid does not require the specification of pressure on the boundaries and does not produce unphysical oscillations in the pressure and velocity fields due to the central differencing of the pressure gradient term. The second approach is a projection method (or, fractional step method) which was first introduced by Chorin (ref.13). At the first step, an intermediate velocity is computed from the momentum equation without the pressure gradient term. Then a pressure field is computed which will make the velocity field obtained from the first fractional step divergence free. Finally, a second fractional step is performed using the pressure field just computed. The third group is the pseudocompressibility method (ref.14,15) which was also first introduced by Chorin (ref.16) primarily for obtaining steady state solutions. In this method, an artificial pressure derivative with respect to time is appended to the continuity equation. The entire system of equation is solved by a time marching scheme developed for compressible flows, such as the approximate factorization scheme (ref.17). If only a steady state is of interest, then the added pressure derivative drops out in the steady state, and physically correct solutions are achieved. If the aim is to achieve time-accurate calculations, either the artificial pressure derivative should be kept very small (which makes the equations extremely stiff, and forces very small time steps) or an inner iterative loop within each time step should be used (ref.18,19). A concept similar to the pseudocompressibility method, known as the penalty function method (ref.20) is widely used in the finite-element based incompressible flow solvers, which solves for p to satisfy :

$$\lambda p + \nabla \cdot \bar{V} = 0 \quad (1.3)$$

In this method, the pressure gradient term of momentum equation is eliminated by substituting Eq.(1.3) into the momentum equation, and then solving the momentum equations with $\lambda \rightarrow 0$.

The methods for solving incompressible viscous flow discussed above have several drawbacks :

- a) Most of them are only second order accurate in space, and first or second order accurate in time. Before these schemes can be applied to phenomena such as direct numerical simulation of turbulence, it will be necessary to raise the spatial and temporal accuracy to fourth or higher order.
- b) The iterative convergence of the pressure Poisson solvers deteriorates at high Reynolds numbers.
- c) In some instance (e.g. in the pseudocompressibility method), a trade off exists between temporal accuracy and convergence speed.
- d) These methods do not take advantage of the vast progress that has been achieved in the solution of steady, viscous flows. For example, with rare exceptions, multigrid acceleration of Poisson solvers has not been attempted. Acceleration of the iterative solution of the pressure field to convergence using spatially varying time steps and grid sequencing have also not been extensively used.
- e) There has been a growing interest in the use of massively parallel computer architectures such as the Connection Machine to solve unsteady viscous flows. Many of the compressible flow algorithms have already been adapted for use on these machines. There is a need to develop new procedures and modify existing algorithms for incompressible flows, on parallel machines.

The objective of this study is to develop an efficient and accurate solution technique for the analysis of two- and three-dimensional, unsteady, incompressible, viscous flows. The key features of the present scheme are listed below :

- a) The primitive variables (p,u,v,w) are the primary unknowns in the present formulation.
- b) The equations and the solution procedures are cast into a curvilinear, time-deforming coordinate system to handle complex internal and external flows.
- c) An iterative time-marching scheme is used.
- d) The present scheme is semi-implicit at each iteration and is suitable for efficient execution on the current generation of vector or massively parallel computer architectures.

e) The solution procedure works for a wide range of Reynolds numbers, with no appreciable loss in solution efficiency.

f) The present scheme is first order accurate in time and second order accurate in space, but higher order accuracy in space and time is easily achievable.

Only laminar flow is considered in the results to be discussed because the goal of this study is to develop an efficient and accurate incompressible Navier-Stokes solver. This method is however capable of handling turbulent flows provided a suitable turbulence model is used, and there are no inherent limitations in this method that will restrict it to laminar flows.

CHAPTER II

MATHEMATICAL FORMULATION

In this chapter, the governing equation for three-dimensional, unsteady, incompressible, viscous flow are presented in terms of the primitive variables (p, u, v, w) in both the Cartesian coordinate system and a curvilinear non-orthogonal, time deforming coordinate system.

2.1 Governing Equations in the Physical Domain

The motion of an incompressible viscous flow is governed by the conservation of mass and momentum, so called the continuity equation and the Navier-Stokes equation. Three-dimensional unsteady, incompressible, laminar, Navier-Stokes equations in an inertial Cartesian coordinate system may be written in a non-dimensional form as follows :

$$\frac{\partial q}{\partial t} + \frac{\partial}{\partial y}(E - E_v) + \frac{\partial}{\partial y}(F - F_v) + \frac{\partial}{\partial z}(G - G_v) = 0 \quad (2.1)$$

where

$$q = \begin{bmatrix} 0 \\ u \\ v \\ w \end{bmatrix} ; \quad E = \begin{bmatrix} u \\ u^2 + p \\ uv \\ uw \end{bmatrix} ; \quad F = \begin{bmatrix} v \\ uv \\ v^2 + p \\ vw \end{bmatrix} ; \quad G = \begin{bmatrix} w \\ uw \\ vw \\ w^2 + p \end{bmatrix} \quad (2.2)$$

$$E_v = \frac{1}{Re} \begin{bmatrix} 0 \\ \tau_{xx} \\ \tau_{xy} \\ \tau_{xz} \end{bmatrix} ; \quad F_v = \frac{1}{Re} \begin{bmatrix} 0 \\ \tau_{yx} \\ \tau_{yy} \\ \tau_{yz} \end{bmatrix} ; \quad G_v = \frac{1}{Re} \begin{bmatrix} 0 \\ \tau_{zx} \\ \tau_{zy} \\ \tau_{zz} \end{bmatrix}$$

The stress terms are given by

$$\begin{aligned}
\tau_{xx} &= \frac{2}{3} \left(2 \frac{\partial u}{\partial x} - \frac{\partial v}{\partial y} - \frac{\partial w}{\partial z} \right) \\
\tau_{yy} &= \frac{2}{3} \left(2 \frac{\partial v}{\partial y} - \frac{\partial u}{\partial x} - \frac{\partial w}{\partial z} \right) \\
\tau_{zz} &= \frac{2}{3} \left(2 \frac{\partial w}{\partial z} - \frac{\partial u}{\partial x} - \frac{\partial v}{\partial y} \right) \\
\tau_{xy} = \tau_{yx} &= \frac{\partial u}{\partial y} + \frac{\partial v}{\partial x} \\
\tau_{xz} = \tau_{zx} &= \frac{\partial w}{\partial x} + \frac{\partial u}{\partial z} \\
\tau_{yz} = \tau_{zy} &= \frac{\partial v}{\partial z} + \frac{\partial w}{\partial y}
\end{aligned} \tag{2.3}$$

In Eq.(2.2) and Eq.(2.3), u , v and w are the normalized Cartesian components of velocity, p is the normalized pressure, and Re is the Reynolds number defined as :

$$Re = \frac{\rho V_{\infty} L}{\mu} \tag{2.4}$$

where ρ , V_{∞} , L and μ are fluid density, freestream velocity, reference length and coefficient of viscosity (dynamic viscosity), respectively.

The governing equation (2.1) is a mixed set of elliptic-parabolic partial differential equations. As mentioned before, the absence of a time derivative in continuity equation and the absence of an explicit relationship between pressure and divergence-free condition on the velocity prohibit time integration in a straightforward manner by a stable time marching scheme. In this study, the continuity equation is modified to directly link the iterative changes in pressure to changes in velocity, as done in the Marker-and-Cell method.

2.2 Governing Equations in the Computational Domain

If the above equations are directly used on a Cartesian system to flow past complex geometries, the imposition of boundary conditions will require a complicated interpolation of the data on local grid lines, since the computational boundaries of complex geometries do not coincide with coordinate lines. This leads to a local loss of accuracy in the computed solution and leads to a complex program. To avoid these difficulties, a transformation from the physical domain (Cartesian coordinates (t, x, y, z)) to computational domain (generalized curvilinear coordinates (τ, ξ, η, ζ)) is used. After transformation from the physical domain to the computational domain, the governing equations can be written as :

$$\frac{\partial \hat{q}}{\partial \tau} + \frac{\partial}{\partial \xi} (\hat{E} - \hat{E}_v) + \frac{\partial}{\partial \eta} (\hat{F} - \hat{F}_v) + \frac{\partial}{\partial \zeta} (\hat{G} - \hat{G}_v) = 0 \quad (2.5)$$

where

$$\hat{q} = \frac{1}{J} \begin{bmatrix} 0 \\ u \\ v \\ w \end{bmatrix}$$

$$\hat{E} = \frac{1}{J} \begin{bmatrix} U - \xi_t \\ uU + p\xi_x \\ vU + p\xi_y \\ wU + p\xi_z \end{bmatrix}; \quad \hat{F} = \frac{1}{J} \begin{bmatrix} V - \eta_t \\ uV + p\eta_x \\ vV + p\eta_y \\ wV + p\eta_z \end{bmatrix}; \quad \hat{G} = \frac{1}{J} \begin{bmatrix} W - \zeta_t \\ uW + p\zeta_x \\ vW + p\zeta_y \\ wW + p\zeta_z \end{bmatrix} \quad (2.6)$$

and

$$\hat{E}_v = \frac{1}{J Re} \begin{bmatrix} 0 \\ (\nabla \xi \cdot \nabla \xi)u_\xi + (\nabla \xi \cdot \nabla \eta)u_\eta + (\nabla \xi \cdot \nabla \zeta)u_\zeta \\ (\nabla \xi \cdot \nabla \xi)v_\xi + (\nabla \xi \cdot \nabla \eta)v_\eta + (\nabla \xi \cdot \nabla \zeta)v_\zeta \\ (\nabla \xi \cdot \nabla \xi)w_\xi + (\nabla \xi \cdot \nabla \eta)w_\eta + (\nabla \xi \cdot \nabla \zeta)w_\zeta \end{bmatrix}$$

$$\hat{F}_v = \frac{1}{J Re} \begin{bmatrix} 0 \\ (\nabla \eta \cdot \nabla \xi)u_\xi + (\nabla \eta \cdot \nabla \eta)u_\eta + (\nabla \eta \cdot \nabla \zeta)u_\zeta \\ (\nabla \eta \cdot \nabla \xi)v_\xi + (\nabla \eta \cdot \nabla \eta)v_\eta + (\nabla \eta \cdot \nabla \zeta)v_\zeta \\ (\nabla \eta \cdot \nabla \xi)w_\xi + (\nabla \eta \cdot \nabla \eta)w_\eta + (\nabla \eta \cdot \nabla \zeta)w_\zeta \end{bmatrix}$$

$$\hat{G}_v = \frac{1}{J Re} \begin{bmatrix} 0 \\ (\nabla \zeta \cdot \nabla \xi)u_\xi + (\nabla \zeta \cdot \nabla \eta)u_\eta + (\nabla \zeta \cdot \nabla \zeta)u_\zeta \\ (\nabla \zeta \cdot \nabla \xi)v_\xi + (\nabla \zeta \cdot \nabla \eta)v_\eta + (\nabla \zeta \cdot \nabla \zeta)v_\zeta \\ (\nabla \zeta \cdot \nabla \xi)w_\xi + (\nabla \zeta \cdot \nabla \eta)w_\eta + (\nabla \zeta \cdot \nabla \zeta)w_\zeta \end{bmatrix} \quad (2.7)$$

with the contravariant velocities U , V and W :

$$\begin{aligned} U &= \xi_t + u\xi_x + v\xi_y + w\xi_z \\ V &= \eta_t + u\eta_x + v\eta_y + w\eta_z \\ W &= \zeta_t + u\zeta_x + v\zeta_y + w\zeta_z \end{aligned} \quad (2.8)$$

Here J is the Jacobian of transformation

$$J = \frac{\partial(\xi, \eta, \zeta)}{\partial(x, y, z)} = \begin{vmatrix} 1 & & & \\ x_\xi & x_\eta & x_\zeta & \\ y_\xi & y_\eta & y_\zeta & \\ z_\xi & z_\eta & z_\zeta & \end{vmatrix} \quad (2.9)$$

The quantities ξ_t , η_t and ζ_t are presented if the grid is in motion (as in the case of flow past an oscillating airfoil or a spinning propeller). These quantities are given in terms of the velocity of the grid (x_τ , y_τ , z_τ) with reference to a stationary observers :

$$\begin{aligned} \xi_t &= -x_\tau \xi_x - y_\tau \xi_y - z_\tau \xi_z \\ \eta_t &= -x_\tau \eta_x - y_\tau \eta_y - z_\tau \eta_z \\ \zeta_t &= -x_\tau \zeta_x - y_\tau \zeta_y - z_\tau \zeta_z \end{aligned} \quad (2.10)$$

CHAPTER III

NUMERICAL FORMULATION

The numerical procedure for solving the governing equation is an iterative time marching scheme which attempts to solve the discretized form of equations to a user-specified accuracy at any time step. Details of the iterative process are given in this chapter.

3.1 Grid Generation

The present method is a finite difference scheme which solves the discretized form of the partial differential equations at a set of discrete points in the flow field. Therefore, a set of grid points within the domain, including its boundaries, must be specified before solving the governing equations. Such a body-fitted grid system may be generated by conformal mapping, by algebraic method, or by partial differential equation techniques. In this study, body-fitted C-grid (Fig.1) and H-O grid system (Fig.5) are generated by an algebraic method for two-dimensional flow around NACA 0012 airfoil and three-dimensional flow around the ellipsoid of revolution, respectively. For the three-dimensional curved duct problem, a sheared/rotated Cartesian grid is used.

3.2 Grid Motion

In unsteady state computations, it is convenient to use a moving grid to account for the body motion. The grid is attached to the body and it rotates or translate with the body. The grid coordinates can be advanced explicitly by a first order time marching scheme :

$$\begin{aligned}x^{n+1} &= x^n + x_{\dot{x}}^n \Delta t \\y^{n+1} &= y^n + y_{\dot{y}}^n \Delta t \\z^{n+1} &= z^n + z_{\dot{z}}^n \Delta t\end{aligned}\tag{3.1}$$

However, if only a pure rotational motion is considered (say in a two-dimensional flow problem), new coordinates of grid at any instance in time can be simply obtained by using the following relations :

$$\begin{bmatrix} x \\ z \end{bmatrix} = \begin{bmatrix} \cos \theta & -\sin \theta \\ \sin \theta & \cos \theta \end{bmatrix} \begin{bmatrix} x' \\ z' \end{bmatrix} \quad (3.2)$$

where (x, z) is the instantaneous x, z values of the node and (x', z') is the x, z values of the node prior to rotation, and θ is the clockwise rotation angle. In such a case x_τ and z_τ may be found by analytical differentiation of (3.2) with respect to time or from (3.1).

3.3 Iterative Time Marching Procedure

The goal of the present procedure is to advance the flow properties (p, u, v, w) from a known time level 'n' to the next time level 'n+1'. First of all, let us consider the momentum equation. Since the momentum equation is a parabolic type of partial differential equation, it can be solved using a time marching scheme as follows :

$$\begin{aligned} \frac{1}{\Delta \tau} (\bar{q}^{n+1} - \bar{q}^n) + \delta_\xi \bar{E}^{n+m} + \delta_\eta \bar{F}^{n+m} + \delta_\zeta \bar{G}^{n+m} = \\ \delta_\xi \bar{E}_v^{n+m} + \delta_\eta \bar{F}_v^{n+m} + \delta_\zeta \bar{G}_v^{n+m} \end{aligned} \quad (3.3)$$

where \bar{q} is \hat{q} of Eq.(2.6) excluding the first row element, i.e.,

$$\bar{q} = \frac{1}{J} \begin{bmatrix} u \\ v \\ w \end{bmatrix} \quad (3.4)$$

Similarly, \bar{E} , \bar{F} , \bar{G} , \bar{E}_v , \bar{F}_v and \bar{G}_v can be also defined. For example,

$$\bar{E} = \begin{bmatrix} uU + p\xi_x \\ vU + p\xi_y \\ wU + p\xi_z \end{bmatrix} \quad (3.5)$$

The above discretization of Eq(3.3) is first order accurate in time if 'm' is zero or one, and second order accurate if 'm' is set to 1/2. The operators, δ_ξ, δ_η and δ_ζ represent second order accurate or higher order accurate spatial differences. The higher order spatial accuracy may be achieved on uniform grids using Pade approximations to the derivatives; on highly stretched grids, higher order accuracy may be achieved using a Lagrangean fit to the flow variables. In high Reynolds number flows, the Lagrangean fit need not be equally weighted about the node, but may be biased in the direction of flow. For example, when the flow is from left to right, if the Lagrangean interpolation of flow variables is done using nodes only to the left of, and including, the current node, then an upwind formulation results.

If the Newton iteration method is applied to solve this unsteady flow problem, Eq.(3.3) is rewritten as follows :

$$\frac{1}{\Delta\tau}(\bar{q}^{n+1, k+1} - \bar{q}^n) + \delta_\xi \bar{E}^{n+m, k+1} + \delta_\eta \bar{F}^{n+m, k+1} + \delta_\zeta \bar{G}^{n+m, k+1} = \delta_\xi \bar{E}_v^{n+m, k+1} + \delta_\eta \bar{F}_v^{n+m, k+1} + \delta_\zeta \bar{G}_v^{n+1, k+1} \quad (3.6)$$

Following a local linearization of \bar{E} , \bar{F} , \bar{G} , \bar{E}_v , \bar{F}_v and \bar{G}_v about the 'n+m' time level and at the 'k' iteration level, one may have

$$\left(I + \frac{\partial}{\partial \xi} A + \frac{\partial}{\partial \eta} B + \frac{\partial}{\partial \zeta} C \right) \Delta \bar{q} = \omega \bar{R}^{n+m, k} \quad (3.7)$$

where ω is a relaxation factor and A, B and C are the Jacobian matrices of the flux vectors $\bar{E} - \bar{E}_v$, $\bar{F} - \bar{F}_v$ and $\bar{G} - \bar{G}_v$, respectively:

$$A = \frac{\partial(\bar{E} - \bar{E}_v)}{\partial \bar{q}} \quad ; \quad B = \frac{\partial(\bar{F} - \bar{F}_v)}{\partial \bar{q}} \quad ; \quad C = \frac{\partial(\bar{G} - \bar{G}_v)}{\partial \bar{q}} \quad (3.8)$$

and $\bar{R}^{n+m, k}$ is the residual vector, defined as :

$$\bar{R}^{n+m, k} = -\frac{\bar{q}^{n+1, k} - \bar{q}^n}{\Delta\tau} - \left(\delta_\xi \bar{E}^{n+m, k} + \delta_\eta \bar{F}^{n+m, k} + \delta_\zeta \bar{G}^{n+m, k} \right) + \left(\delta_\xi \bar{E}_v^{n+m, k} + \delta_\eta \bar{F}_v^{n+m, k} + \delta_\zeta \bar{G}_v^{n+m, k} \right) \quad (3.9)$$

Note that when $\bar{R}^{n+m, k}$ goes to zero, the momentum equations in their discretized form are exactly satisfied, and the solution is independent of ω , and any approximations made in the construction of A, B and C.

Next, let's consider the continuity equation. As mentioned in Chapter I, in order to solve incompressible viscous flow problems efficiently, we need a relationship coupling changes in the velocity field with changes in the pressure field while satisfying the divergence-free constraint. In the present study, the Marker-and-Cell (MAC) approach is used to link the iterative changes between them, and can be written :

$$\Delta p = -\beta (\nabla \cdot \mathbf{v})^{n+1, k} \quad (3.10)$$

where $\Delta p = p^{n+1, k+1} - p^{n+1, k}$

and β is a relaxation factor, that may even vary from node to node using local time concept. Again, when Δp goes to zero, the continuity equation is exactly satisfied at each time step, even in unsteady flows.

In curvilinear coordinate system, Eq.(3.10) can be rewritten as :

$$\Delta \left(\frac{p}{J} \right) = -\beta \left[\frac{\partial}{\partial \xi} \left(\frac{U - \xi_t}{J} \right) + \frac{\partial}{\partial \eta} \left(\frac{V - \eta_t}{J} \right) + \frac{\partial}{\partial \zeta} \left(\frac{W - \zeta_t}{J} \right) \right]^{n+1, k} \quad (3.11)$$

The contravariant velocities, U, V and W are already defined in Eq.(2.8).

Eq.(3.10) states that if a cell is accumulating mass, then the pressure value at next iteration is increased to repel fluid away from the cell. If a cell is losing mass, then the pressure value is lowered to draw fluid. Thus the pressure field is iteratively updated along with the velocity field until the conservation of mass is satisfied.

Combining the momentum equation, Eq.(3.7) and the continuity equation, Eq.(3.11), and applying the numerical discretization in time and space at all nodes in the flow field, a system of simultaneous equation results for the quantity $\Delta \hat{q}$ equal to

$\left(\Delta \frac{p}{J}, \Delta \frac{u}{J}, \Delta \frac{v}{J}, \Delta \frac{w}{J} \right)$. This system may be formally written as :

$$[M] \{ \Delta \hat{q} \} = \{ R \} \quad (3.12)$$

Here, since the right hand side is the discretized form of the unsteady governing equations, as long as $\{\Delta t\}$ is driven to zero, the discretized form of unsteady Navier-Stokes equations are exactly satisfied at physical time level 'n+1'.

Although the matrix $[M]$ is a sparse, banded matrix, direct inversion of this matrix requires a huge number of arithmetic operations. A common strategy in iterative solutions of elliptic equations is to approximate the matrix $[M]$ by another, easily inverted matrix $[N]$. The closer the matrix $[N]$ is to $[M]$, the faster the iterative convergence of the solution at any time step. In this study, matrix $[N]$ contains only the diagonal contributions of matrix $[M]$, and Eq.(3.12) becomes an explicit form which is easier to be tailored for efficient execution on the current generation of vector or massively parallel computer architectures than an implicit form. This simplicity comes at the expense of the iterative speed. Acceleration of the iterative process above is a major contribution of this work to the state of the art.

The spatial derivatives of convective flux terms are differenced by using third order accurate upwind QUICK (Quadratic Upstream Interpolation for Convective Kinematics, ref.21) scheme to reduce unphysical oscillations or false diffusion for high Reynolds number flows, and the spatial derivatives of viscous terms are differenced using half-point central differencing. The spatial derivatives of continuity equation is differenced with central differencing and a fourth order artificial damping term is added to the continuity equation to stabilize the present procedure. The QUICK scheme is constructed that, instead of such a linear interpolation for the convective terms as used in standard one-sided differencing schemes, a three-point upstream weighted quadratic interpolation is used. For example, let's consider the convective term in ξ -direction which may be approximated as follows :

$$\frac{\partial}{\partial \xi} \left(\frac{uU}{J} \right) = \frac{1}{\Delta \xi} \left[\left(\frac{uU}{J} \right)_{i+\frac{1}{2}} - \left(\frac{uU}{J} \right)_{i-\frac{1}{2}} \right] \quad (3.13)$$

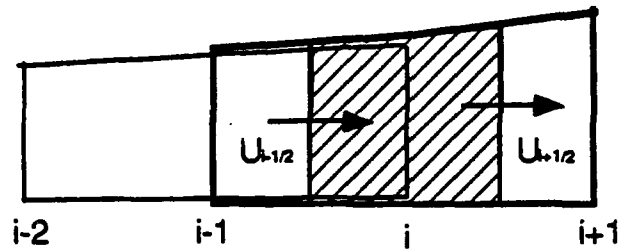
where

$$\begin{aligned} \left(\frac{uU}{J} \right)_{i+\frac{1}{2}} &= \left(\frac{U}{J} \right)_{i+\frac{1}{2}} \left\{ \frac{(u_{i+1} + u_i)}{2} - \frac{\Delta \xi^2}{8} \text{CURV}_{i+\frac{1}{2}} \right\} \\ \left(\frac{uU}{J} \right)_{i-\frac{1}{2}} &= \left(\frac{U}{J} \right)_{i-\frac{1}{2}} \left\{ \frac{(u_{i-1} + u_i)}{2} - \frac{\Delta \xi^2}{8} \text{CURV}_{i-\frac{1}{2}} \right\} \end{aligned} \quad (3.14)$$

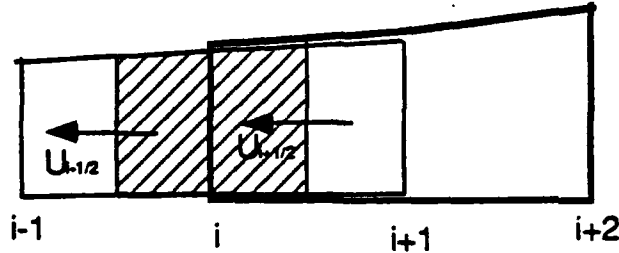
The curvature terms (CURV) depend on the direction of the contravariant velocity U :

$$\text{CURV}_{i+\frac{1}{2}} = \begin{cases} \frac{1}{\Delta\xi^2} (u_{i+1} - 2u_i + u_{i-1}) & \text{if } U_{i+\frac{1}{2}} > 0 \\ \frac{1}{\Delta\xi^2} (u_{i+2} - 2u_{i+1} + u_i) & \text{if } U_{i+\frac{1}{2}} < 0 \end{cases} \quad (3.15)$$

$$\text{CURV}_{i-\frac{1}{2}} = \begin{cases} \frac{1}{\Delta\xi^2} (u_i - 2u_{i-1} + u_{i-2}) & \text{if } U_{i-\frac{1}{2}} > 0 \\ \frac{1}{\Delta\xi^2} (u_{i+1} - 2u_i + u_{i-1}) & \text{if } U_{i-\frac{1}{2}} < 0 \end{cases} \quad (3.16)$$



(a)



(b)

Fig. 3.1. Quadratic upstream interpolation

(a) For $U > 0$ (b) For $U < 0$

3.4 Initial and Boundary Conditions

The governing equation (2.1) and (2.5) is a mixed elliptic-parabolic type of partial differential equation, and requires initial conditions to start the calculation as well as

boundary condition at every time step. The parabolic nature of the flow ensures that the flows will be independent of initial conditions, after large number of time step.

In the present work, the quantities Δp , Δu , Δv and Δw are set to zero at all solid and fluid boundaries. The boundary conditions are updated after every interior points updated during each iteration. Thus the boundary values as well as interior values are iteratively advanced from a time level 'n' to 'n+1'.

Initial Conditions :

In the case of external flows, we assume that the object is impulsively started from rest. Therefore, the uniform freestream conditions are used as initial conditions. In the case of internal flows, parallel flow solutions (e.g. Poiseuille flow in a square duct) are used to start the calculations.

Farfield Boundary Conditions :

For external flow applications, the farfield boundary is placed far away from the solid surface. Thus, it is natural to specify the freestream values at the farfield boundaries except along the outflow boundary where the extrapolation for velocities in combination with $p = p_{\infty}$ is used, to account for the removal of vorticity from the flow domain by convective process.

Boundary Conditions on the Solid Surface :

On the solid surface, the no slip condition is imposed for velocity components. The surface pressure distribution is determined by solving the normal gradient of pressure to be zero :

$$\frac{\partial p}{\partial n} = 0 \quad (3.17)$$

Some researchers (ref.22, 23) obtain the boundary conditions for pressure from the normal component of momentum equation at the wall

$$\frac{\partial p}{\partial n} = \frac{1}{Re} \frac{\partial^2 u_n}{\partial n^2} \quad (3.18)$$

where u_n is the normal component of velocity. In high Reynolds number flows, the viscous stress contribution to the normal momentum equation can be neglected at the wall and the grid point adjacent to the surface will be sufficiently fine so that constant pressure normal to the surface can be assumed. Thus Eq.(3.17) is an acceptable boundary condition.

Boundary Conditions on the Cut and Singular Line :

Since the C-grid and the H-O grid which are used for two-dimensional airfoil problem and three-dimensional body of revolution have a cut and singularlines, respectively, special treatment is needed (see Fig. 3.2 and 3.3). Across the cut of the C-grid system, flow quantities should be continuous. The flow quantities on the cut can be obtained by averaging the flow properties from above and below the cut. On the singular lines that occur in a H-O grid system, the flow quantities are obtained by extrapolating from two adjacent interior points and then averaging them azimuthally to ensure that the flow quantities are single-valued.

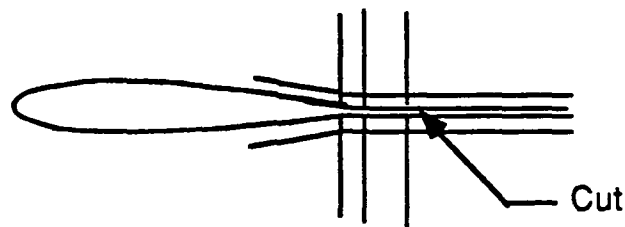


Fig.3.2 Cut of the C-grid system

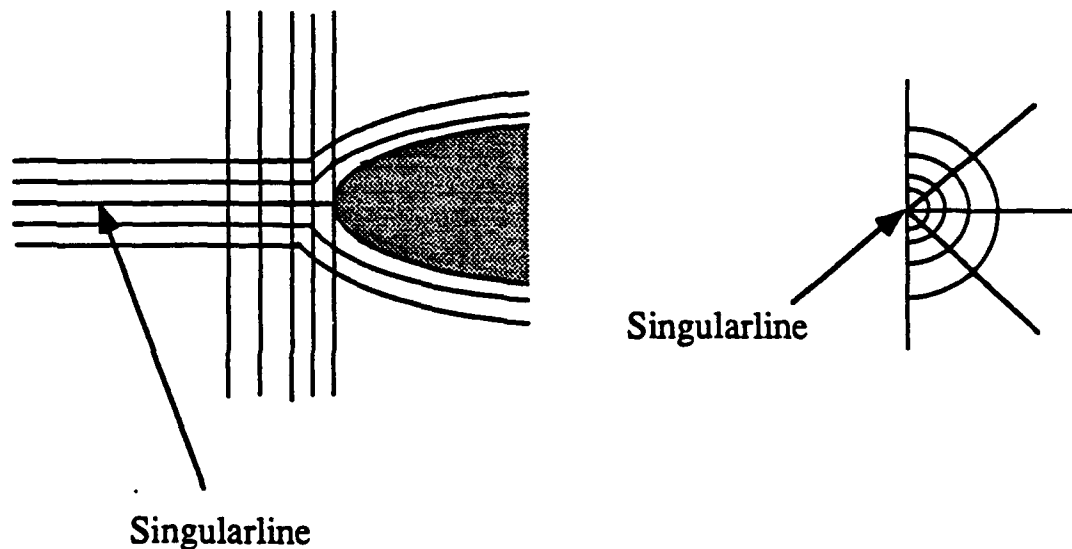


Fig.3.3. Singularline of the H-O grid system

3.5 Acceleration by Multigrid Technique

Since the matrix [N] (which is an approximate to matrix [M] of Eq.(3.12)) is a simple diagonal-matrix, it leads to slow convergence of the pressure and velocity fields at every time step. Use of such a simple diagonal matrix simplifies the inversion, and makes the flow solver 100% vectorizable and parallelizable. To accelerate the present procedure, a multigrid technique (Coarse Grid Correction method) is applied in this study.

The principles behind the present multigrid technique are as follows. The quantities (Δu , Δv , Δw , Δp) may be viewed as Fourier series-like sums made of components of different wave lengths. An extremely coarse grid linking a point to a node several units away is effective in computing the long wave length components. A very fine grid is effective in computing the short wave length components, and is very inefficient for computing the long wave length components. The multigrid technique attempts to compute these individual components of Δq on grids of several levels efficiently. When the process converges, of course, the discretized equations (i.e. RHS of Eq.(3.7) and (3.11)) are exactly satisfied on the finest grid.

The coarse grid correction algorithm presently used (given here for 2-grid sequence for simplicity) is as follows :

- i) Compute the residual {R} appearing on the right hand side of Eq.(3.12) on the fine grid using $q^{n+1,k}$.
- ii) Transfer the residual from the fine grid to the coarse grid using the injection operation, $I_h^{2h} R$. An injection operation is given at any node (i,j) in two-dimensional case by

$$I_h^{2h} R_{i,j} = R_{i,j} + \frac{1}{2}(R_{i+1,j} + R_{i-1,j} + R_{i,j+1} + R_{i,j-1}) + \frac{1}{4}(R_{i+1,j-1} + R_{i-1,j+1} + R_{i-1,j-1} + R_{i+1,j+1}) \quad (3.19)$$

and in three-dimensional case :

$$I_h^{2h} R_{i,j,k} = R_{i,j,k} + \frac{1}{2}(R_{i,j-1,k} + R_{i+1,j,k} + R_{i,j+1,k} + R_{i-1,j,k} + R_{i,j,k-1} + R_{i,j,k+1}) + \frac{1}{4}(R_{i-1,j-1,k} + R_{i+1,j-1,k} + R_{i+1,j+1,k} + R_{i-1,j+1,k} + R_{i,j-1,k-1} + R_{i,j+1,k-1} + R_{i,j+1,k+1} + R_{i,j-1,k+1} + R_{i-1,j,k-1} + R_{i+1,j,k-1}) \quad (3.20)$$

$$\begin{aligned}
& + R_{i+1,j,k+1} + R_{i-1,j,k+1}) + \frac{1}{8} (R_{i-1,j-1,k-1} + R_{i+1,j-1,k-1} \\
& + R_{i+1,j+1,k-1} + R_{i-1,j+1,k-1} + R_{i-1,j-1,k+1} + R_{i+1,j-1,k+1} \\
& + R_{i-1,j+1,k+1} + R_{i+1,j+1,k+1})
\end{aligned}$$

iii) Compute the quantity Δq at every point on the coarse grid by solving the system of equation :

$$[N]\{\Delta q / J\} = \{I_h^{2h} R\} \quad (3.21)$$

iv) Interpolate the Δq values computed in step (iii) back on to the fine grid by using the bilinear interpolation.

v) Compute the updated values of the flow properties $q^{n+1,k+1}$ as $q^{n+1,k} + \Delta q$.

Repeat step (i) - (v) till Δq is driven to zero.

The present 2-D solver accepts grids upto 3 levels.

To the writer's knowledge, the multigrid technique in unsteady incompressible flows has been applied only to pressure-Poisson equation. The u-, v- and w- momentum equations are usually solved only on a single grid. The present work fully exploits the benefits of the multigrid method for all the equations, while keeping the form of the matrix $[N]$ extremely simple. This allows use of larger time steps and improved convergence as discussed on Chapter IV. The present investigator applied a conjugate gradient like scheme, called the GMRES (Generalized Minimal Residuals) to solve Eq.(3.12). The matrix $[N]$ was used as the preconditioner. The success of the GMRES scheme crucially depends on the closeness of $[N]$ to $[M]$. That is the eigenvalues of the matrix $[I - N^{-1}M]$ must be small and closely packed. The use of GMRES with $[N]$ as a preconditioner was not successful.

CHAPTER IV

RESULTS AND DISCUSSION

In this chapter, the work done to date is presented. To validate the present procedure, three cases were tested. The first test case is two-dimensional unsteady viscous flow over an oscillating airfoil. The second is three-dimensional steady flow over an ellipsoid of revolution. The third is the flow through a curved duct. Numerical results are presented in the form of instantaneous streamlines, velocity profiles, vorticity contours, surface pressure distribution, and aerodynamic loads. Streamlines and surface pressure distributions are compared with flow visualization and the other available numerical data .

4.1 Dynamic Stall of an Oscillating Airfoil

The computations were carried out for a sinusoidally pitching NACA 0012 airfoil, at $Re = 5,000$ and $\kappa = 0.5$, where κ is reduced frequency of oscillation, defined by

$$\kappa = \frac{\Omega c}{2 V_{\infty}} \quad (4.1)$$

where Ω is the radians of rotation per second and c is chord of airfoil. The physical interpretation of reduced frequency is the number of radians of oscillation per semi-chord length of travel. This case has been previously studied by Mehta (ref.3) at NASA Ames Research Center using a velocity-vorticity formulation and its flow visualization was carried out by Werlé (ref. 24) in ONERA.

After the flow is fully developed at zero angle of attack, the airfoil is allowed to oscillate in pitch through an angle of attack range from 0 degree to 20 degree given by $\alpha = 10^\circ(1 - \cos t)$. Fig.1 shows the body-fitted grid around the airfoil used in this study. Fig.2 shows the instantaneous streamlines (actually, called particle tracers in PLOT3D software), velocity profiles and vorticity contours at selected angle of attack. Fig.3 shows the surface pressure distribution. In general, the streamline patterns and surface pressure distributions are in very good agreement with flow visualization and Mehta's numerical

results except that the present procedure predicts a little earlier generation of vortex than Mehta's method. The flow visualizations were carried out with air bubble in the water tunnel. Here, we should note that photographs showing air bubble trajectories were taken at an exposure time of 1/10 seconds. Therefore, in unsteady flow the air bubble trajectories near the surface of airfoil represent neither streamlines nor streaklines because the pictures contain many paths over the exposure time. On the other hand, the instantaneous streamline is a streamline at any instant of time, i.e. we assume the flowfield is frozen at any instant of time and draw the streamline. In other words, the instantaneous streamline is equivalent to the bubble trajectories with an infinitesimal exposure time. Thus, the flow visualization with air bubble is different from the instantaneous streamline, and should be used only for qualitative comparison. Fig.4 shows the lift, drag and moment hysteresis loops. The main feature of dynamic stall which is significantly different from static stall is due to the generation of a vortex near the leading edge. This vortex passes over the upper surface of airfoil, creating large variations in the aerodynamic forces and moment. From these figures, it is seen that the growth of lift during the upstroke is slow and gradual, well past the static-stall angle. The separation region, which is present over a small region near the trailing edge at first, moves upstream as the angle of attack increases. The pitching moment does not change much during the upstroke. The surface pressure distribution at an angle of attack of 18.6 degree shown in Fig.3 shows another pressure peak near the quarter chord. This indicates the leading-edge vortex is already generated, and this can be identified in Fig.2 (c). As the leading-edge vortex moves downstream, the chordwise surface pressure distribution and aerodynamic forces are significantly varied, especially during the downstroke. This variation may depend on the Reynolds number, airfoil shapes and reduced frequency. The moment stall, associated with an increase of negative moment, begins at about 18.5 degree in the downstroke.

4.2 3-D Steady Flow over an Ellipsoid of Revolution

To validate the capability of the present method to handle three-dimensional viscous flows, the present procedure was tested by computing the flow past a 6:1 ellipsoid of revolution at 10 degree angle of attack, at a Reynolds number of 5,000. Fig.5 shows the body-fitted grid system. Fig.6 shows streamlines over the body surface. There is a limited amount of experimental data (ref.25, 26) available for this particular configuration, at high Reynolds number ($Re=7.2 \times 10^6$). Fig.7 shows the surface pressure distribution on the windward and leeward sides of the symmetry plane, along with the experimental data.

Good agreement is evident everywhere except in the last 10% of the body, where the present laminar simulation predicts flow separation, and a flattening out of the pressure distribution.

4.3 3-D Steady Flow through a 90° Bended Square Duct

To validate the capability to handle three-dimensional internal flow problems, the flow within a square duct with a 90-deg bend was tested. The radius of curvature of the inner wall in the curved section is 1.8 times of the side length of square cross-section. This particular configuration (Fig.8) was experimented by Humphrey et al. (ref.27) and numerically calculated by Kwak et al.(ref.19) at a Reynolds number of 790 based on the average inflow velocity and hydraulic diameter. The inflow and outflow velocity profile are obtained by solving the equation of fully developed duct flow (ref.28) :

$$\frac{\partial^2 u}{\partial y^2} + \frac{\partial^2 u}{\partial z^2} = \frac{1}{\mu} \frac{dp}{dx} = \text{const.} \quad (4.2)$$

This equation is a standard form of Poisson equation and can be solved by ADI scheme. Fig.9 shows the streamwise velocity profiles compared with the experimental data of Humphrey et al. and numerical data of Kwak et al. The results are in general good agreement with experiments and the other numerical solution. The present grid system is 75x41x41. In Fig.10, the cross-sectional velocity profiles are plotted at $\theta = 30, 60$ and 90 deg. The top side and bottom side of cross-section are the inside wall and outside wall, respectively. In this figure, the pair of vortices and the secondary flow are shown. These vortices are generated due to the pressure difference between the higher pressure on the outside wall and lower pressure on the inside wall. Fig.11 and 12 show the velocity magnitude contours and the vorticity magnitude contours at the three selected streamwise stations, respectively. The plot on the left side of Fig.13 is a sideview of streamwise velocity profiles at $y/y_{1/2} = 0.5$, which is midway between the left side wall and the symmetry plane of square duct and the right side plot is at $y/y_{1/2} = 0$, which is on the symmetry plane. The inside and outside wall are corresponding to $z = 0$ and $z = 1$, respectively. Fig.14 shows streamwise velocity profiles from a viewpoint which is located at upper 45° in the xz -plane. The plot at $z = 0.25$ is corresponding to the midway plane between the inside wall and the plane of symmetry. The plots at $z = 0.5$ and 0.75 are on

the plane of symmetry and the midway between the outside wall and the symmetry plane, respectively. Fig.15 is the streamlines viewing from the three different viewpoints, i.e., front, oblique, and side view. We can see the vortex pair which is originating from about $\theta = 0^\circ$. Fig.16 is the pressure contours in the curved section and shows the higher pressure on the outer wall due to the centrifugal forces.

4.4 Acceleration of Flow Solver by Multigrid Technique

The multigrid technique was implemented to the two- and three-dimensional solver. In two-dimensional case, the fine grid system has (81×41) grid points and the coarse grid system has the half of the fine grid points, i.e. (41×21) grid points, and the coarsest grid system has (21×11) grid points. The two grid system consists of the fine and coarse grid system (Fig. 4.1.(a)) and the three grid system consists of all of them as shown in Fig.4.1.(b). Especially, three grid system such as Fig. 4.1.(b) is called V-cycle.

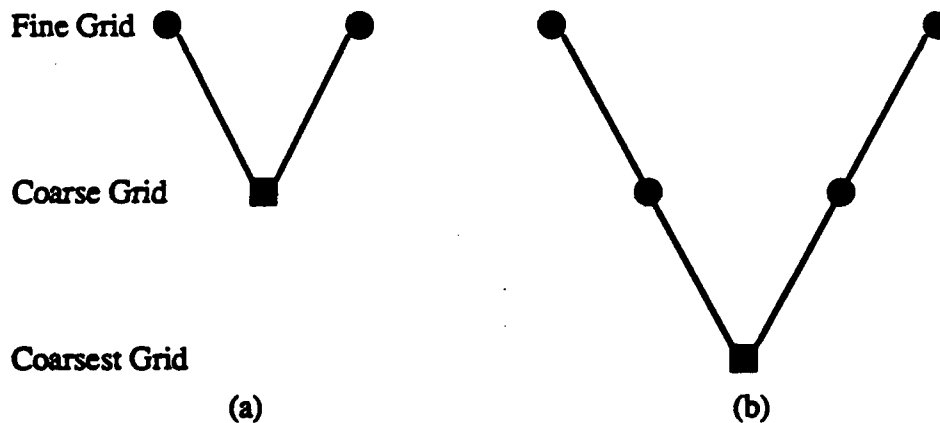


Fig. 4.1 Structure of multigrid cycle

(a) Two-grid system

(b) Three-grid system

Fig.17 shows the convergence history of the global residual (l_2 -norm of RHS of Eq (3.12)) reduction in CPU time for 2-D steady flow over NACA 0012 airfoil at zero angle of attack. Upto 40% and 60% acceleration was obtained using two- and three-grid system,

respectively. The CPU time is based on 25 iterations at each time step on an IBM RISC/6000 workstation. Fig.18 shows the history of global residual of 2-D unsteady state for sinusoidally oscillating airfoil (50 iterations/time step), where the three-grid system is used for multigrid. The residual by the multigrid technique maintains lower level than that of single grid iteration procedure indicating that the discretized equations are solved to much high levels of accuracy using the multigrid technique. The surface pressure distribution and dynamic stall hysteresis is nearly the same as those of single grid system and are not plotted here. In three-dimensional case, the multigrid technique was implemented to the flow solver for 90° bended square duct problem. The three level of grid system consists of (65x21x21), (33x11x11), and (17x6x6). Fig.19 shows the comparison of convergence history with and without multigrid method. Here we got much better quality of solutions with multigrid technique than were without multigrid technique. Furthermore, The grid system (65x21x21) is so coarse that it can not detect the sufficiently strong vortex core and the residual of solution without multigrid technique remains of the order of 10^0 . Thus the solution with single grid/non-multigrid version is not accurate. The comparison of solutions with multigrid and without multigrid is shown in Fig.20. The solutions of fine grid(75x41x41) system with single grid are also plotted to compare the intensity of vortex. From this figure, it is clear that the multigrid analysis is adequately resolving the counter-rotating vortex pair.

4.5 3-D Steady Flow around a Marine Propeller

The flow around a marine propeller is a challenging problem because the geometry is much more complex than the aircraft wing and helicopter blades. The high twist, low aspect ratio, close proximity of other blades and high rotational speed make the flow around a propeller highly three-dimensional and complex, featuring centrifugal forces, formation of curved tip vortices and leading edge vortices.

Technique for efficient and accurate prediction of 3-D incompressible viscous flow around a marine propeller are necessary for accurate prediction of performance. Moreover, the lack of such tools is a major obstacles to the accurate calculation of cavitation and propeller noise.

Numerical methods to solve flow around propellers range from Goldstein's strip theory (1929) to Navier-Stokes equation solvers. The Goldstein's strip theory models the propeller by a lifting line vortex in a potential flow and assumes that the wake is a rigid

helical vortex sheet. This theory can handle only a straight blade without a nacelle. Sullivan (1977) and Egolf (1979) improved this theory to account for blade sweep and nacelle by using the curved lifting line concept and vortex filaments. A review of potential flow method applicable to propellers is well described by Kerwin (1986). Jou (1982) has applied the full potential equation with a finite volume approach to solve propfans but his method can not catch the strong rotational flow effects near the leading edge. Euler equations have been applied by many researchers such as Chaussee (1979, 1983), Bober (1985, 1986) and Whitfield (1987). For a more accurate prediction, Srivastava and Sankar (1990) developed an iterative method which couples the Euler equation solver and NASTRAN to model structural deformation due to aerodynamic forces and centrifugal forces. Full Navier-Stokes equations have recently been applied to advanced propfans by Matsuo (1988) and Hall (1991). Lim and Sankar (1993) extended the Euler equation solver of Srivastava and Sankar to full Navier-Stokes equations using the Roe upwind scheme. These Navier-Stokes equation solvers are based on the compressible Navier-Stokes equations and can not accurately predict incompressible flow solutions. Kim (1989) applied incompressible Navier-Stokes equations in the cylindrical coordinate to an infinite-pitch marine propeller with rectangular blades by using the SIMPLER algorithm. Although their work can simulate marine-propeller flow fields, including propeller loading and complex blade-to-blade flow, the infinite pitch propeller with rectangular blade shape is not realistic and no experimental data is available for comparison.

The above procedure for solving 3-D unsteady incompressible viscous flows without cavitation has been applied to the flow around a 2-bladed SR7L propeller as shown in Fig.1. The present scheme is time accurate and the steady state solutions are obtained as asymptotic solution of the time marching process. Fig.2 shows the H-O grid for a 2-bladed SR7L propeller. Fig.3 shows the pressure coefficient distribution at some selected spanwise location at a nondimensional time of 0.3 in a single grid system (without acceleration by multigrid technique), compared with experimental data by Bushnell (1988) and compressible Navier-Stokes equation solutions by Lim and Sankar. A fairly good agreement with experimental and other numerical data was achieved except near the leading edge region. These discrepancies are because at the nondimensional time = 0.3, the flow has not evolved enough to generate leading edge vortices. At later time levels, it is anticipated that the suction peak near the leading edge will be higher.

CHAPTER V

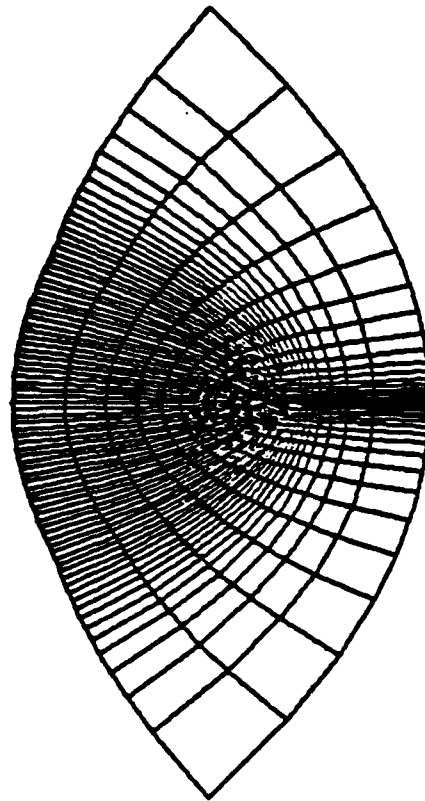
CONCLUDING REMARKS

An accurate and efficient iterative time marching procedure for two- and three-dimensional unsteady, incompressible, viscous flow has been developed. It has been applied to the following cases with success :

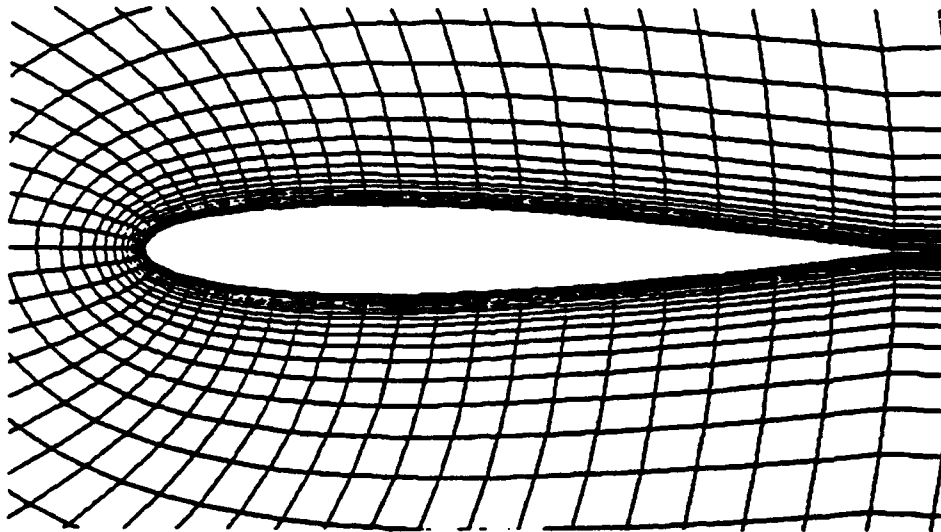
- (a) Massively separated flow over oscillating airfoil,
- (b) Three-dimensional flow past an ellipsoid of revolution,
- (c) Three dimensional flow through a square duct with a 90-deg. bend
- (d) Three-dimensional flow around a marine propeller.

Good agreement with published experimental and numerical data has been obtained. After the validation of the present procedure, techniques for acceleration were explored. It was found that the multigrid technique was efficient in reducing the CPU time needed for the simulation and improved the solution quality because of the lower residuals achieved.

This report is a draft copy of the Ph. D. dissertation of Mr. Warn-Gyu Park, and will in its completed form include changes suggested by the thesis committee. A copy of the finished form of the thesis will be mailed to the sponsor around March 1993.

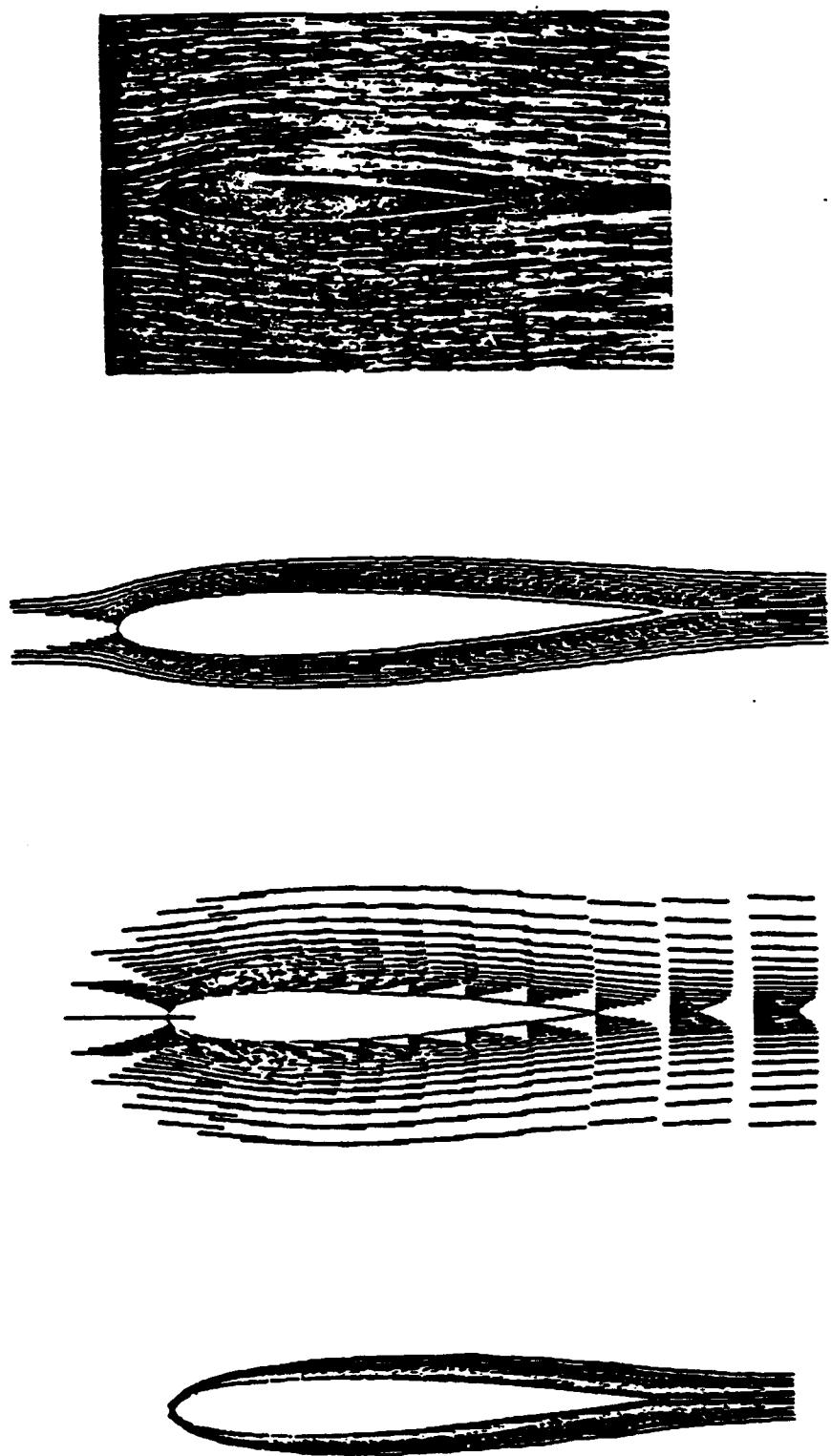


(a)



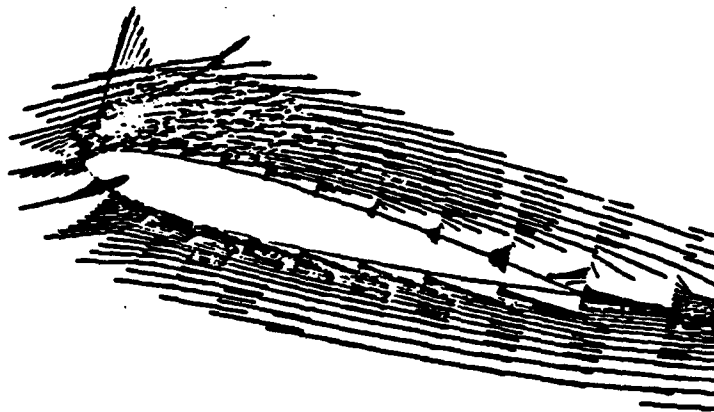
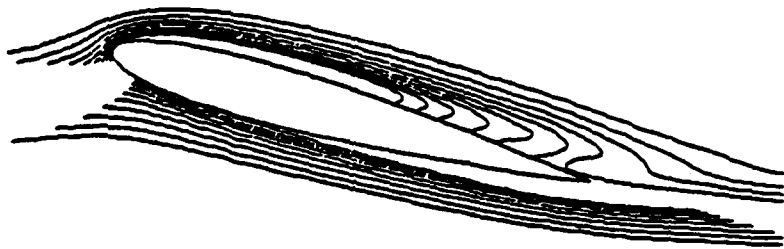
(b)

Figure 1. Body-Fitted Grid Around a NACA 0012 airfoil



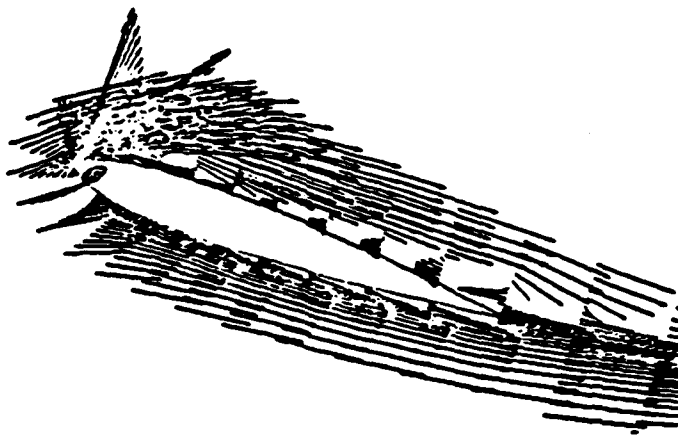
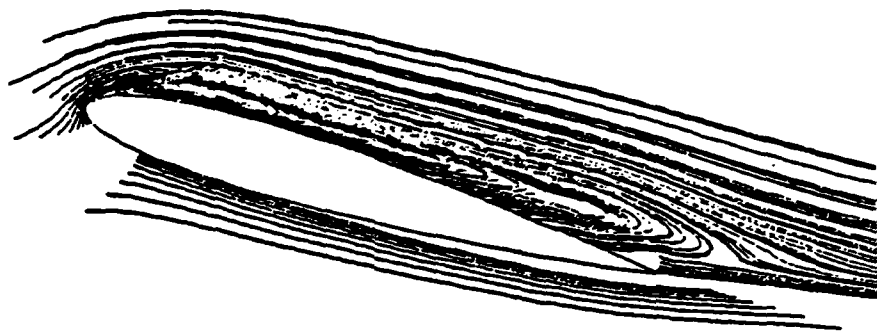
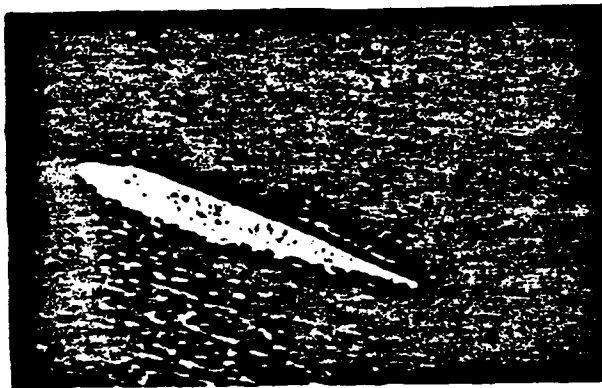
(a) $\alpha = 0$ (deg)

Figure 2. Instantaneous Streamlines, Velocity Profiles, and Vorticity Contours at Selected Angle of Attack with Experimental Flow Visualizations



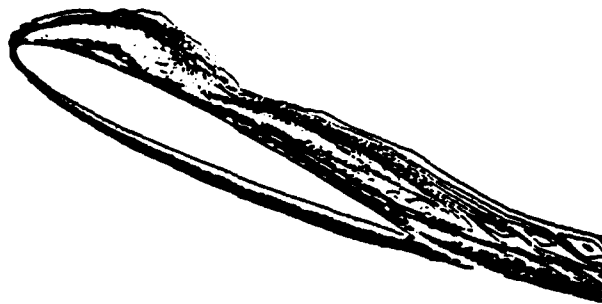
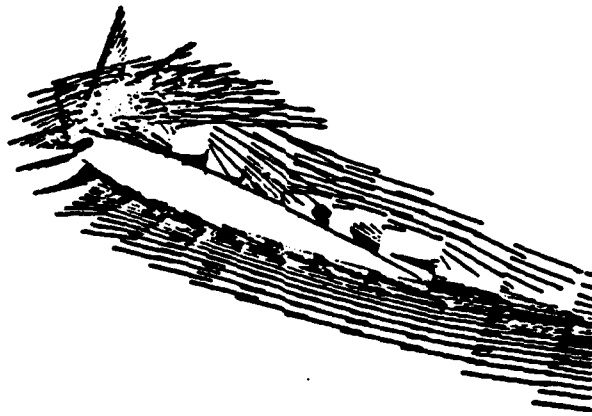
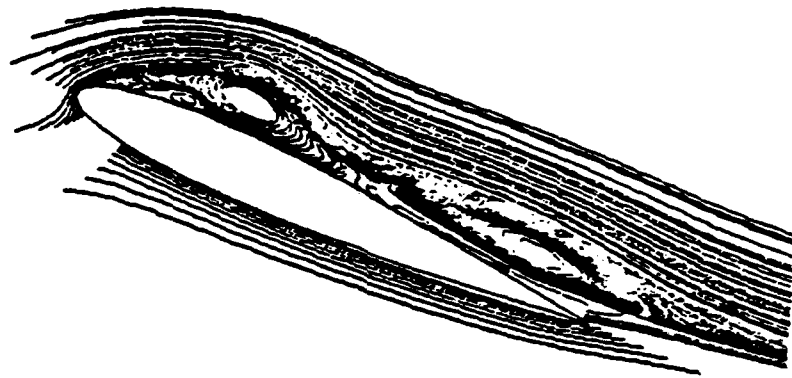
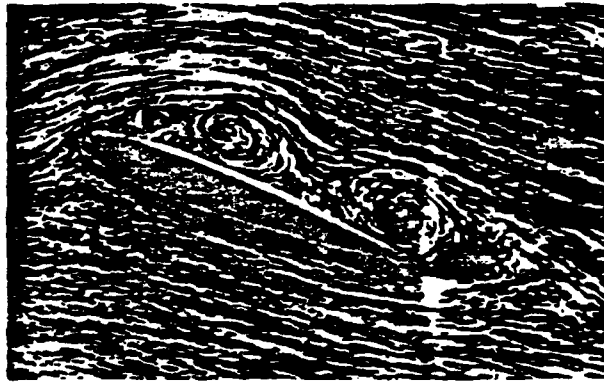
(b) $\alpha = 14.6$ (deg)

Figure 2. Continued..



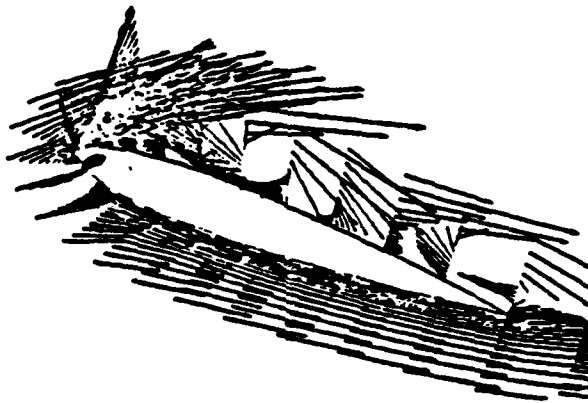
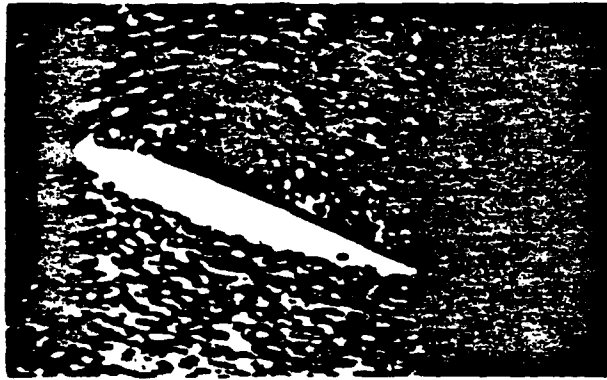
(c) $\alpha = 18.8$ (deg)

Figure 2. Continued.



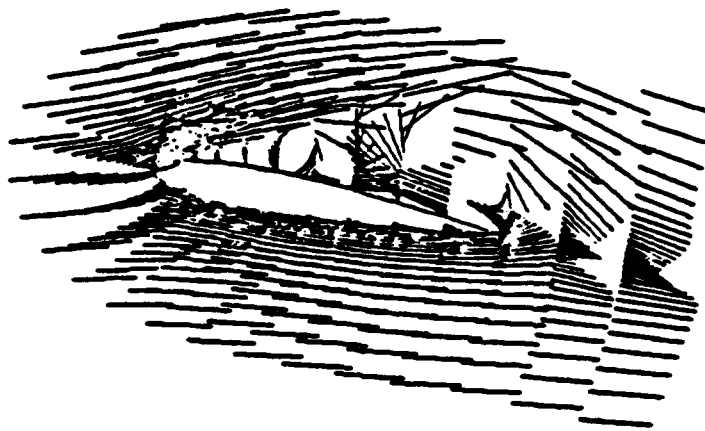
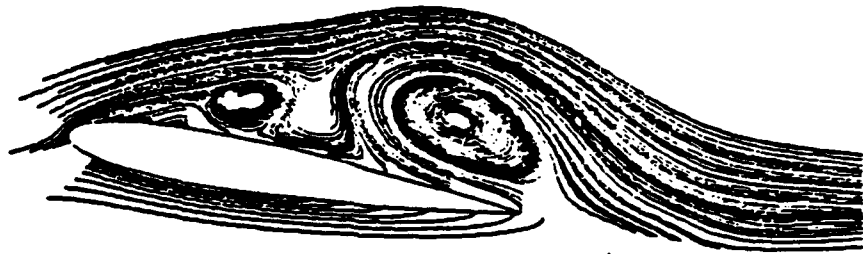
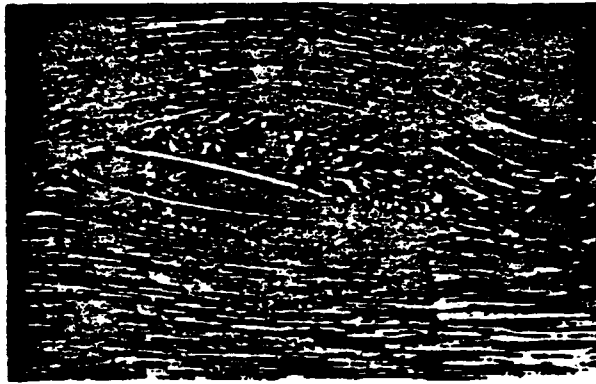
(d) $\alpha = 20$ (deg)

Figure 2. Continued.



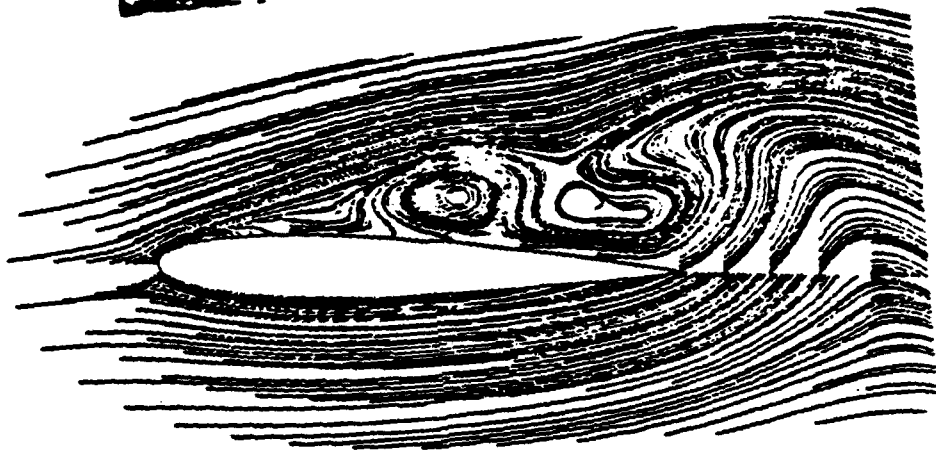
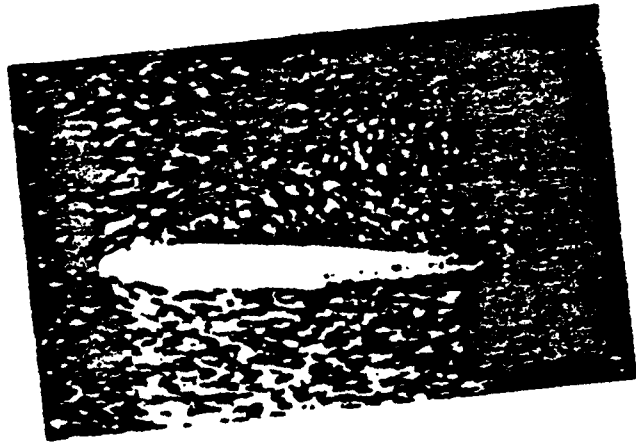
(e) $\alpha = 19.8$ (deg)

Figure 2. Continued.



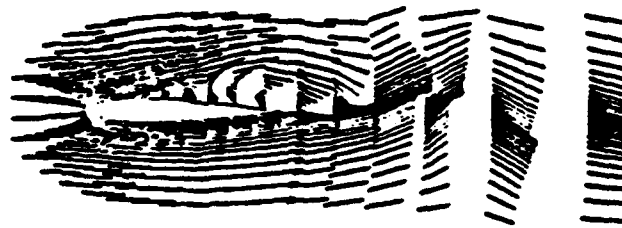
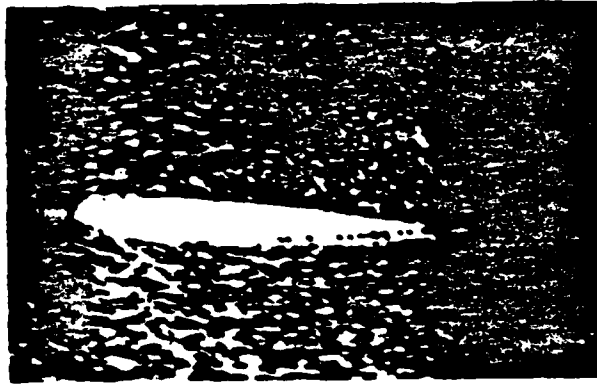
(f) $\alpha = 11$ (deg)

Figure 2. Continued.



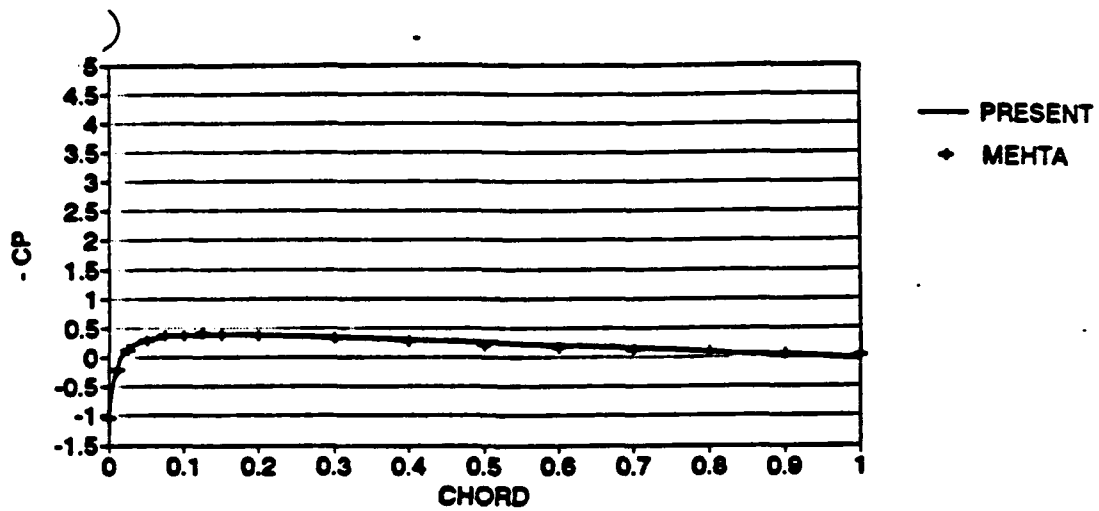
(g) $\alpha = 5$ (deg)

Figure 2. Continued.

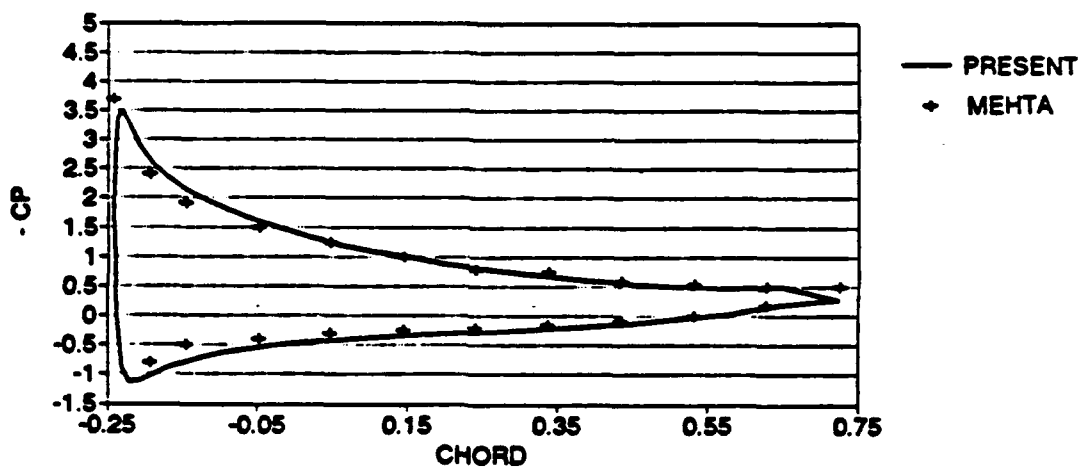


(h) $\alpha = 1$ (deg)

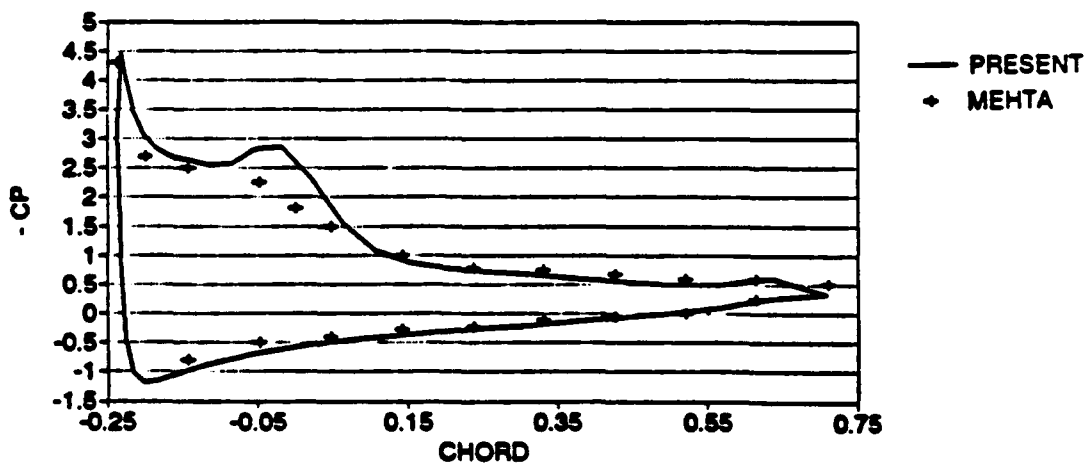
Figure 2. Continued.



(a) $\alpha = 0$

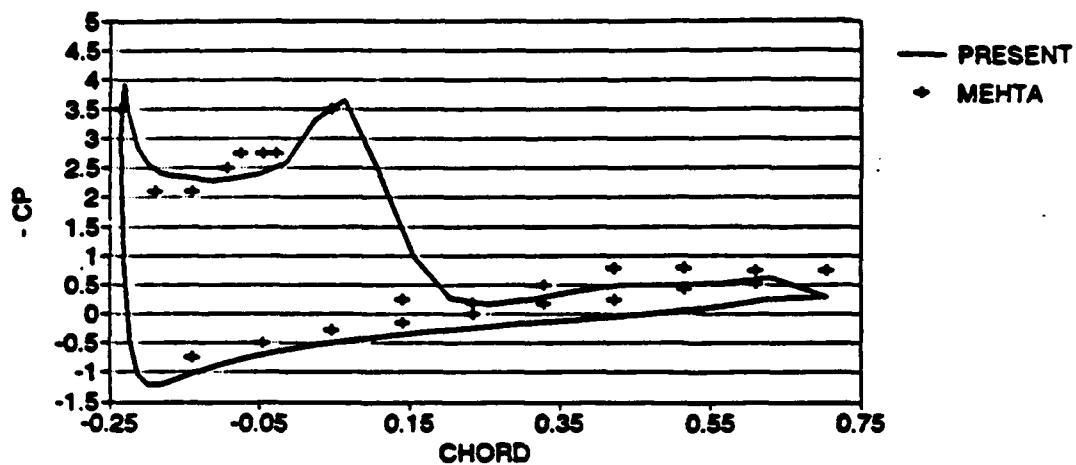


(b) $\alpha = 14.6$

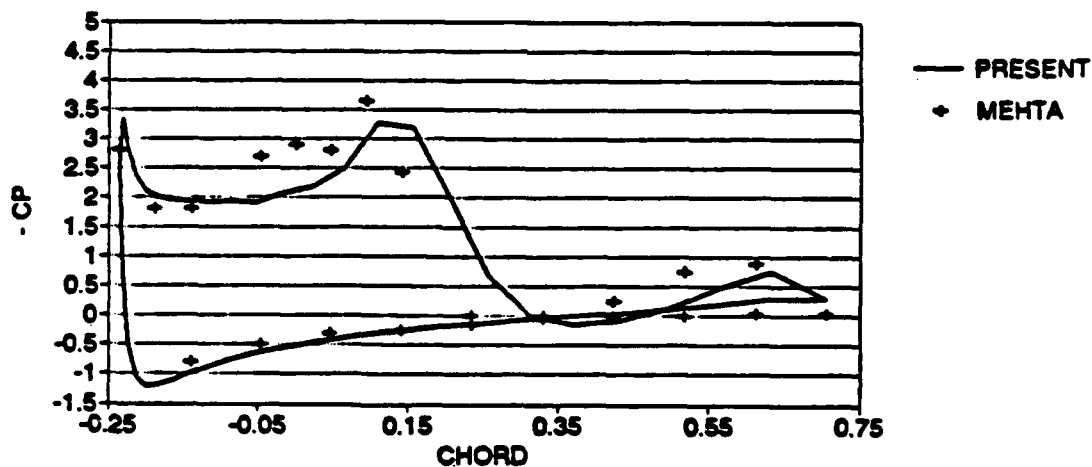


(c) $\alpha = 18.8$

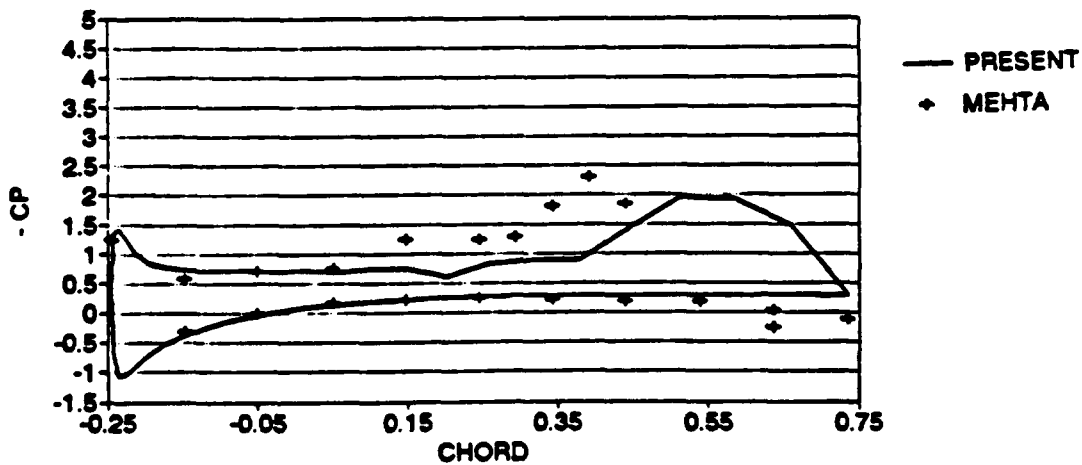
Figure 3. Surface Pressure Distributions at Selected Angle of Attack



(d) $\alpha = 20$

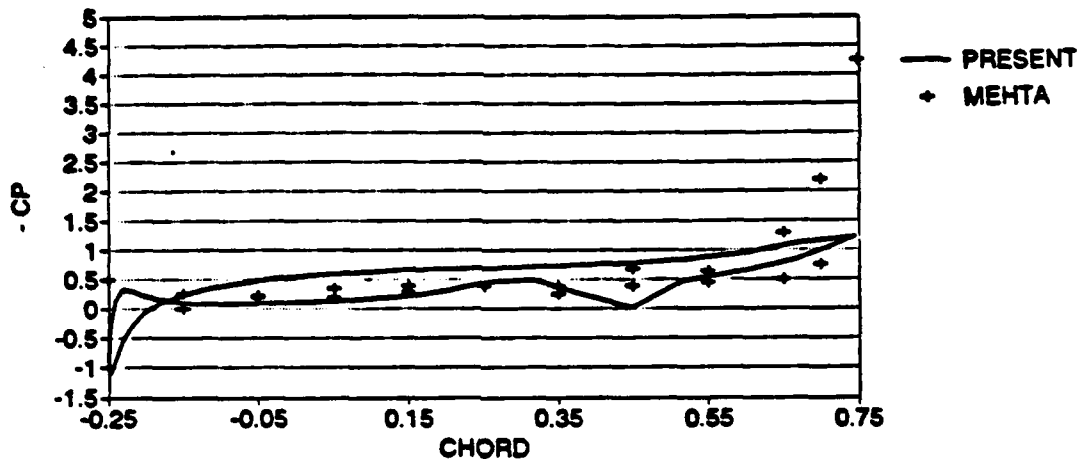


(e) $\alpha = 19.8$

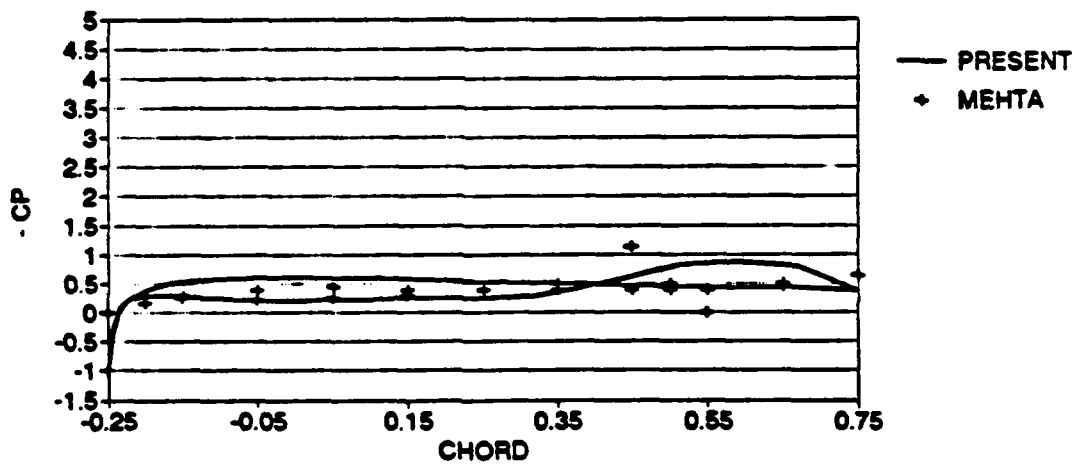


(f) $\alpha = 11$

Figure 3. Continued.

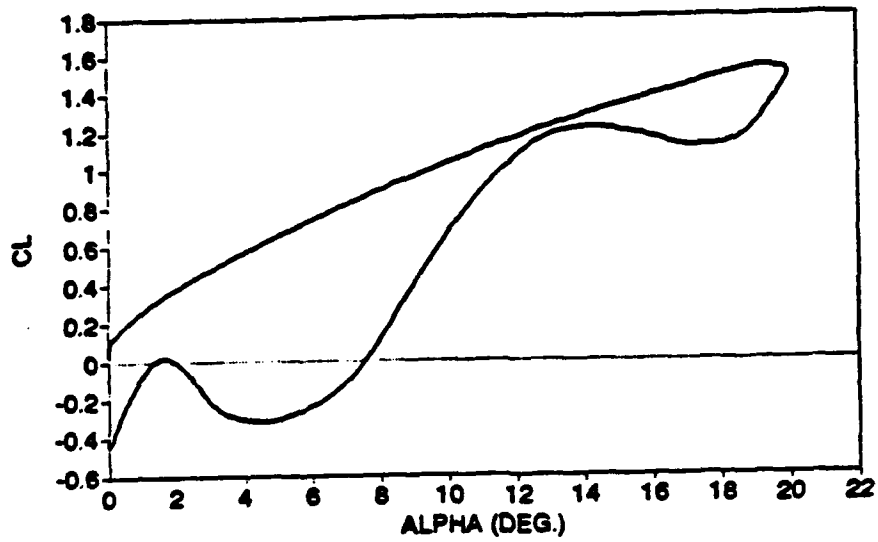


(g) $\alpha = 5$

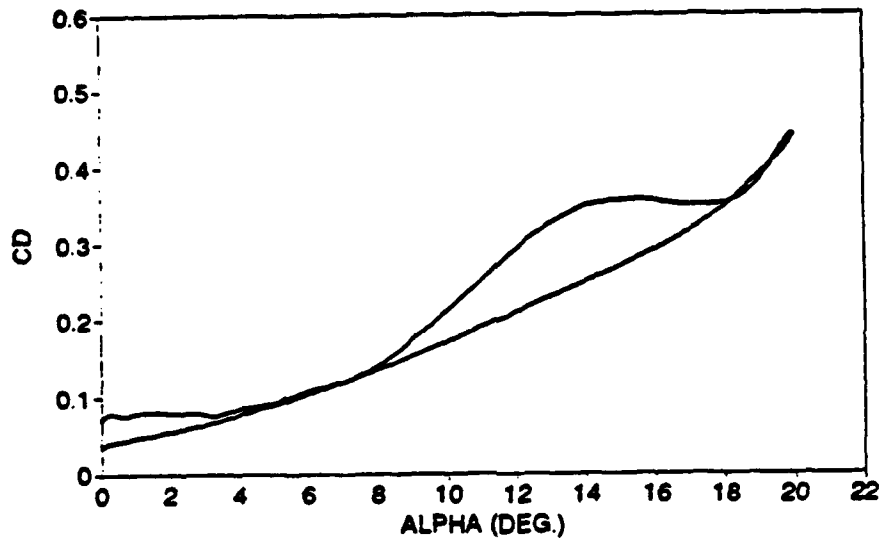


(h) $\alpha = 1$

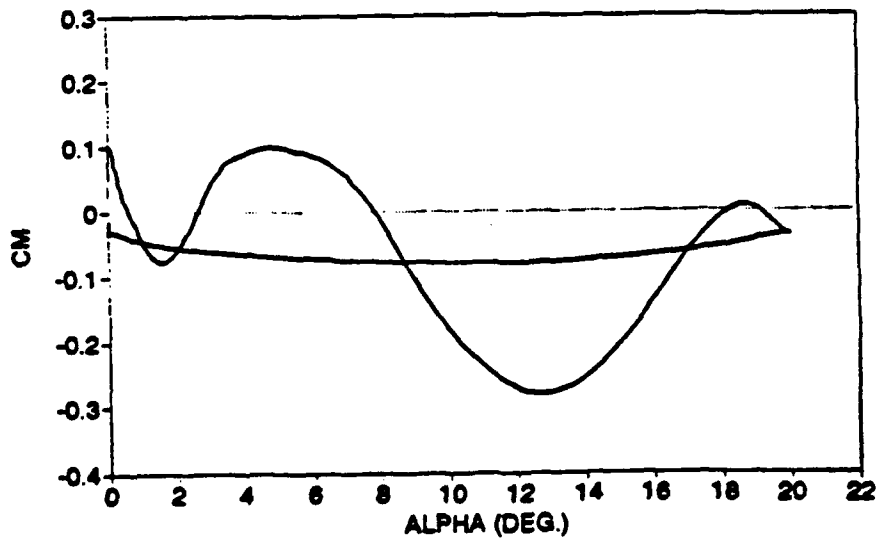
Figure 3. Continued.



(a)

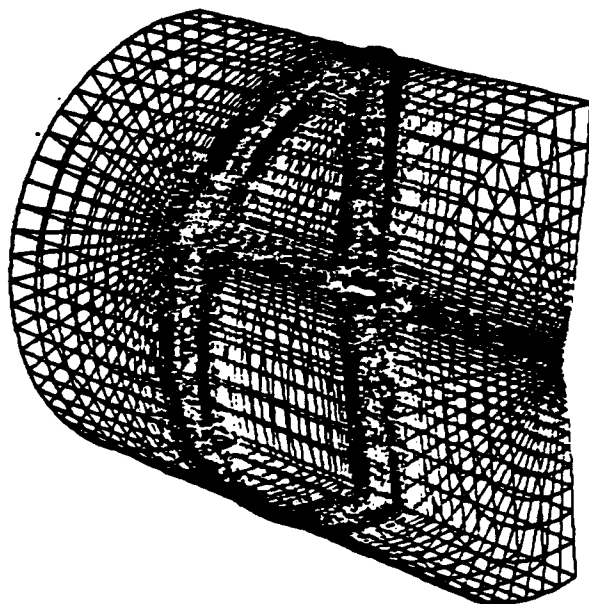


(b)

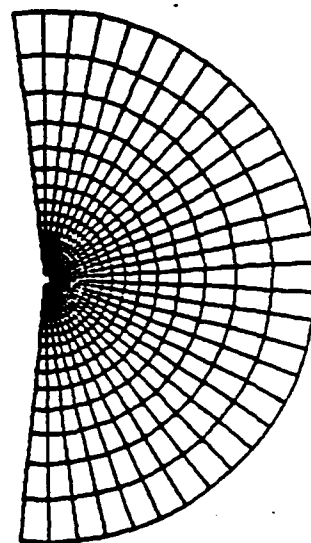


(c)

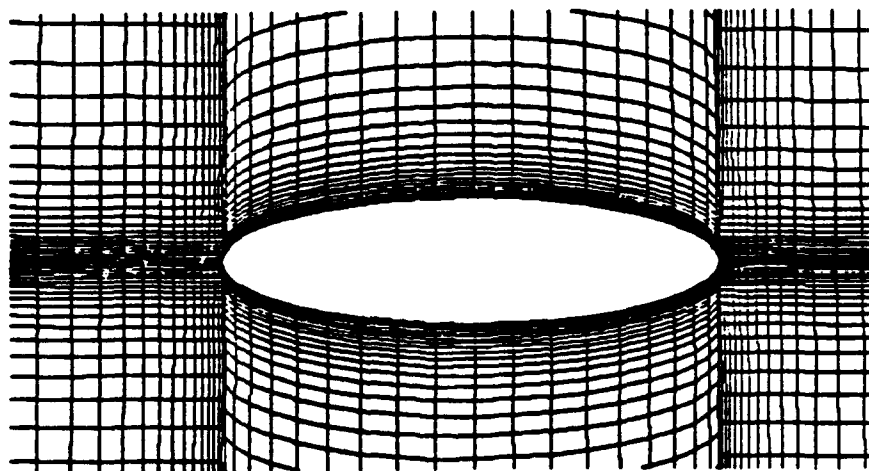
Figure 4. Dynamic Stall Hysteresis Loops for a NACA 0012 Airfoil



(a)



(b)

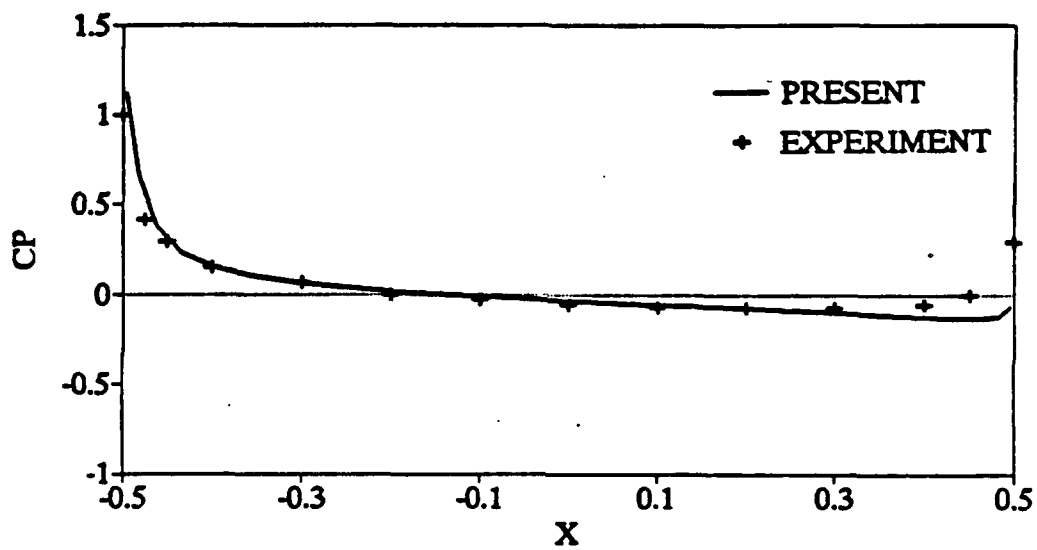


(c)

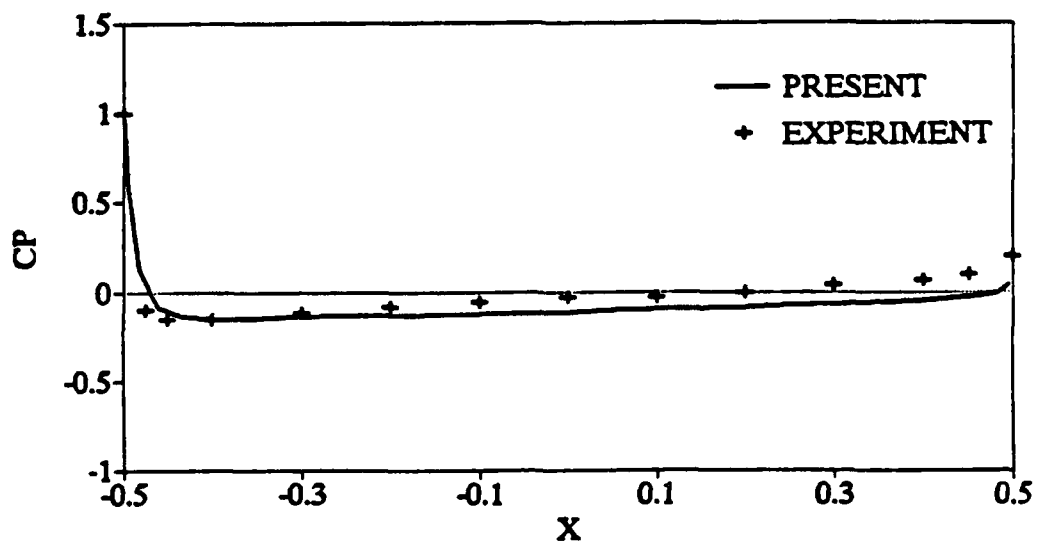
Figure 5. Body-Fitted Grid Around an Ellipsoid of Revolution



Figure 6. Streamlines over the Ellipsoid of Revolution



(a) In The Windard Plane



(b) In The Leeward Plane

Figure 7. Surface Pressure Distributions Compared With Experimental Data

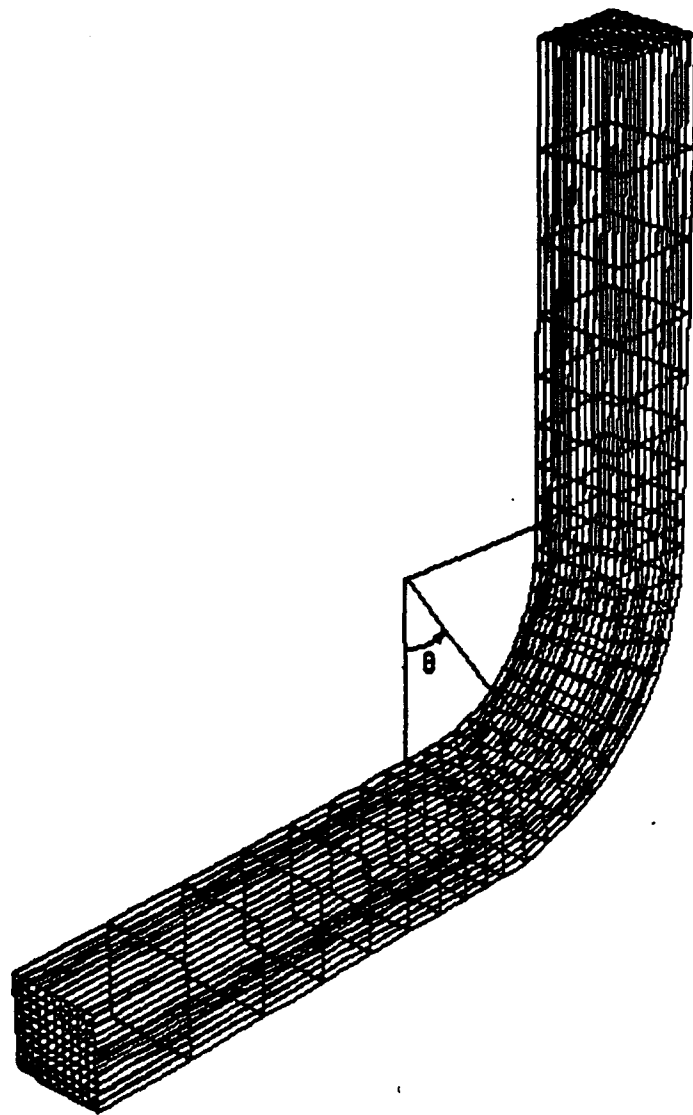


Figure 8. Body-fitted grid within a square duct
with a 90° bend

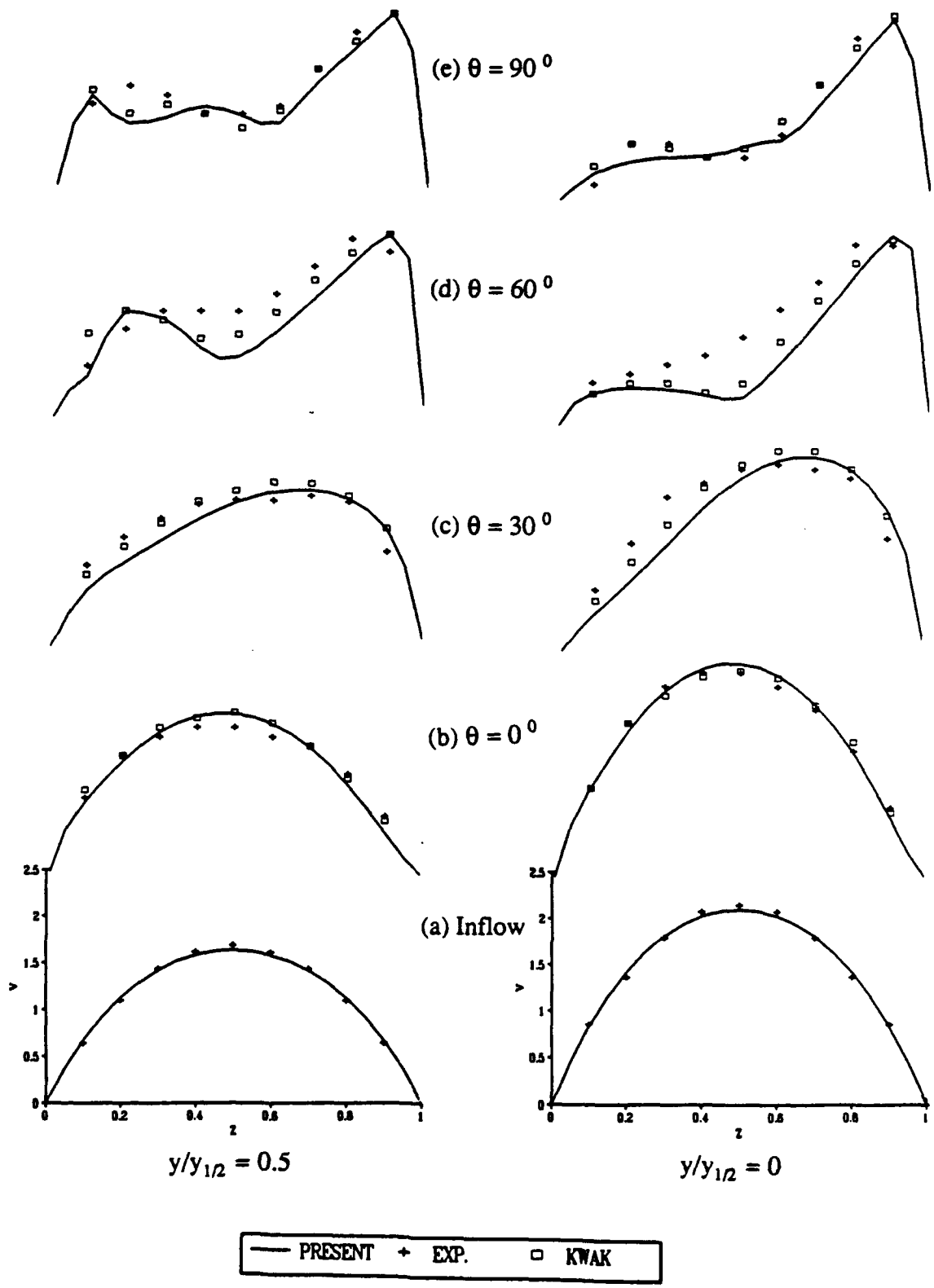
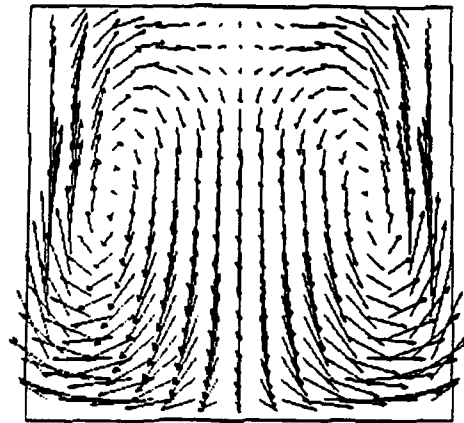
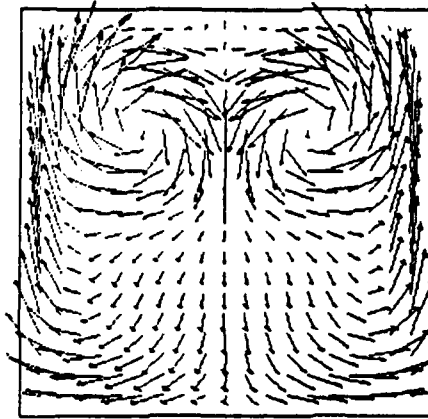


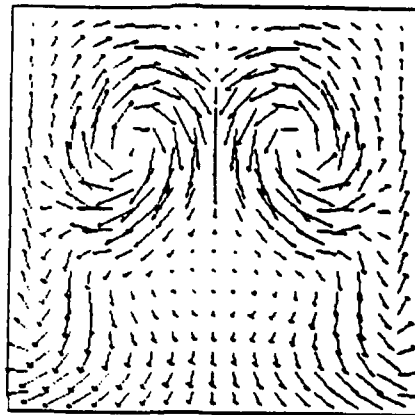
Figure 9. Streamwise Velocity Profiles



(a) $\theta = 30^\circ$

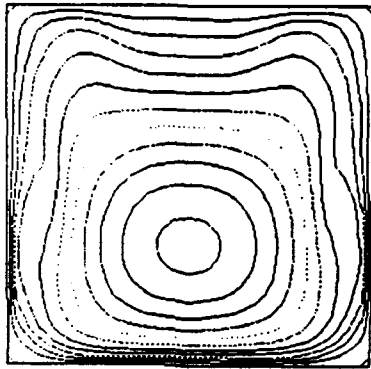


(b) $\theta = 60^\circ$

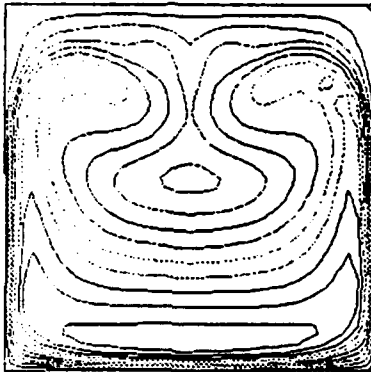


(c) $\theta = 90^\circ$

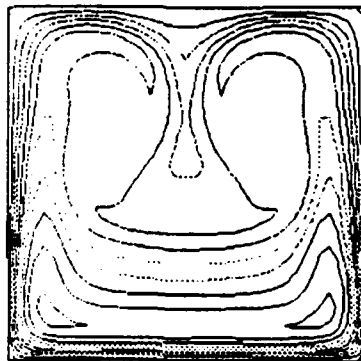
Figure 10. Cross-sectional velocity profiles at three streamwise stations in the curved section



(a) $\theta = 30^\circ$

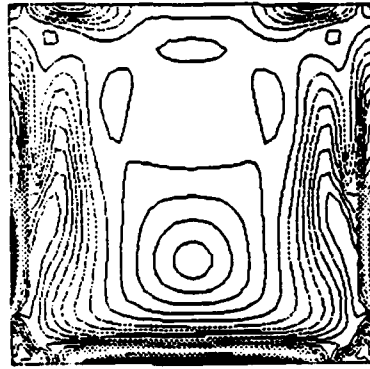


(b) $\theta = 60^\circ$

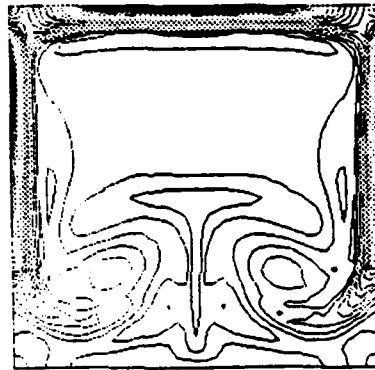


(c) $\theta = 90^\circ$

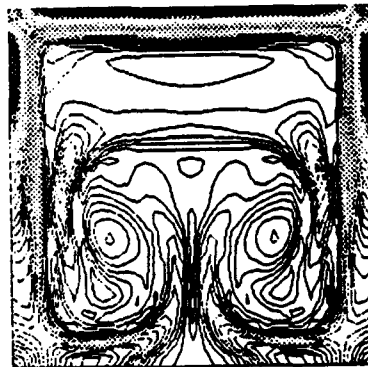
Figure 11. Velocity magnitude contours at three streamwise stations in the curved section



(a) $\theta = 30^\circ$



(b) $\theta = 60^\circ$



(c) $\theta = 90^\circ$

Figure 12. Vorticity magnitude contours at three streamwise stations in the curved section

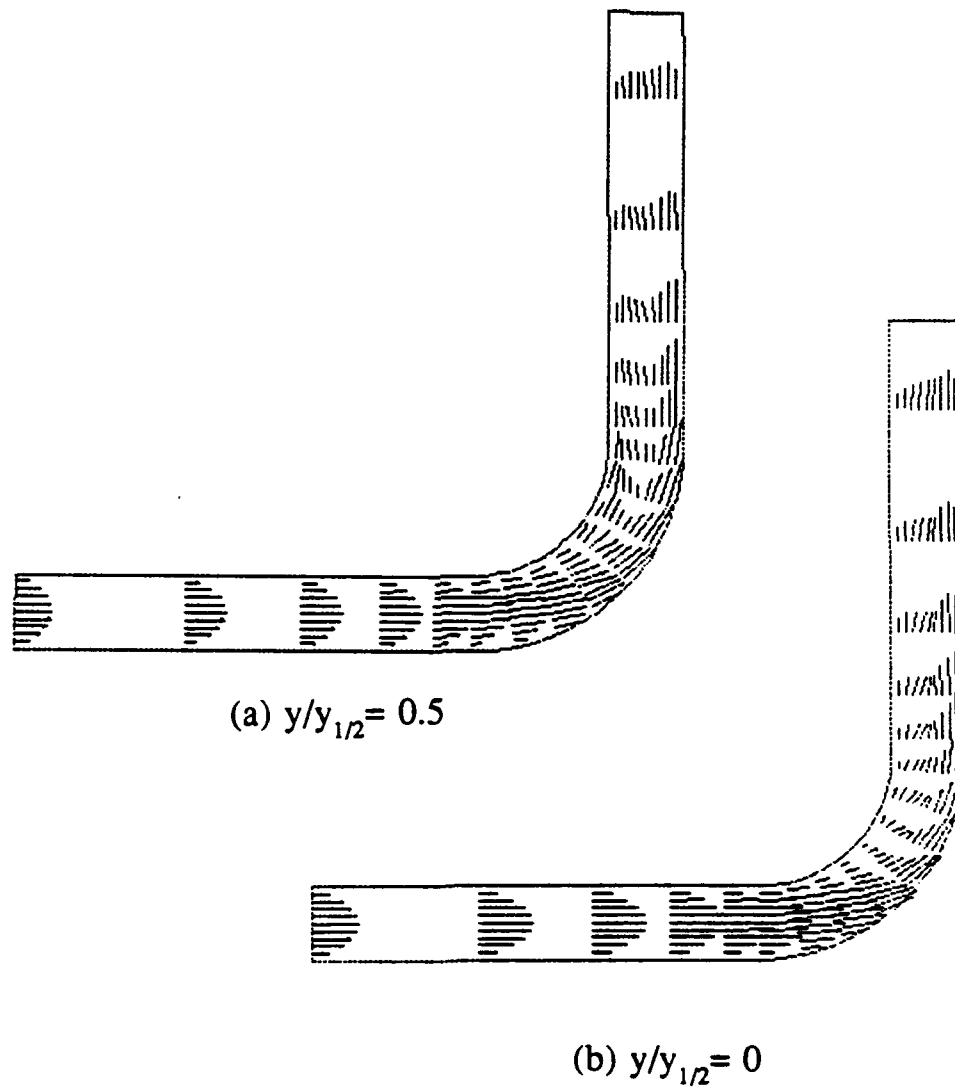


Figure 13. Streamwise velocity profiles at $y/y_{1/2} = 0.5$
and $y/y_{1/2} = 0$



(a) $z = 0.25$



(b) $z = 0.5$

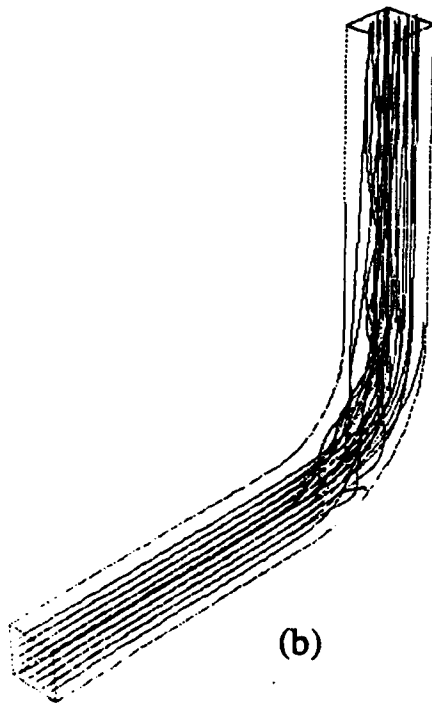


(c) $z = 0.75$

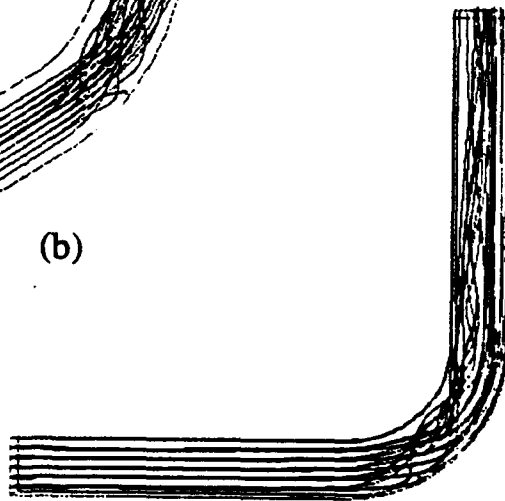
Figure 14. Streamwise velocity profiles at $z = 0.25$, $z = 0.5$,
and $z = 0.75$



(a)



(b)



(c)

Figure 15. Streamlines viewing from the three different view-points

(a) Front view

(b) Oblique view

(c) Side view

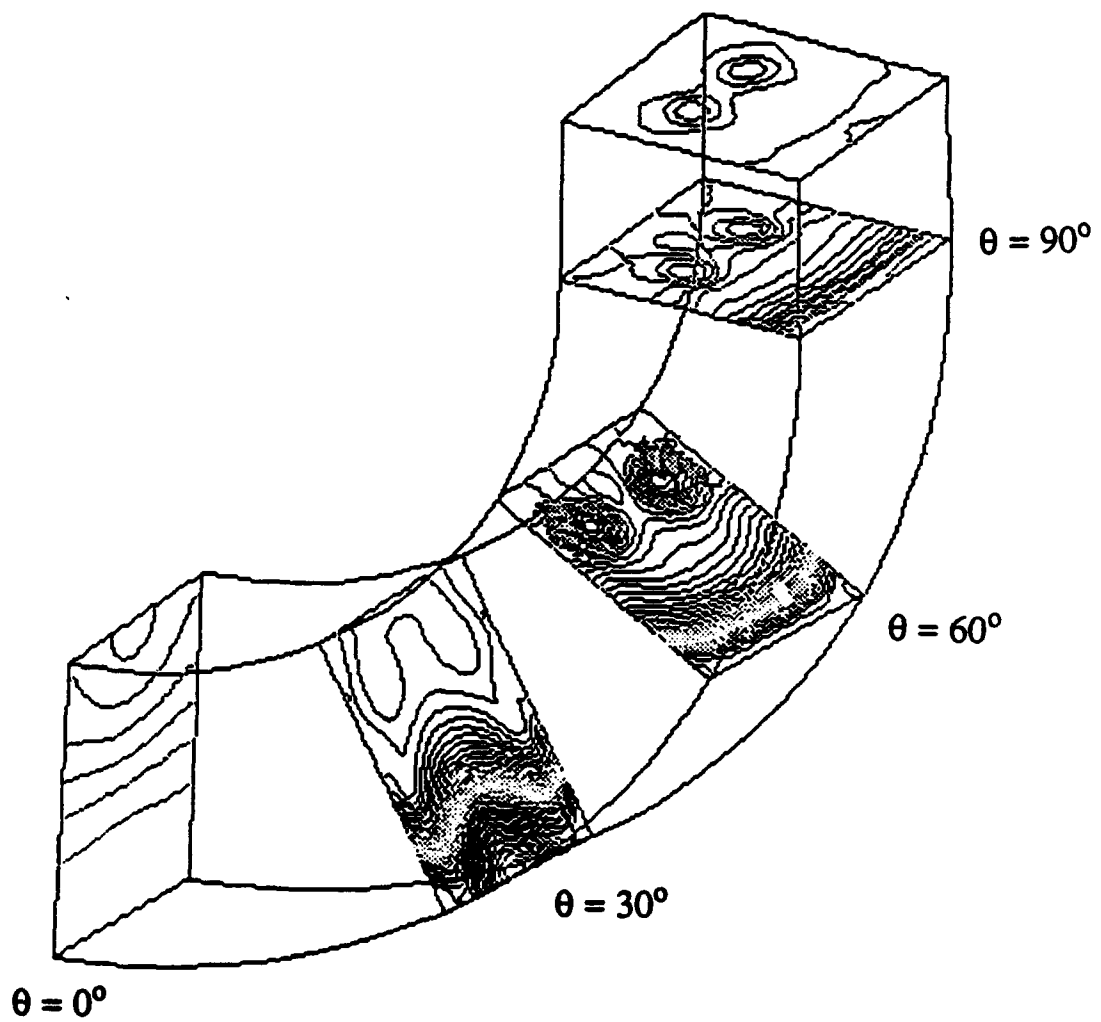


Figure 16. Pressure contours in the curved section

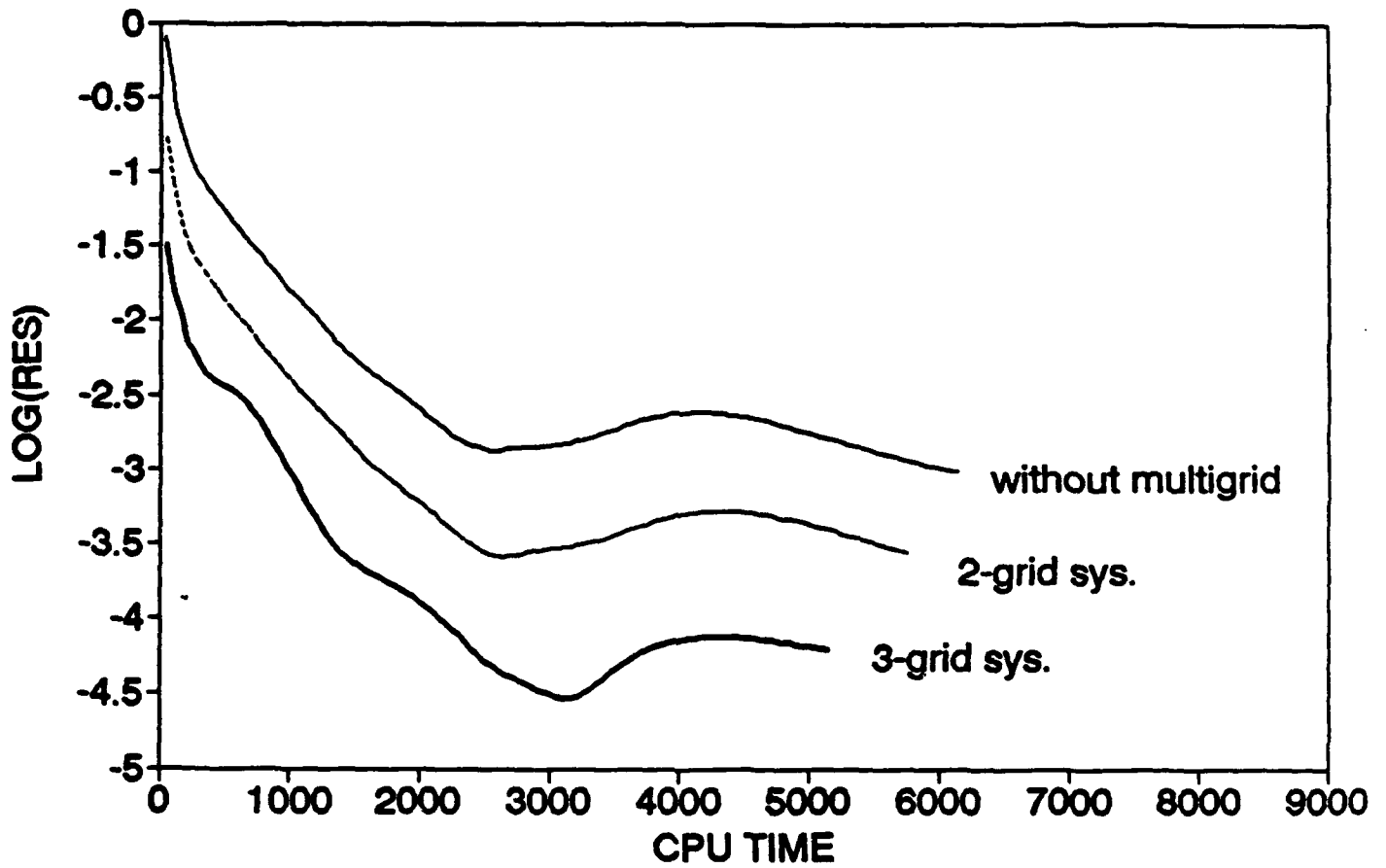


Figure 17. Comparison of convergence history of NACA 0012 airfoil for steady state (at zero angle of attack)

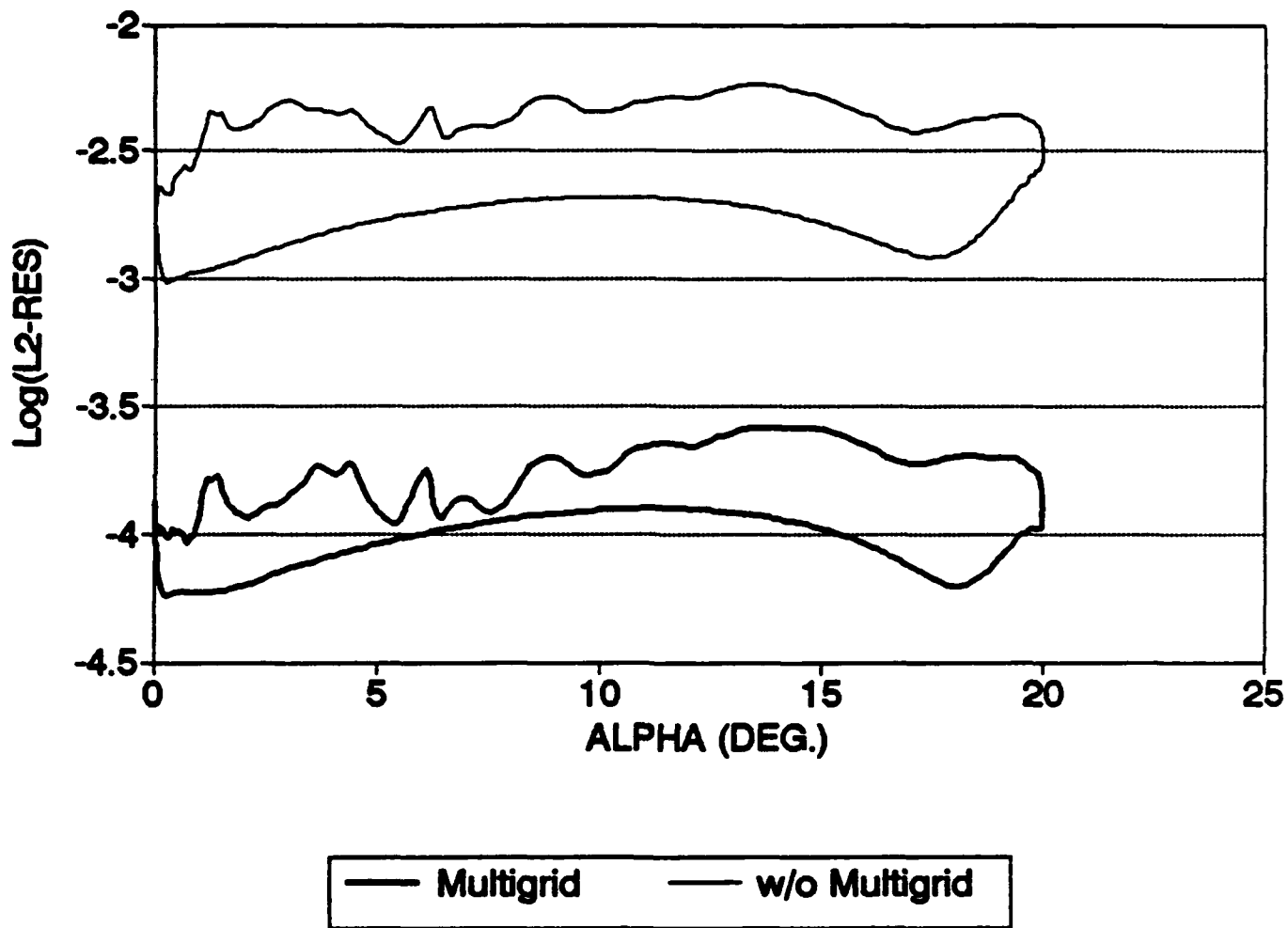


Figure 18. Comparison of global residual history of a sinusoidally oscillating airfoil

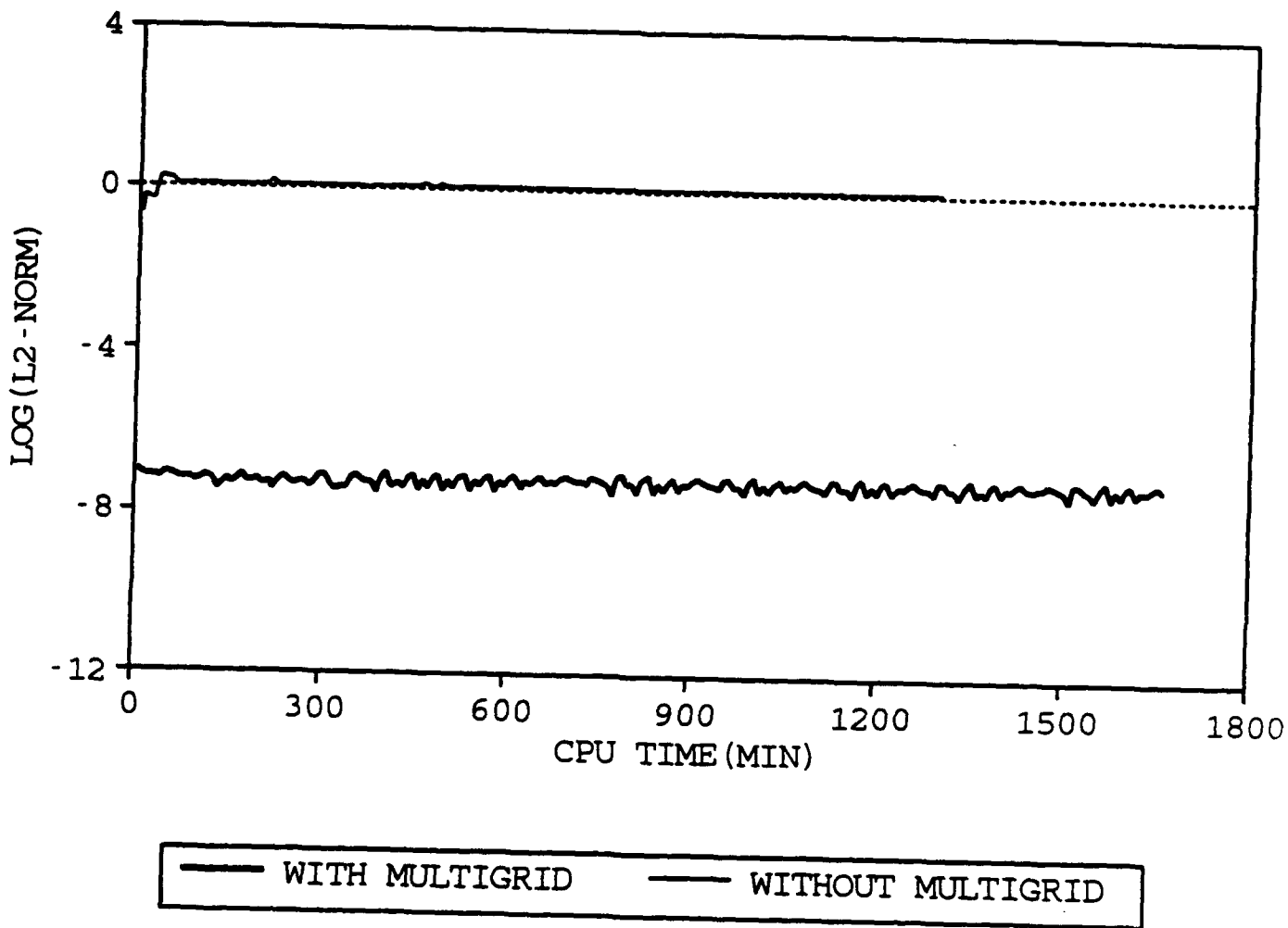
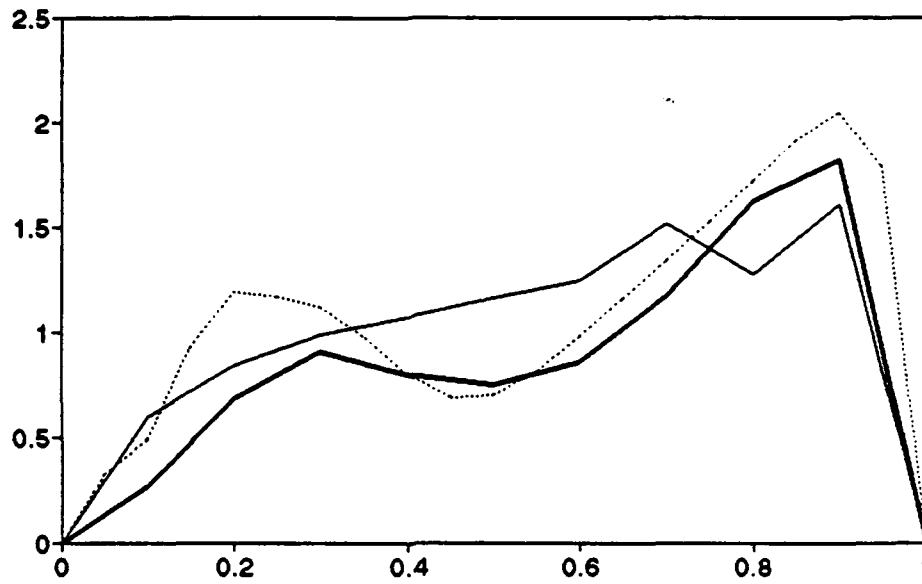
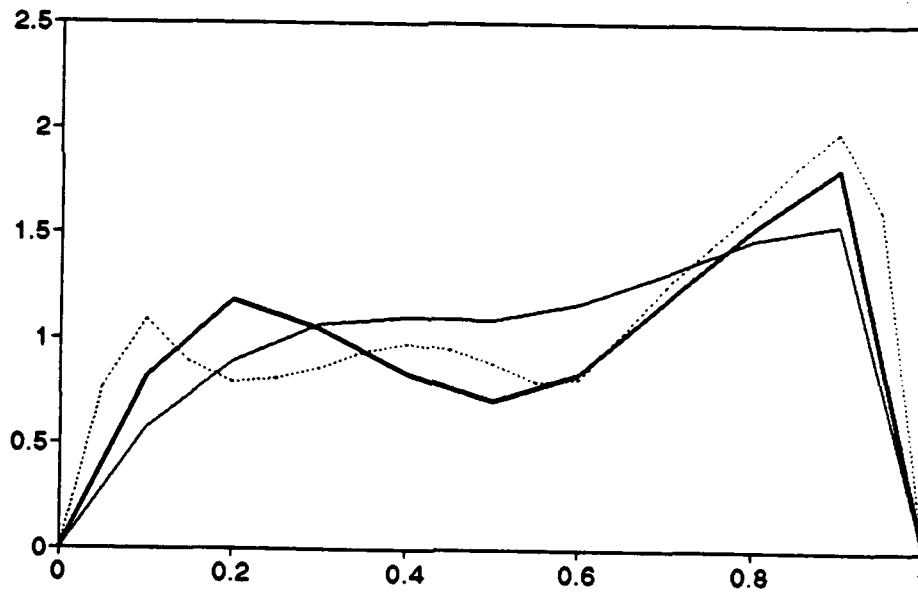


Figure 19. Comparison of convergence history of 3-D steady flow through a 90° bended square duct (Grid : $65 \times 21 \times 21$)



(a) $\theta = 60^\circ$, $y/y_{1/2} = 0.5$



(b) $\theta = 90^\circ$, $y/y_{1/2} = 0.5$

— Single Grid	— Multigrid Fine Single Grid
---------------	-------------	------------------------

Figure 20. Comparisons of streamwise velocity profile with and without multigrid technique

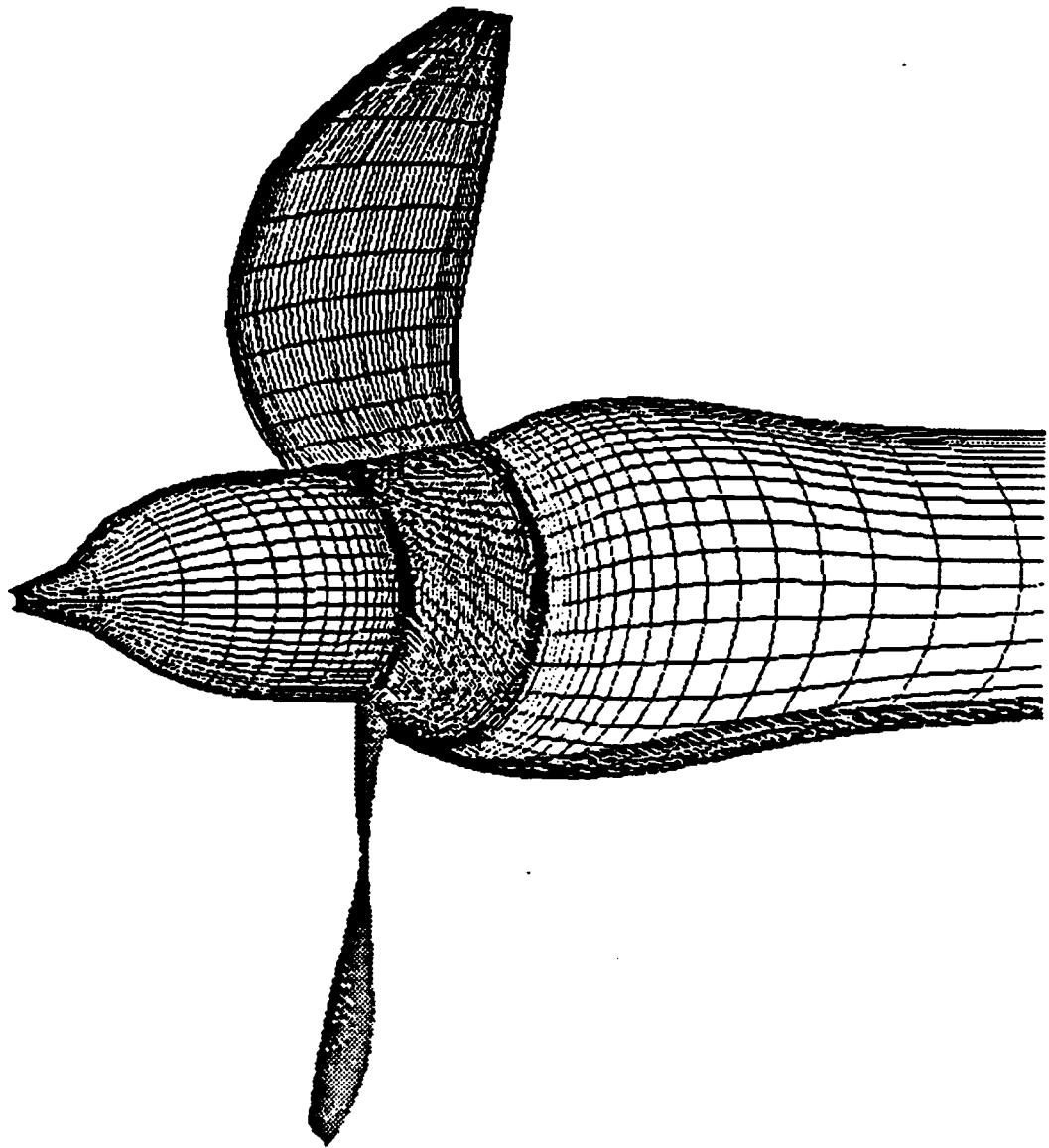


Figure 21. Configuration of marine propeller
(2-bladed SR7L)

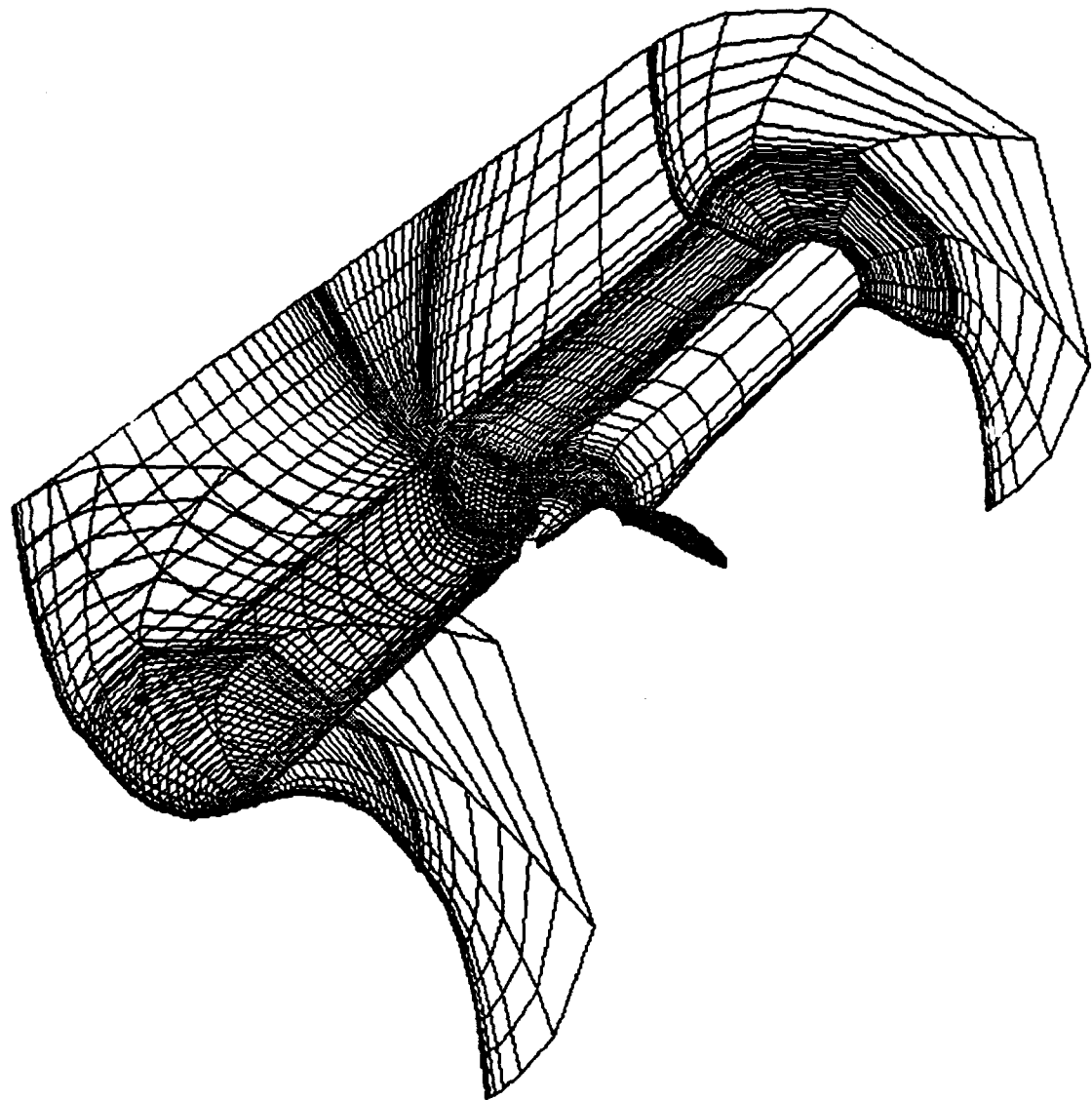


Figure 22. Body-fitted H-O grid around a SR7L propeller

CP DISTRIBUTION AT $r/R=0.284$

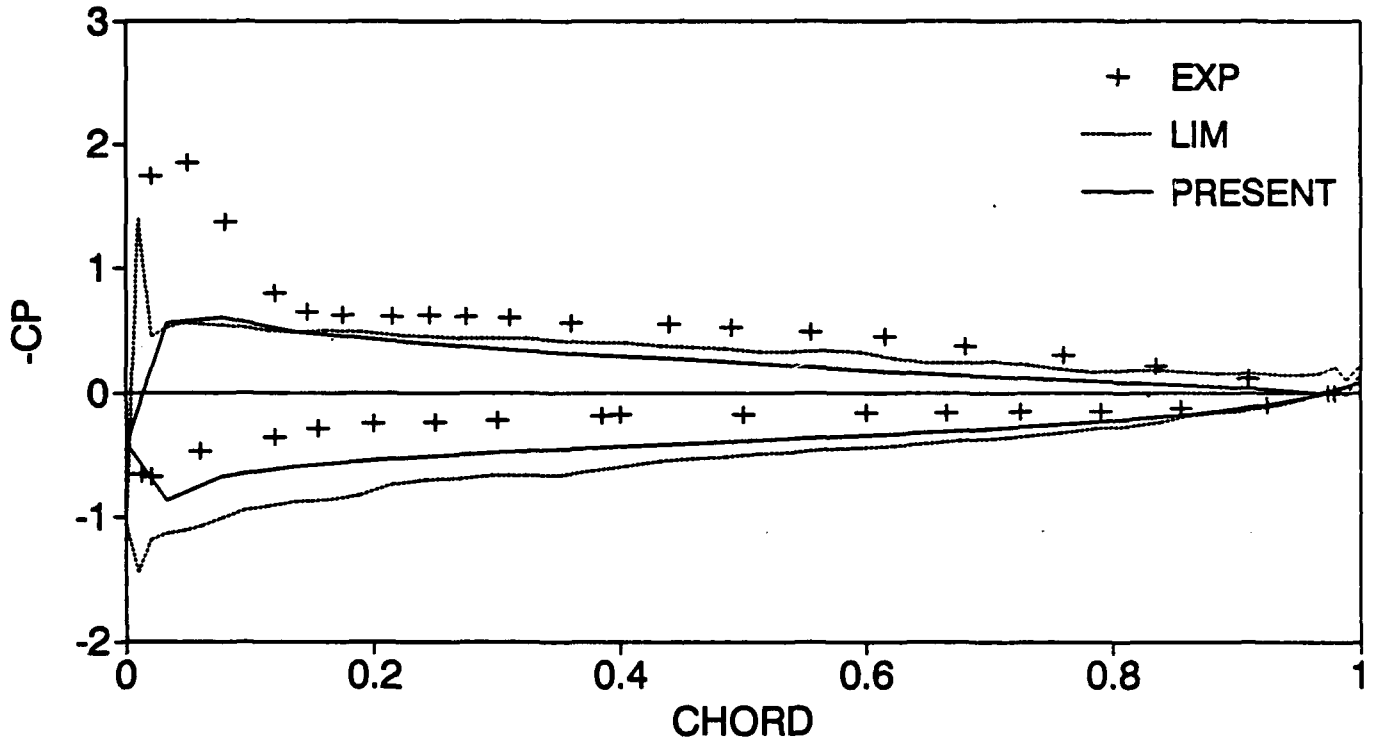


Figure 23. Chordwise pressure distribution at selected spanwise location (Advance ratio = 0.881, $\beta = 31.0$, $Re=50,000$)

CP DISTRIBUTION AT $r/R=0.57$

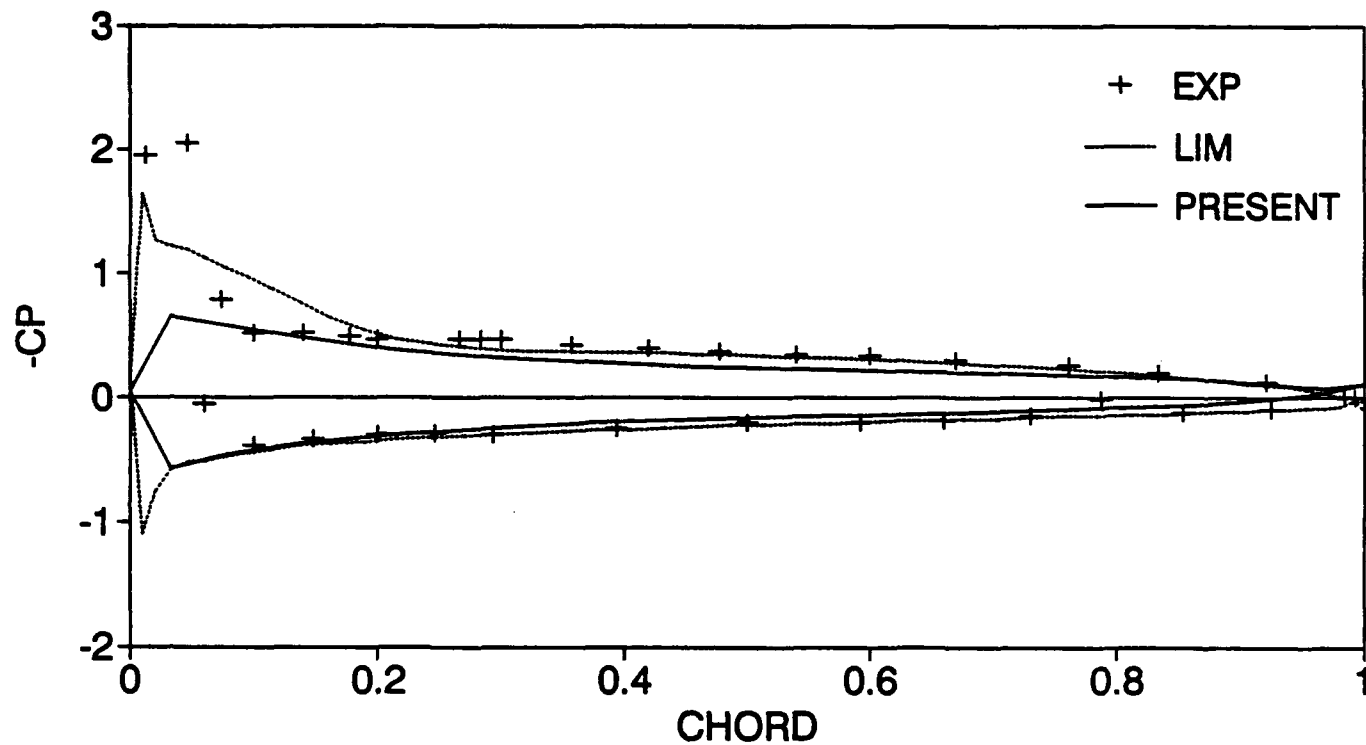


Figure 23. continued

CP DISTRIBUTION AT $r/R=0.80$

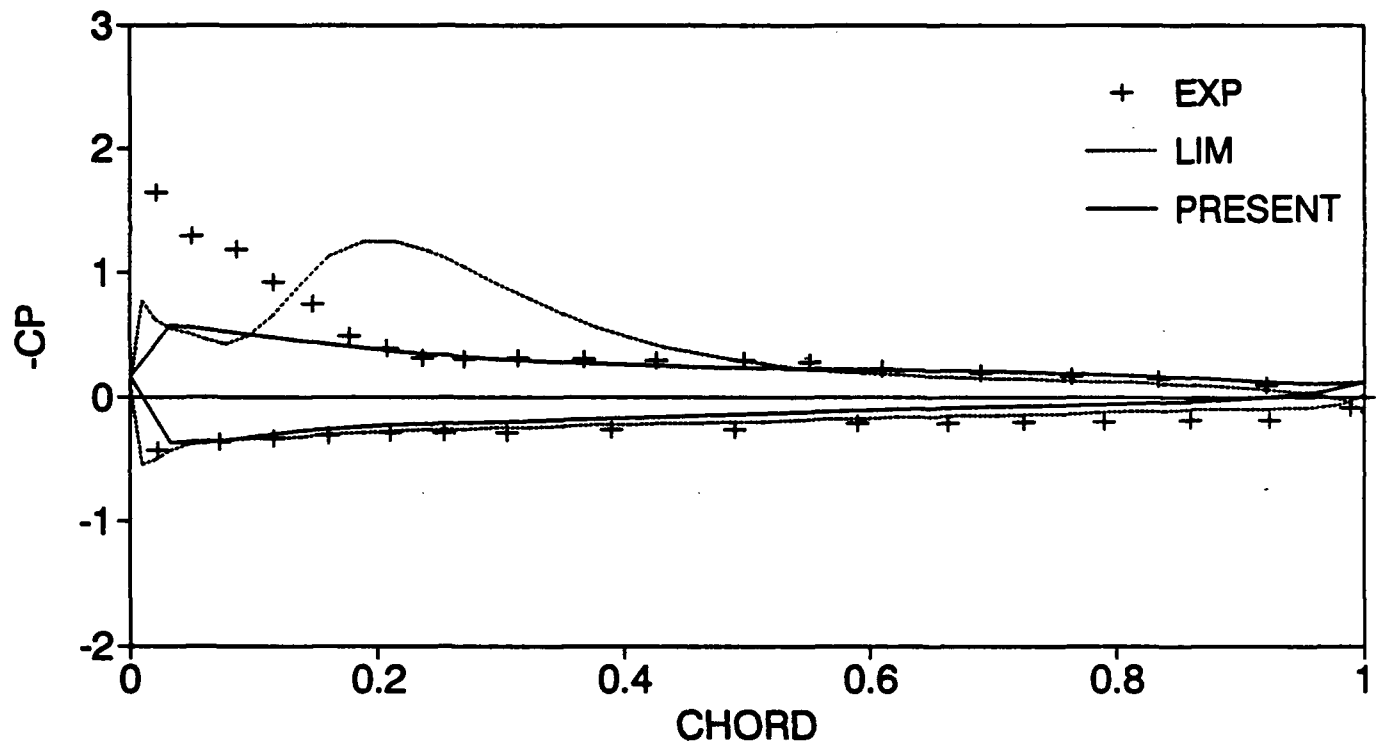


Figure 23. continued

CP DISTRIBUTION AT $r/R=0.93$

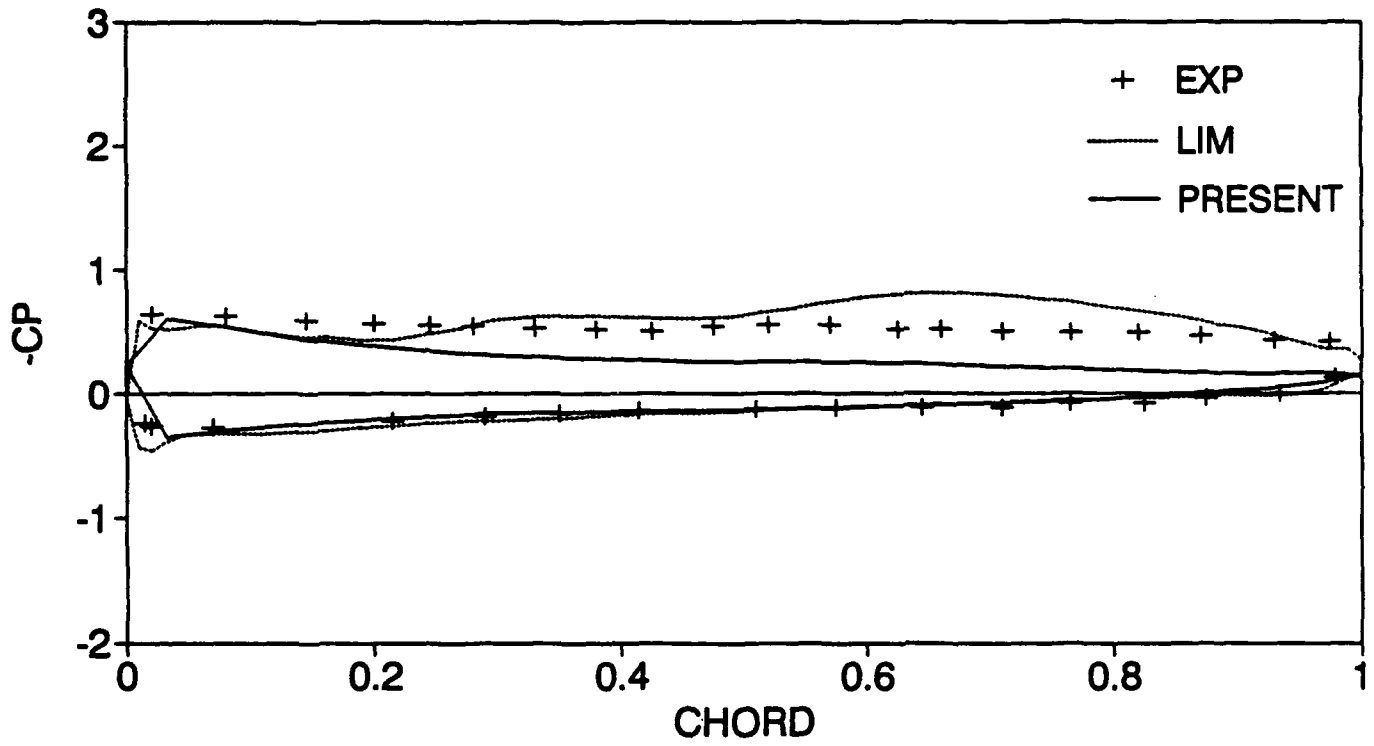


Figure 23. continued

CP DISTRIBUTION AT $r/R=0.975$

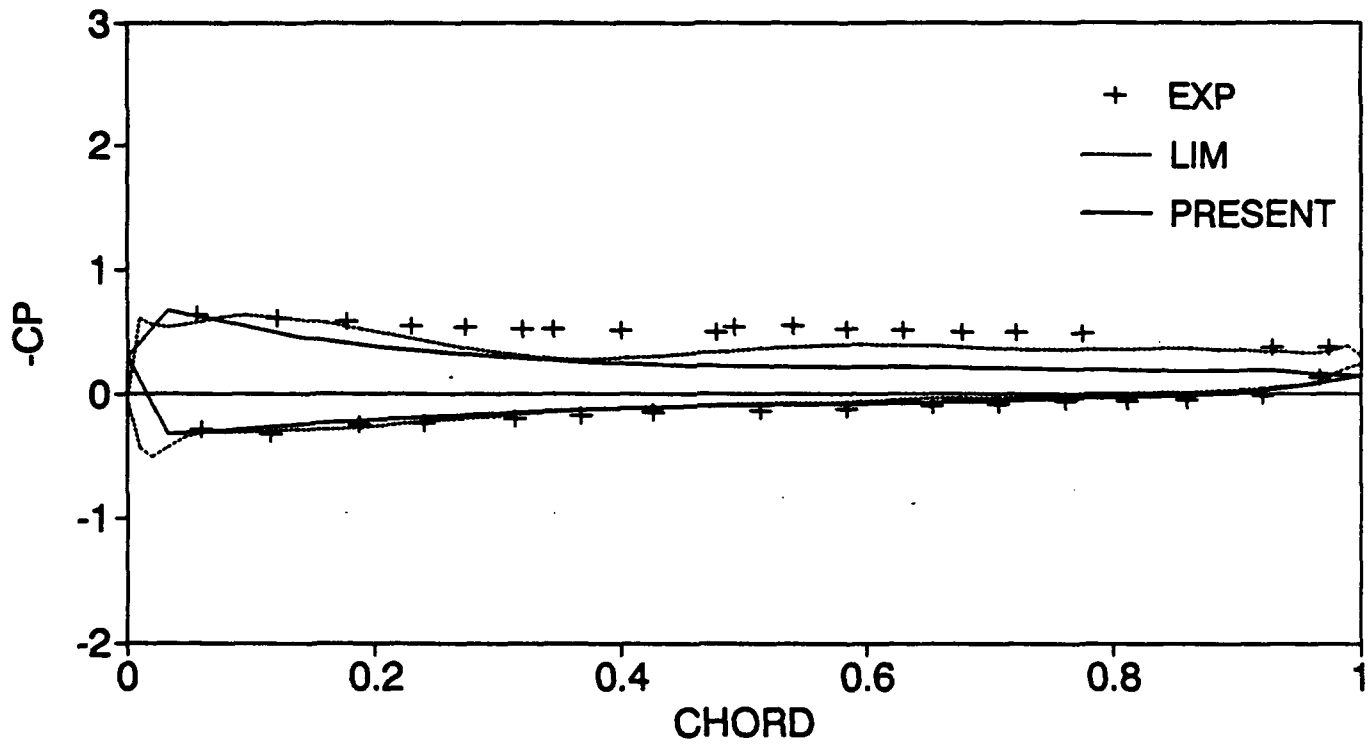


Figure 23. continued

REFERENCES

1. Gresho, P. M. and Sani, R. L., "On Pressure Boundary Conditions for the Incompressible Navier-Stokes Equations," *International Journal for Numerical Methods in Fluids*, Vol. 7, 1987, pp.1111-1145.
2. Anderson, D. A., Tannehill, J. C. and Pletcher, R. H., Computational Fluid Mechanics and Heat Transfer, Hemisphere Publishing, N.Y., 1984.
3. Mehta, U. B., "Dynamic Stall of an Oscillating Airfoil," AGARD CP-227, 1977.
4. Wu, J. C., "Numerical Boundary Conditions for Viscous Flow Problems," *AIAA Journal*, Vol. 14, No. 8, 1976, pp.1042-1049.
5. Thames, F. C., "Numerical Solution of Incompressible Navier-Stokes Equations About Arbitrary Two-Dimensional Bodies," Ph. D. Thesis, Mississippi State University, Mississippi, August, 1977.
6. Harlow, F. H. and Welch, J. E., "Numerical Calculation of Time-Dependent Viscous Incompressible Flow with Free Surfaces," *Physics of Fluids*, Vol. 8, No. 12, 1965, pp.2182-2185.
7. Osswald, G. A., Ghia, K.N. and Ghia, U., "An Implicit Time Marching Method for Studying Unsteady Flow with Massive Separation," *AIAA CP-854*, 1985, pp.686-696.
8. Goda, K., "Multistep Implicit Technique with Implicit Difference Schemes for Calculating Two- or Three-Dimensional Cavity Flows," *Journal of Computational Physics*, Vol. 30, 1979.
9. Abdallah, S., "Numerical Solutions for the Incompressible Navier-Stokes Equations in Primitive Variable Using a Non-Staggered Grid, II," *Journal of Computational Physics*, Vol. 70, 1987, pp.193-202.
10. Mansour, M. L. and Hamed, A., "Implicit Solution of the Incompressible Navier-Stokes Equations on a Non-Staggered Grids," *Journal of Computational Physics*, Vol. 86, 1990, pp.147-167.
11. Viacelli, J. A., "A Method for Including Arbitrary External Boundaries in the MAC Incompressible Fluid Computing Technique," *Journal of Computational Physics*, Vol. 4, 1969, pp.543-551.

12. Hirt, C. W. and Cook, J. L., "Calculating Three-Dimensional Flows Around Structures and Over Rough Terrain," *Journal of Computational Physics*, Vol. 10, 1972, pp.324-340.
13. Chorin, A. J., "Numerical Solution of Navier-Stokes Equations," *Mathematics of Computation*, Vol. 22, 1968, pp.745-762.
14. Steger, J. L. and Kutler, P., "Implicit Finite-Difference Procedures for the Computation of Vortex Wakes," *AIAA Journal*, Vol. 15, 1977, pp.581-590.
15. Kwak, D., Chang, J. L. C., Shanks, S. P. and Chakravarthy, S. R., "A Three-Dimensional Incompressible Navier-Stokes Flow Solver Using Primitive Variables," *AIAA Journal*, Vol. 24, 1986, pp.390-396.
16. Chorin, A. J., "A Numerical Method for Solving Incompressible Viscous Flow Problems," *Journal of Computational Physics*, Vol. 2, 1967, pp.12-26.
17. Beam, R. M. and Warming, R. F., "An Implicit Finite-Difference Algorithm for Hyperbolic Systems in Conservative-Law Form," *Journal of Computational Physics*, Vol. 22, 1976, pp.87-110.
18. Merkle, C. L. and Athavale, M., "Time-Accurate Unsteady Incompressible Flow Algorithms Based on Artificial Compressibility," *AIAA Paper 87-1137*, June 1987.
19. Rogers, S. E. and Kwak, D., "Steady and Unsteady Solutions of the Incompressible Navier-Stokes Equations," *AIAA Journal* Vol. 29, No. 4, 1991, pp.603-610.
20. Shih, T. M., Tan, H and Hwang, B. C., "Equivalence of Artificial Compressibility Method and Penalty-Function Method," *Numerical Heat Transfer, Part B*, Vol. 15, 1989, pp.127-130.
21. Leonard, B. P., "A Stable and Accurate Convective Modelling Procedure Based on Quadratic Upstream Interpolation," *Computer Methods in Applied Mechanics and Engineering*, Vol. 19, 1979, pp.59-98.
22. Michelassi, V. and Benocci, C., "Prediction of Incompressible Flow Separation with the Approximate Factorization Technique," *International Journal for Numerical Methods in Fluids*, Vol. 7, 1987, pp.1383-1403.
23. Biringen, S. and Cook, C., "On Pressure Boundary Conditions for the Incompressible Navier-Stokes Equations Using Nonstaggered Grids," *Numerical Heat Transfer*, Vol. 3, 1988, pp.241-252.
24. Werle, H., "Hydrodynamic Flow Visualization," *Annual Review of Fluid Mechanics*, Vol. 5, 1973, pp.361-382.
25. Patel, V. C. and Baek, J. H., "Boundary Layers in Planes of Symmetry, Part II : Calculations for Laminar and Turbulent Flows," *AIAA Journal*, Vol. 25, No. 6, 1987, pp.812-818.

26. Meier, H. U. and Kreplin, H. D., "Experimental Investigation of Boundary Layer Transition and Separation on a Body of Revolution," *Zeitschrift für Flugwissenschaften und Weltraumforschung*, Vol. 4, No. 2, 1980, pp.65-71.
27. Humphrey, J. A. C., Taylor, A. M. K. and Whitelaw, J.H., "Laminar Flow in a Square Duct of a Strong Curvature," *Journal of Fluid Mechanics*, Vol.83, 1977, pp.590-527.
28. White, F. M. Viscous Fluid Flow, McGraw-Hill, 1974, pp.120.
29. Bober, L. J., Barton, J. M., and Yamamoto, O., "Inviscid Analysis of Advanced Turboprop Propeller Flow Field," AIAA Paper 85-1263, 1985
30. Bober, L. J., Yamamoto, O., and Barton, J. M., "Improved Euler Analysis of Advanced Turboprop Propeller Flow," AIAA Paper 86-1521, 1986
31. Chaussee, D. S., "Computation of Three Dimensional Flow Through Propfans," Nielsen Engineering and Research Inc., NEAR TR-199, 1979
32. Chaussee, D. S., Bober, L. J., and Kutler., "Prediction of High Speed Propeller Flow Fields Using a Three Dimensional Euler Analysis," AIAA Paper 83-0188, 1983
33. Egolf, T. A., Anderson, O. L., Edwards, D. E., and Landgrebe, A. J., "An Analysis for High Speed Propeller-Nacelle Aerodynamic Performance; Vol.1, Theory and Initial Application and Vol.2, User's Manual for the Computer Program," United Technologies Research Center, R79-912949-19, 1979
34. Goldstein, S., "On the Vortex Theory of Screw Propellers," *Royal Society Proceeding*, Vol.123, no.792, pp.440-465, 1929
35. Hall, E. J., Delaney, R. A., and Bettner, J. L., "Investigation of Advanced Counter Rotating Blade Configuration Concepts for High Speed Turboprop System ; Task 2, Unsteady Ducted Propfan Analysis," Final Report, NASA CR-187106, 1991
36. Harlow, F. H. and Welch, J. E., "Numerical Calculation of Time-Dependent Viscous Incompressible Flow with Free Surfaces," *Physics of Fluids*, Vol. 8, No. 12, 1965, pp.2182-2185.
37. Jou, W. H., "Finite Volume Calculation of the Three Dimensional Flow Around a Propeller," AIAA Paper 82-0957, 1982
38. Kerwin, J. E., "Marine Propeller," *Annual Review of Fluid Mechanics*, Vol.18, pp.367-403, 1986
39. Kim, H. T., "Computation of Viscous Flow Around a Propeller-Shaft Configuration with Infinite-Pitch Rectangular Blades," Ph.D. Thesis, The University of Iowa, Iowa City, IA, 1989
40. Lim, T. B. and Sankar, L. N., "Viscous Flow Computations of Flow Field around an Advanced Propeller," AIAA Paper 93-0873, 1993

41. Matsuo, Y., Arakawa, C., Satio, S., and Kobayashi H., "Navier-Stokes Computations for Flow Field of an Advanced Turboprop," AIAA Paper 88-3094, 1988
42. Sankar, L.N. and Park, W.G., "An Iterative Time Marching Procedure for Unsteady Viscous Flows," ASME-BED Vol.20, pp.281-284, 1991
43. Srivastava, R. and Sankar, L. N., "Application of an Efficient Hybrid Scheme for Aeroelastic Analysis of Advanced Propeller," AIAA Paper 90-0028, 1990
44. Sullivan, J. P., "The Effect of Blade Sweep on Propeller Performance," AIAA Paper 77-176, 1977
45. Whitfield, D. L., Swafford, T. W., and Arnold, A. F. S., and Belk, D. M., "Three Dimensional Euler Solution for Single Rotating and Counter Rotating Propfan," AIAA Paper 87-1197, 1987